2017

Cathepsin K Targeting Matrix Regenerative Nanoparticles for Small Abdominal Aortic Aneurysm Repair

Jonathan M. Fox
Cleveland State University

CATHEPSIN K TARGETING MATRIX REGENERATIVE NANOPARTICLES FOR SMALL ABDOMINAL AORTIC ANEURYSM REPAIR

JONATHAN M. FOX

Bachelors of Arts Biochemistry and Molecular Biology

The College of Wooster

May 2012

Submitted in partial fulfillment of requirements for the degree

MASTER OF SCIENCE IN BIOMEDICAL ENGINEERING

at

CLEVELAND STATE UNIVERSITY

May 2017

We hereby approve this thesis for

Jonathan M. Fox

Candidate for the Master of Science in Biomedical Engineering degree for the

Department of Chemical and Biomedical Engineering

and the CLEVELAND STATE UNIVERSITY

College of Graduate Studies

Thesis Chairperson, Dr. Anand Ramamurthi

Department of Biomedical Engineering, Cleveland Clinic

_____

Date

Thesis Committee Member, Dr. Nolan Holland

Chemical and Biomedical Engineering Department, Cleveland State University

_____

Date

Thesis Committee Member, Dr. Chandrasekhar Kothapalli

Chemical and Biomedical Engineering Department, Cleveland State University

_____

Date

Date of Defense: May 1, 2017

ACKNOWLEDGMENTS

I would like to thank Dr. Anand Ramamurthi for this opportunity in the Biomedical Engineering Department at The Cleveland Clinic Foundation. Dr. Ramamurthi has been incredibly supportive in my research and an invaluable resource who has pushed me to expand my scientific skills. His advice and guidance has helped me develop as a scientist and set me up for success in the future.

I would like to thank my current and previous peers in the lab for all their help and advice with experiments: Drew Camardo, Shataakshi Dahal, Daniel Ortiz, Dhruv Seshadri, and Ganesh Swaminathan. I would also like to thank the Imaging Core staff at The Cleveland Clinic, specifically, Dr. Judy Drazba and Eric Diskin, for all their technical assistance and help with my various projects. I want to thank the Biomedical Engineering Department at The Cleveland Clinic and the Cleveland State University Biomedical Engineering Department for their support during my time in the program.

I would also like to thank my family and friends for all their support during this entire process. My family has always supported my education and have played a major role in my success.

CATHEPSIN K TARGETING MATRIX REGENERATIVE NANOPARTICLES FOR SMALL ABDOMINAL AORTIC ANEURYSM REPAIR

JONATHAN M. FOX

ABSTRACT

Abdominal aortic aneurysms (AAAs) are characterized by the loss of elasticity in the aorta wall leading to a chronic increase in diameter and resulting in rupture. This is due to the lack of regeneration of elastic fibers and chronic proteolytic breakdown of elastic fibers within the aorta mediated by matrix metalloproteinases (MMPs), specifically MMP-2 and -9. Previous studies in our lab have shown cationic amphiphile-surface functionalized poly(lactic-*co*-glycolic acid) (PLGA) nanoparticles (NPs) loaded with doxycycline (DOX) to inhibit MMP activity and stimulate elastic matrix synthesis, effects we attributed to both low doses (< 10 mg/ml) of DOX released and independent effects of cationic amphiphile pendant groups on the NP surface. This promises application of these NPs to arrest or regress AAA growth since high oral DOX dosing inhibits new elastic matrix formation in the AAA wall and has undesirable side effects. In this study, we investigated feasibility of antibody-based active targeting of intravenously infused NPs to the AAA wall. Cathepsin K, a cysteine protease, is a biomarker for AAA and overexpressed in abdominal aortic aneurysm tissue making it an ideal target moiety. We have shown using a covalent conjugation method of modifying the surface of the NPs with a cathepsin K antibody resulted in a more robust antibody attachment which did not affect the DOX release profile. Cathepsin K expression was confirmed to be localized on the cell surface and utilizing cathepsin K Ab-conjugated NPs, we demonstrated an increased NP

localization to the cathepsin K overexpressing cells *in vitro* and *ex vivo*. Importantly, the DOX-loaded NPs demonstrated pro-elastogenic and anti-proteolytic effects in aneurysmal smooth muscle cells supporting their use as regenerative therapies to arrest and regress AAA growth. Preliminary data has been collected indicating cathepsin K Ab-conjugated NP targeting to AAAs in elastase-injured rat models. The study outcomes support the feasibility of using cathepsin K Ab-conjugated NPs as a targeted therapy for elastic matrix regeneration in AAA tissue and will serve as a basis for already initiated follow up studies to assess NP biodistribution, in situ retention in the AAA wall, and safety as a function of time.

TABLE OF CONTENTS

LIST OF TABLES

LIST OF FIGURES

CHAPTER I

INTRODUCTION

1.1. Cardiovascular disease and abdominal aortic aneurysms

Cardiovascular disease (CVD) broadly describes a variety of disease states including coronary artery disease, myocardial infarction, heart failure, and aneurysms[1]. Currently, CVD is the leading cause of death in the United States, with approximately one-third of the population living with at least one type of CVD, and one of the most prominent causes of death worldwide[1–3]. CVD is becoming more prevalent in the US, and currently accounts for ~17% of the healthcare expenditures with the medical costs increasing by ~6% annually[2]. In 2010, it was estimated $444 billion was spent on treatment and medications for CVD and associated lost productivity, while hospitalization costs reached an additional $33 billion[3]. With increased prevalence and cost associated with CVD, treatment options and preventative measures are becoming areas of much interest[4].

Abdominal aortic aneurysms (AAAs) are a prominent manifestation of CVD. They are abnormal and rupture-prone expansions of the wall of the abdominal aorta segment (**Figure 1.1**). AAAs occur in approximately 6-7.6% of men and 0.7-1.3% of women (increases to 6% when multiple risk factors present) in the US, and account for more than

13,000 deaths per year domestically[5–7]. While certain sub-populations (elderly males, Caucasians, and smokers) have been identified to be more susceptible to developing AAAs, screening these individuals at an early stage in AAA development is vital. Currently, the United States Preventive Task Force recommends men between the ages of 65 to 75 undergo a one-time ultrasound screening to detect and thus initiate early management of AAAs[8]. If unchecked, the mortality rate after AAA rupture is ~80% and 50% for those who receive emergency reparative surgery[5,9]. This data emphasizes the importance of early diagnosis, identification, and treatment of AAAs, especially since this can improve survival and can be a cost-effective preventative measure.

Figure 1.1. CT scan of an AAA in a 76-year old asymptomatic male[5]. Adapted by permission from Macmillan Publishers Ltd: [NATURE REVIEWS CARDIOLOGY], Pathophysiology and epidemiology of abdominal aortic aneurysms. Copyright 1 Feb 2011

Risk factors that have been associated with the formation and growth of AAAs include age, sex, family history, smoking, lipid levels, hypertension and obesity[5,10]. The risk of AAA formation increases with age with individuals in the >50 year old segment being especially prone to developing AAAs. AAA rupture is rare below 65 years of age but the risk increases by 40% for every 5 years after the age of 65[5]. Men are at a 6-fold higher risk for AAA formation than are women but the AAA development in women is highly correlated to family history suggesting that genetics also play a vital role in disease etiology[6]. Patients with a positive family history were found to exhibit twice the risk of AAA formation than someone without a family history[5].

The formation and growth of an AAA is a very slow process, extending over 5-7 years and results from the loss of the structural extracellular matrix (ECM; stretch and recoil generating elastic fibers and collagen fibers that impart stiffness and load bearing strength)[11,12] in the wall of the aorta due to chronically overexpressed matrix metalloproteinase (MMP) enzymes and cysteine proteases[13–16]. AAA growth is generally seen as irreversible or even difficult to arrest due to poor auto-regeneration and repair of elastic matrix structures in adult tissues, and lack of technologies to overcome these issues[17].

1.2. Current methods to diagnose and treat AAAs

Since AAAs are typically asymptomatic until they attain a critical size (> 5.5cm in diameter versus a normal aorta with a diameter of 2-2.5 cm), their detection tends to mostly coincide with elective imaging-based screening of high risk patients with known risk factors for AAA formation (e.g. elderly Caucasian males and smokers)[9]. The World Health

Organization (WHO) has developed protocols and guidelines to determine the effectiveness and usefulness of screening tests for specific diseases. Based on the criteria set by the WHO, AAAs can be considered a screenable disease which will help increase survival rates[9].

Among other techniques, ultrasound has been utilized to successfully detect aneurysmal expansions. Ultrasound technology can clarify the diameter of the aneurysm, an important factor in determining the future treatment course[9]. The screening method has proven to be an effective tool in reducing rupture and increase survival rates with studies showing screening processes can reduce the rate of rupture by 55-70% over a five year period[9]. Current management of AAAs smaller than a critical size of 5.5 cm is limited to such passive ultrasound based growth monitoring, conducted every 6 months. If the aneurysm is close to 5 cm in diameter, or if the annual growth rate exceeds 10%, active treatment may be mandated, since significant increases in risk of AAA rupture are indicated[10]. At this time, active treatment of large, critically-sized AAAs is primarily via surgical intervention (**Figure 1.2**).

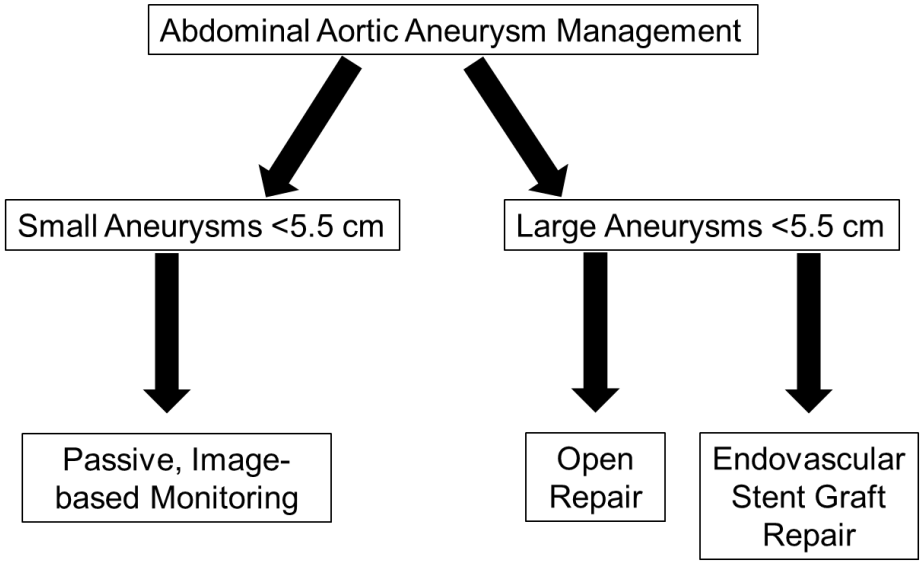

Figure 1.2. Current treatment options based on AAA size and patient history.

In the open repair procedure[18], the aneurysmal vessel segment is surgically excised and replaced with a graft. In the minimally invasive endovascular repair (EVAR) procedure, the aorta is opened lengthwise and a stent inserted within. Once the stent has been inserted, both ends of the stent are sutured to the aortic wall such that blood does not leak out. Once the stent is attached to the aorta, the aortic wall is closed around the stent and sutured back together[18,19]. Despite being applied to large rupture prone AAAs, surgery on small (<5.5 cm diameter) AAAs is elective, and performed in only ~35% of small AAAs[20]. Such elective surgical intervention has been found to provide no benefit in terms of preventing continued AAA growth to rupture or improving post-op patient survival. The procedural risk of surgery on small AAAs also greatly exceeds their rupture risk (~2% for aneurysms less than 4 cm)[20]. Since no other clinically proven drug-based treatments exist for small AAAs, management of small AAAs, as mentioned above, is currently limited to passive, imaging-based growth monitoring leading to a pre-rupture stage when surgery is

inevitable. Given the slow growth of AAAs to rupture, which occurs over a 5-7 year period, there is a long-window of opportunity to deliver therapies targeting arrest or reversal of AAA growth.

Although there are several drugs in the discovery pipeline for the treatment of AAAs, treatment of AAAs with doxycycline (DOX), a modified tetracycline with antibiotic properties has been most promising. Studies have shown DOX to attenuate MMP activity in the AAA wall to slow proteolytic disruption of the aortic wall ECM[17,21], towards slowing AAA growth. However, most of these outcomes have been observed in animal models[18,19] and clinical outcomes are inconsistent[5]. There are also other critical challenges with DOX therapy including **a)** systemic inhibition of MMPs, which play essential roles in healthy tissue remodeling and maintenance, **b)** several body-wide side effects, and **c)** inhibitory effects of DOX at these high oral doses, on the already poor deposition of new, crosslinked elastic matrix in the AAA wall[22]. Since restoring elastic matrix homeostasis is essential to arrest or reverse AAA growth, oral DOX therapy has poor prospects to achieve these outcomes. Recent findings in our laboratory have shown for the first time that DOX at low micromolar doses maintains its anti-MMP effects but additionally, also provides pro-elastogenic properties[23]. On the basis of this evidence, and considering the deficiencies of oral DOX dosing, there is a significant motivation for AAA tissue-localized, predictable and sustained low level DOX dosing. Nanoparticles (NPs) may be useful vehicles for such localized drug therapy.

1.3. Nanoparticles and their use as a targeted treatment option

The term nanoparticle can be used to describe an object in the size range of approximately 1 to 100 nm in all three dimensions while other definitions suggest the range is from 5 to 200 nm or even as large as 1 μm[24–26] (**Figure 1.3**). However, the definition of a nanoparticle is not necessarily determined by its size but rather by its physical properties. A particle could be considered a nanoparticle if its properties are different than the properties of the bulk material of the same substance[24].

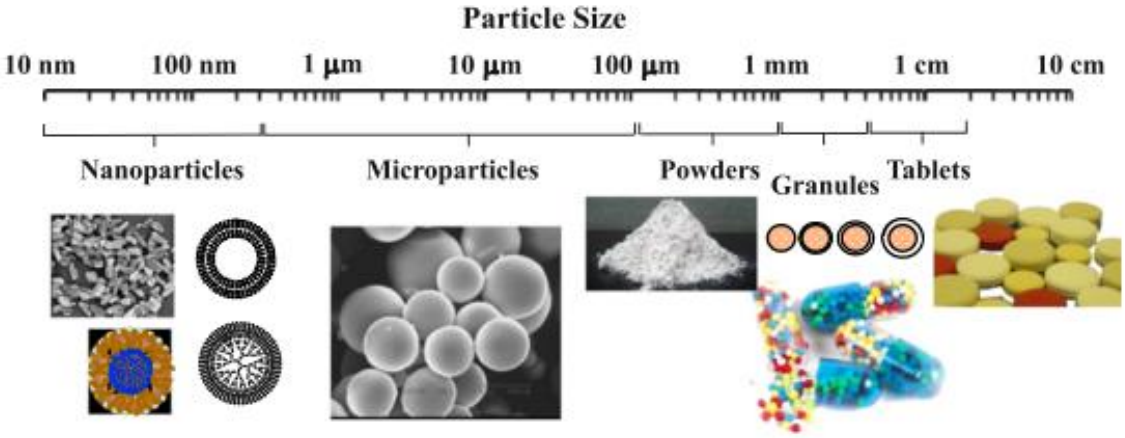

Figure 1.3. Sizes of common pharmaceutical treatments[24]. Reprinted from Chemical Engineering Science, 125, Byung Kook Lee, Yeon Hee Yun, Kinam Park. Smart Nanoparticles for drug delivery: Boundaries and opportunities, 158-164., Copyright 2015, with permission from Elsevier.

Encapsulating the drug within the nanoparticle provides opportunities to enable controlled (e.g., steady-state), predictable, and sustained release of the drug, protect the drug from rapid degradation and thus extend its half-life *in vivo*, permit low level dosing of active agent with reduced systemic biodistribution and effect, and provide a much lower

footprint in terms of vehicle degradation byproducts and associated toxicity[27–29]. NPs thus have attractive prospects to improve efficacy of drug-based treatments[30].

Our lab has recently designed biodegradable polylactic co-glycolic acid(PLGA)-polyethylene glycol (PEG) NPs for sustained (>6 months), predictable, and steady release of DOX locally within the AAA wall at very low doses (i.e., 1/100th of the useful oral dose or 1-20 μg/ml) at which we found DOX to continue to inhibit MMPs but, in addition, also stimulate elastogenesis[23]. A unique feature of the NP design is the incorporation of pendant cationic amphiphile functional groups on the NP surface that augment elastin regenerative repair by **a)** enabling NPs to hydrophobically interact and bind to the exposed elastin core of disrupted elastic fibers at the site of tissue repair, **b)** stimulating elastin precursor synthesis, crosslinking and fiber formation by aneurysmal SMCs, and **c)** inactivating elastolytic MMPs[23]. Through the independent but synergistic effects of the functionalized PLGA nanocarriers and their released drug (DOX), the DOX-NPs are able to shift the balance between elastic matrix biosynthesis (elastogenesis) and elastin breakdown (elastolysis) to facilitate robust and lasting buildup of stable and mature elastic fibers at the AAA tissue site. Despite these highly promising outcomes, further innovation in NP design is required to actively target these NPs in an efficient manner to the AAA wall following simple intravenous (IV) infusion. The focus of this thesis is to explore one such antibody-based active targeting strategy.

1.4. Problem statement and thesis objectives

The objective of this thesis is to develop an antibody-based modality for active targeting and improved retention of our DOX loaded, anti-proteolytic, and pro-matrix

regenerative NPs to/within the matrix-disrupted AAA wall, without adversely compromising their functional effects. Potential NP targets are cysteine proteases overexpressed in AAA tissue. Of particular interest within the family of cysteine proteases is the group of enzymes termed cathepsins. These proteins have been associated with many physiological processes including cartilage proteoglycan degradation, ECM regeneration and embryonic development[13]. The cathepsin family includes enzymes that target both elastin (elastases) and collagen (collagenases); these include cathepsin S (cat S), cathepsin K (cat K), cathepsin L (cat L), and cathepsin V (cat V). Even though cathepsins have been associated with a wide range of physiological processes, overexpression of cathepsins has only been recently linked to formation and growth of AAAs[14,16]. While the role cathepsins play in AAA formation is still not completely understood, their high level of expression both in AAA tissues and in serum/plasma of AAA patients, makes them a useful biomarker for early diagnosis of AAA formation, growth assessment, and a potential target for drug delivery to the AAA wall[16].

The specific aims of this study are:

1. To determine if functionalization of the NP surface with a cathepsin K antibody improves their targeting and uptake to the AAA wall without change in their physical and functional pro-regenerative/anti-proteolytic properties *in vitro* and in *ex vivo* culture models.
2. To assess trans-endothelial migration of Ab-functionalized NPs from the lumen to the AAA wall and benefits of $\alpha_v\beta_3$-integrin antibody tagging for this purpose.

3. To generate initial evidence of successful delivery of the cathepsin K Ab-modified NPs to AAAs in a rat model following intravenous infusion.

1.5. Organization of thesis

Chapter 2 presents an extensive literature review to provide background on the structure of vasculature, abdominal aortic aneurysm etiology and progression, a detailed explanation of current treatment options for AAAs and their limitations, nanoparticle uses in various treatments and how to apply nanoparticles to the treatment of AAAs. Chapter 3 presents comprehensive experimental methods used for *in vitro* and *in vivo* treatment with antibody-modified NPs. Chapter 4 outlines and interprets the results and provides interpretations of these results. Chapter 5 explains the limitations and future work to further advance the use of antibody modified nanoparticles in the treatment of AAAs.

CHAPTER II

BACKGROUND

2.1. Vascular physiology

The vascular system is a complex network of blood vessels that delivers oxygenated blood from the heart to tissues in the body to support their proper function. Arteries are exposed to drastic increases in blood pressure following each ventricular contraction. They respond by expanding with increased pressure and relaxing with decreased pressure to propel blood forward between heartbeats. Expansion of the major vascular conduit leading from the heart, the aorta, controls the pressure spike from each heart contraction and evens out the blood flow in smaller vessels[31]. In cross-section, the walls of blood vessels are composed of three major layers – the tunica intima, the tunica media, and the tunica adventitia (**Figure 2.1**). These layers have distinct cell types and extracellular matrix (ECM) composition that allows them to perform specific functions and change under certain physiologic conditions. The demand for blood and nutrients varies widely between tissues but can rapidly change in the same tissue under different environmental conditions. The vascular system is well adapted to meet these varying demands and arteries play a key role in controlling blood flow[31].

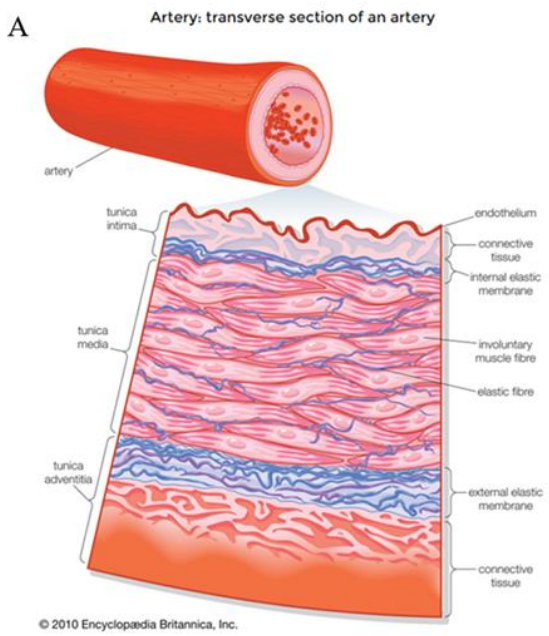

Figure 2.1. The artery is composed of three separate layers all with different compositions and functions[32,33]. Adapted from Encyclopedia Britannica Online.

2.1.1. Tunica Intima

The tunica intima is the innermost layer of the blood vessel, adjoining the lumen, and consists of endothelial cells (ECs) and the subendothelial matrix[34]. The subendothelial layer consists of a specialized ECM or basement membrane comprised of collagen type IV, laminin and proteoglycans[35]. In the artery wall, the monolayer of ECs respond to increased fluid shear stress due to blood flow by releasing specific factors such as nitric oxide or prostacyclin that incite relaxation of smooth muscle cells (SMCs) surrounding the intima layer[31].

The role of endothelial cells in the tunica intima is to serve as a barrier, affect vasodilation, and influence thrombotic events. The ECs act as a selective barrier by controlling the passage of particles into and out of the bloodstream. The control of particle

passage is due to the ECs ability to change the adherens and tight junction complexes between cells[36–38]. Beyond their role as a barrier, ECs play a role in responses to tissue damage as well as an anti-thrombotic function to prevent thrombosis and blockage of the artery[36,39]. The release of adhesion molecules and cytokines into the blood stream recruit leukocytes to repair tissue damage. To regulate thrombotic events in the blood vessel, the ECs release various molecules to inhibit or promote the activation of platelets and the coagulation cascade[36]. Besides the release of molecules that regulate coagulation, ECs release various factors to control vasodilation[40]. The endothelium releases factors such as nitric oxide (NO) and prostacyclin (PGI_2) to induce dilation of the artery or thromboxane (TXA_2) and endothelin-1 (ET-1) to cause constriction. The vasoactive factors released by the ECs target the smooth muscle cells in the tunica media to change the vessel diameter[40].

2.1.2. Tunica Media

The tunica media, the middle layer of the artery, is mostly comprised of vascular smooth muscle cells (SMCs) surrounded by another basement membrane and ranges in thickness from 0.03 mm in mice to 1.12 mm in humans[35,41]. In the tunica media of the aorta, elastin and collagen are precisely oriented forming defined layers. The layers of thick elastin, termed lamellae, are seen as concentric plates with thin elastin fibers connecting the elastin layers. Between the layers, collagen is present and aligned circumferentially and while the elastin fibers are connected, there are no connections between the collagen and elastin[41]. This arrangement of elastin and collagen could present a challenge in regeneration of the vascular wall especially concerning the crosslinking of elastin and not of collagen. The SMCs are located between the elastin lamellae and the

interactions between cells, elastin and collagen produce the viscoelastic properties of the aorta[41].

The SMCs in the arteries respond to changes in blood pressure through the myogenic effect. In response to elevated pressure, the SMCs contract narrowing the artery while maintaining a constant blood flow downstream. Chronic high pressure in the arteries causes the SMCs to remodel the vascular wall by increasing its thickness helping to resist pressure. However, this remodeling can disrupt the elastic matrix and decrease the capability to withstand sudden pressure changes[31]. Disruption of the elastin in the artery wall can alter the SMC phenotype and generate a cascade of problems for the ECM. SMCs remain in a quiescent contractile state in mature arteries but can differentiate under certain conditions such as injury or repair[42]. *In vitro* experiments confirmed the role of elastin in regulating SMC proliferation, migration and differentiation. Elastin significantly inhibits SMC proliferation and migration while maintaining the contractile phenotype[42,43]. Results from several studies have determined elastin is not only vital for artery recoil but plays a regulatory function through SMC proliferation[42,43].

2.1.3. Tunica Adventitia

The tunica adventitia, the outermost layer of the artery, composed of connective tissue, small blood vessels and nerve endings is a structural support for the tunica media[44]. While the main function of the adventitia was considered to be support, it is now understood to play an important physiological role in vascular function. In diseases where vascular function has been affected, noticeable changes in structure and biochemical composition are observed. Removal of the adventitia from rat carotid arteries decreases

contractile capabilities and increases the endothelium function suggesting its role in vascular function[44]. Even though the adventitia surrounds the artery it can affect other layers. Adventitial fibroblasts may be substitutes for the endothelial cells in regulating artery tone or the source for proliferating cells in the intima caused by atherosclerosis[45]. Overall, the tunica adventitia plays a role in vascular function beyond its structural support of the tunica media.

2.2. Composition and structure of the extracellular matrix (ECM)

The ECM of the aorta wall plays a major role in determining its mechanics and regulating biology of the contractive vascular cells. The ECM is comprised of several protein components which vary between the different tunic layers. The two major structural components of the ECM of the vessel wall are collagen and elastin[34]. The integrity of the ECM is maintained by contacting vascular cells (smooth muscle cells, fibroblasts) which are capable of limited matrix remolding.

Both collagen and elastin play a vital role in determining vascular mechanics. Elastin is responsible for the initial change in modulus when the vessel undergoes expansion at physiologic pressures. The elastic lamellae expand during increased pressure because of their low stiffness compared to collagen. However, under increasing strain the modulus increases due to the collagen fibers. At super-physiologic pressures, the collagen fibers begin to carry the load under the strain in order to maintain the aorta shape[46,47]. Eventually, the strain in the wall will become greater than the collagen strength and the wall will rupture. Under diseased conditions, the mechanics of the wall are altered so lower strain can cause greater strains leading to increased stiffness (**Figure 2.2)**[46].

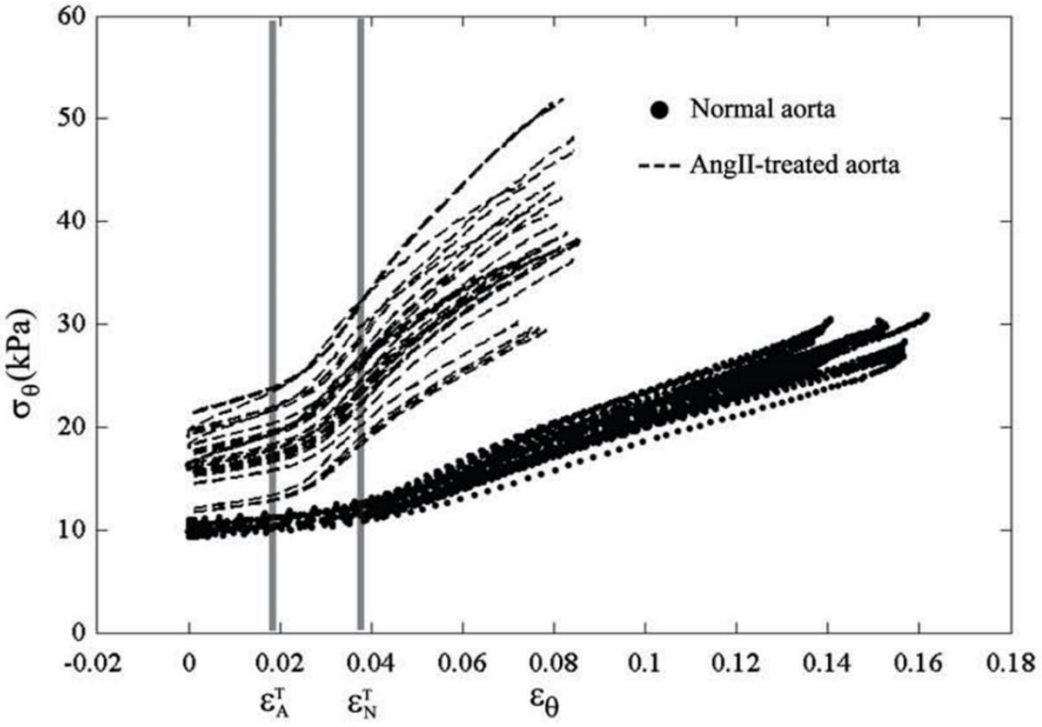

Figure 2.2. The stress-strain curve of a healthy and disease-simulated aorta[46]. The normal aorta can withstand greater strains than the injured aorta. Reprinted from Ultrasonics, 50, Asawinee Danpinid, Jianwen Luo, Jonathan Vappou, Pradit Terdtoon, Elisa E. Konofagou, In vivo characterization of the aortic wall stress-strain relationship, 654-665, Copyright 2010, with permission from Elsevier.

2.2.1. Collagen

Collagen is one of the most abundant proteins in the ECM of connective tissues. There are as many as 16 different types of collagen but three types – I, II, and III – make up more than 80 percent of the collagen in the body[48]. Collagen was thought to be only secreted by fibroblasts but now it is well understood that numerous cell types generate different collagen structures and this may play an important role in regeneration of the collagen matrix. This is noticed in the varying deposition of collagen types in the different tunics and in arteries of different sizes. Collagen is found in the tunica intima and adventitia but is limited in the medial layer. However, no matter the structure and type of

collagen, the function remains the same, that is to help tissues withstand stretching forces to prevent their rupture.

Collagen, similar to many other secreted proteins, is synthesized as precursor molecules. These chains are transported to the rough endoplasmic reticulum and undergo processing leading to formation and alignment of disulfide bonds between the precursor molecules to generate a triple helix structure[48]. This triple helix conformation domain and the interactions between these domains help stabilize these aggregates to form larger networks. The triple helix of collagen is characterized by the interweaving of three helical polypeptide chains. This forms a coiled coil structure where, due to steric reasons, the center of the helix is comprised of only glycine (Gly) residues. The amino acid sequence of these helices follows a similar pattern of Gly-X-Y allowing for the Gly to remain in the center of the helix. Glycine is found in the center of the helix due to the single hydrogen atom while the other two amino acids provide stability. Any other sequence of amino acids would disrupt the triple helix formation [49].

After secretion of this triple helical structure into the extracellular space, both terminal regions of the propeptide are removed allowing the collagen to polymerize into fibrils[48]. As mentioned before, the interactions of the helix domains stabilize the aggregates and this is due to the side chains of the X-Y amino acids in the polypeptide. The side chains of the X and Y amino acids are facing outside of the helix allowing for lateral interactions mediated by the crosslinking enzyme lysyl oxidase (LOX) (**Figure 2.3**)[48–50]. The crosslinks occur between helices and are critical for collagen function and strength. The various collagen types allow collagen to generate a wide range of structures.

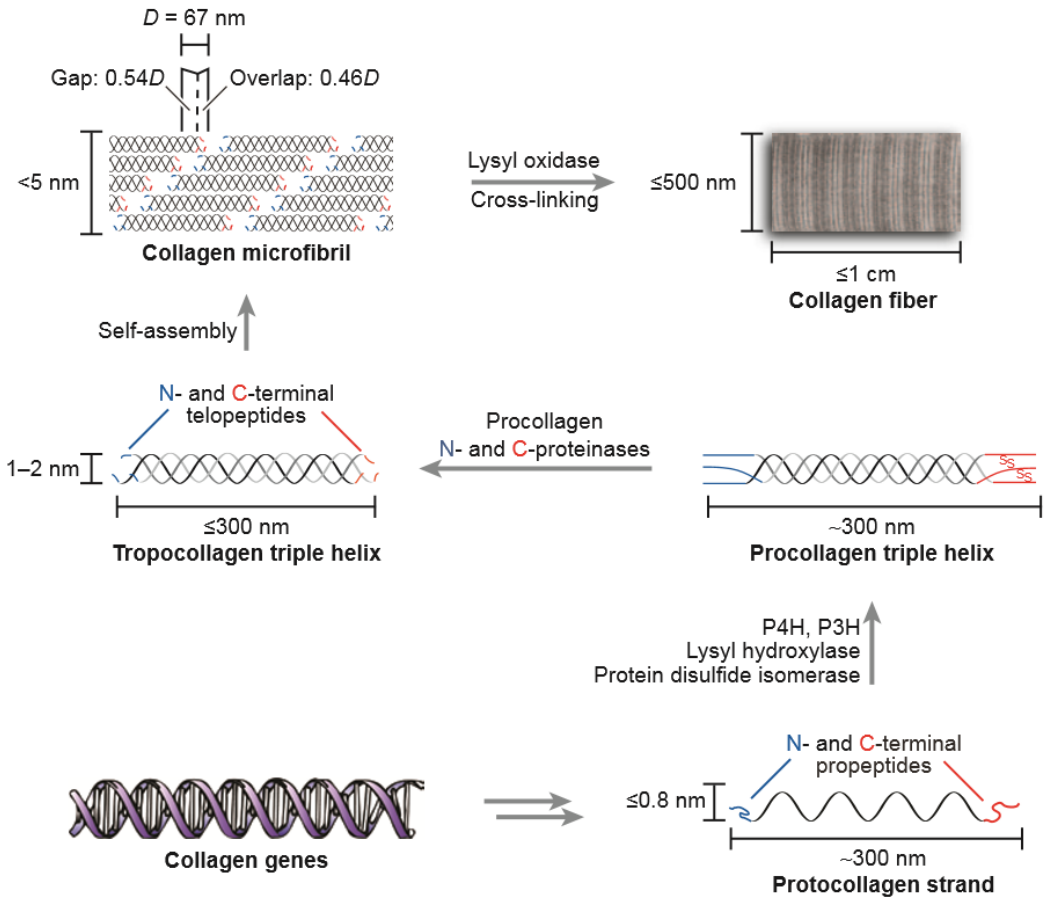

Figure 2.3. Synthesis of collagen fibers[50]. Collagen monomers can aggregate to form several types of structures with various mechanical properties[49]. Adapted from Shoulders and Raines. Annu. Rev. Biochem. (2009). 78: 929-58.

2.2.2. Elastin

Elastin is a key protein component of the elastic matrix which provides stretch and recoil properties to the vessel wall to accommodate blood flow during systole and to maintain blood pressure during diastole [42,51]. In the major arteries such as the aorta, elastin comprises ~50% of the tissue dry weight. In the aorta wall, elastin is found mainly in the tunica media and is responsible for artery recoil. Artery recoil was attributed to SMCs and elastin but comparing recoil of arteries with and without smooth muscle cells have shown similar recoil properties. This suggests the cells do not play a major role in the contraction

of the artery after expansion but rather elastic fibers are the major contributor. This is further confirmed in cases of mutations of the elastin gene (e.g., supravalvular aortic stenosis, cutis laxa, Williams Syndrome)[52–54]. The mutations in the elastin gene causes loss of function or complete gene deletion. In these mutations, the elastic lamellae in the aorta wall are fewer or disrupted leading to various degenerative vascular conditions and early mortality[52].

The elastic matrix is generated through the crosslinking of tropoelastin monomers but the process is complex (**Figure 2.4**). The elastic fiber is made of two distinct components, the microfibrils and an amorphous elastin core. The amorphous elastin core is synthesized from tropoelastin monomers encoded by an ELN gene expressed by fibroblasts, smooth muscle cells, and endothelial cells during childhood but expression quickly decreases during adulthood[51]. The tropoelastin monomers bind to the elastin-binding protein which protects the monomers from degradation and phase separation while transporting the monomers to the cell surface[55,56]. Once the complex is secreted from the cell, the elastin-binding protein interacts with other complexes causing the release of tropoelastin. The elastin-binding protein returns to the intracellular space to bind more tropoelastin monomers and repeat the process[51]. Outside of the cell, the hydrophobic domains of tropoelastin interact generating aggregates on the cell surface. While this appears to be the beginning of the elastic fiber formation, studies have shown the interaction of the C-terminal of tropoelastin with microfibrils is the first step and is required to assemble an elastic fiber[51]. Eventually, tropoelastin production and crosslinking at the cell surface generates a sufficiently sized aggregate and it is released from the cell surface where it migrates through the extracellular matrix and deposits into the microfibril

scaffold[56]. Lysyl Oxidase (LOX) plays an important role in the crosslinking of tropoelastin leading to stable and non-reducible crosslinks[34,57]. Once tropoelastin has been crosslinked, its production is reduced and there is minimal turnover of the mature elastin[55].

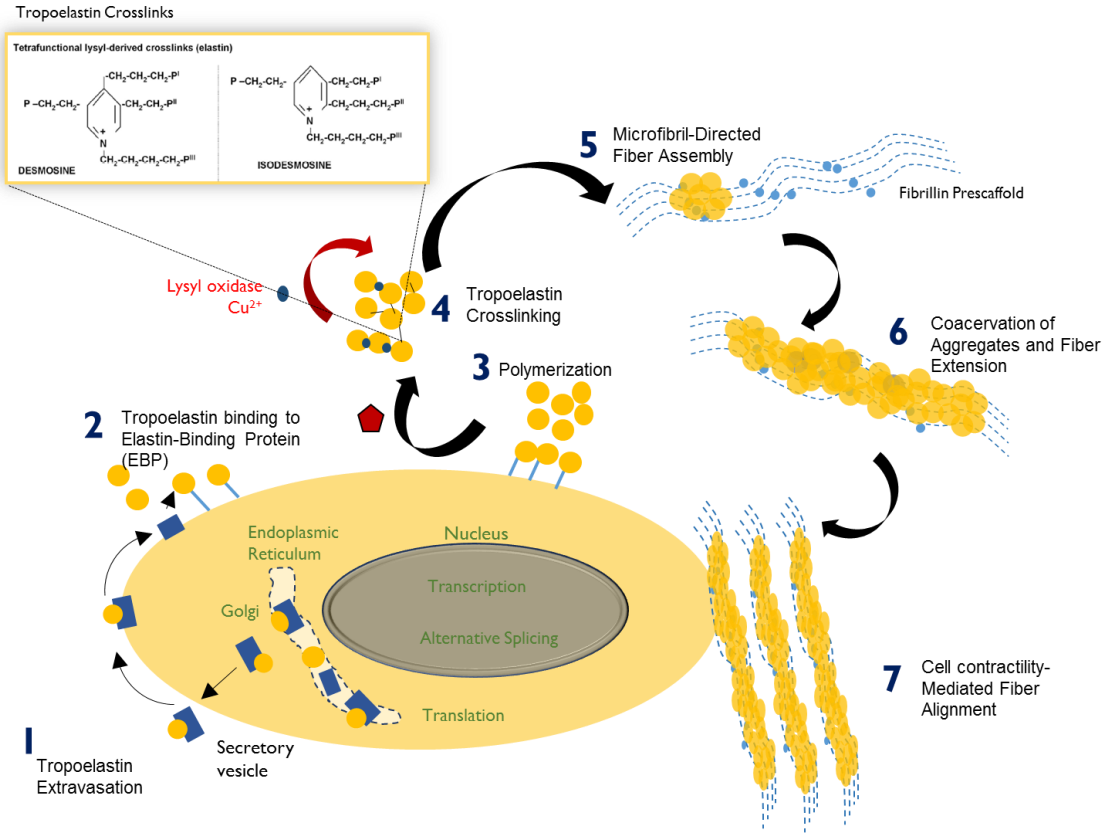

Figure 2.4. Schematic showing steps in elastic fiber assembly. (1) The tropoelastin is secreted to the cell surface and binds to the Elastin-Binding Protein (2) before being polymerized (3) and released. The tropoelastin undergoes cross-linking by lysyl oxidase (4) and is directed to assembly onto microfibrils (5) followed by aggregation and fiber extension (6) resulting in an aligned fiber (7).

As mentioned earlier, elastic fiber formation requires microfibrils and the microfibrils act as a scaffold and support elastin deposition. The microfibrils are composed of fibrillin, specifically fibrillin-1, which is expressed across all tissues. Fibrillin-1 is secreted and undergoes a cleavage step required for the multimerization to create structures at the cell surface. Microfibrils are stabilized by a fibronectin network that promotes

interactions with other microfibril proteins where the microfibrils will be crosslinked leading to further stabilization of the structure[51]. The aggregates associated with the microfibril continue to crosslink leading to larger aggregates generating a functional fiber. LOX, an oxidative deaminase, and Cu^{2+}-dependent enzyme, oxidizes the deposited elastin until the coacervates coalesce and integrate onto the microfibril scaffold[51].

Elastin production is significant during prenatal and neonatal development but decreases by adolescence. Fortunately, the half-life of cross-linked elastic matrix is ~74 years so once the matrix has been deposited in childhood, it withstands an entire lifetime. This long half-life is due to the high degree of crosslinking and tightly packed nature of elastin due to its hydrophobicity. Since elastin production is limited in adult SMCs and there are no current treatments to increase elastin production, disorders wherein accelerated enzymatic disruption of the elastic matrix occurs are difficult to treat or reverse[33]. However, the advances in tissue engineering and regenerative medicine may soon make it possible to stimulate elastin regeneration and repair such scenarios.

The tertiary structure of elastin varies across tissue types and this is due to the forces the tissue experiences. The ELN primary transcript is heavily spliced causing isoforms that range from 60 to 75 kDa. Six exons of human tropoelastin have been identified to be alternatively spliced affecting the hydrophobic and hydrophilic domains. The splicing may be tissue dependent as multiple isoforms have been identified in aorta and lungs[56]. The different splicing of domains may explain the differences in elastin structure in tissues. For example, the aorta in humans may have as many as seven isoforms of elastin and this could affect the elastin structure[56]. In the medial layer of the aorta, the elastin is arranged in concentric fenestrated lamellae while in elastic cartilage the elastin is configured in three-

dimensional honeycomb-like structures and this could be the result of splicing[51]. Differently, in aortic valves, elastin is present as continuous and fenestrated sheets in the ventricularis layer and is found as discrete/loose fiber networks in the skin[58]. The structure and content of elastin in various tissues are listed in **Table 2.1**.

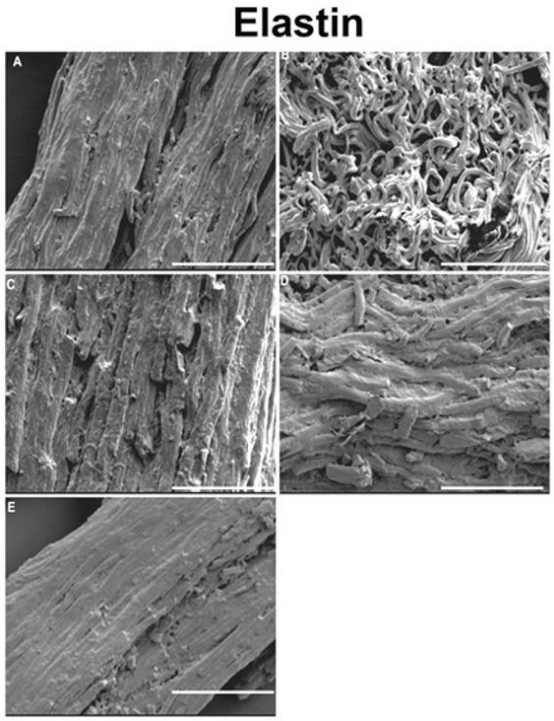

Figure 2.5. SEM images of bovine elastin fibers treated with cathepsin K. Panel A shows untreated elastin with visible fibers. Panel B shows elastin treated with cathepsin K in which disruption is visible. Panel C, D, and E highlight the elastin treatment with a mutant cathepsin K to highlight exosite importance in degradation[59]. Adapted from Sharma *et al*. Biochem J. (2015), 163-173.

Table 2.1. Elastic Fibers in Various Tissues and Elastin Content as Percentage of Dry Weight[51].

Tissue Type	Elastin Content (%)	Configuration of Elastin
Aorta	50	Concentric lamellae
Elastic Ligaments	75	Fibers
Lung	30	Lamellar sheets
Skin	5	Fibers
Tendon	4	Long Fibers

Mature elastin is stable under normal physiological conditions and exhibits minimal remodeling and turnover. However, specific cell types (e.g., SMCs, fibroblasts) express elastin degrading enzymes (proteases, elastin matrix metalloproteinases, cysteine cathepsins) at low levels[14,60,61]. **Figure 2.5** highlights the degradation of elastin due to cathepsin K. **Figure 2.5.A** shows the untreated elastin fibers in bovine. **Figure 2.5.B** shows the disrupted elastin fibers following treatment with cathepsin K. **Figure 2.5.C**, **Figure 2.5.D**, and **Figure 2.5.E** were treated with mutant variants of cathepsin K to highlight the importance of the exosites in the degradation of elastin[59]. Such basal expression of elastin degrading enzymes is required for cells to migrate through the ECM. However, under certain diseased conditions or following tissue injury, these enzymes are expressed at greater levels leading to rapid elastic matrix degradation. These elastases are generally released by recruited inflammatory cells and cytokine-activated fibroblasts in the vessel wall in several diseases (atherosclerosis, abdominal aortic aneurysms)[55].

2.2.3. Cathepsins

The extracellular matrix is a complex structure that continually undergoes remodeling and modification. The restructuring of the ECM can be caused through enzymatic or non-enzymatic processes[62]. The enzymatic processes were thought to be controlled by MMPs and serine proteases until recent discoveries have shown cysteine cathepsins also contribute to the degradation of the ECM. Cysteine cathepsins were originally described as intracellular proteases requiring an acidic environment for optimal activity but under certain conditions, the cathepsins are secreted into the extracellular matrix and maintain their protease activity[12,62].

Cysteine cathepsins fall under a more diverse cathepsin group composed of various catalytic proteases. The broad cathepsin group includes serine cathepsins, aspartic cathepsins and cysteine cathepsins. Sequencing of the human genome has revealed 11 cysteine cathepsins, the most abundant in the cathepsin group[62]. Cathepsins are expressed in an inactive state and following transport to the lysosome are activated by removal of the predomain which can be autocatalytic or catalyzed by other proteases. One important factor in autocatalytic activation is the presence of negatively charged surfaces that induces a conformational change allowing for processing by other proteases[62,63]. The presence of a negatively charged surface such as an appropriately modified nanoparticle surface, could increase cathepsin activation so it is necessary to design their surface characteristics to achieve desired anti-proteolytic and pro-matrix properties for therapy.

Cysteine cathepsin structure consists of two domains: a left domain composed of three α-helices and a right domain composed of a β-barrel. Located between these two domains is the active site, a cysteine and histidine residue[62,64]. Substrates bind to the cathepsin through interactions with both domains and along the active site cleft. The binding of cysteine cathepsins and substrates exhibit a greater specificity compared to other cysteine proteases and this is attributed to the interaction of multiple binding sites. Specifically, cathepsin K exhibits specificity for proline and glycine residues and this matches the cathepsin K specificity for ECM proteins[62]. The role of cathepsin K on the degradation of the ECM proteins will be discussed later.

The localization of cathepsins in lysosomes was thought to retain the cathepsins as intracellular proteases but they can be released into the cytosol and translocate to the cell surface or are secreted into the extracellular space. Once in the extracellular space, cysteine

cathepsins degrade proteoglycans and fibrous proteins such as collagen and elastin (**Table 2.2**). Several proteases have been identified that degrade collagen including MMPs and cysteine cathepsin K[65]. The degradation of collagen was thought to be originally caused by multiple cysteine cathepsins until recently when cathepsin K was shown to be the only physiologically relevant collagenase. While other collagenases (MMPs, elastase) cleave the triple helix in collagen at a single site, cathepsin K can cleave the helix in multiple sites as well as cleave the telopeptide region producing collagen monomers making cathepsin K more potent[62,65]. Another important component of the ECM, elastin, can be degraded by cathepsin K - known to be a potent elastase. Cathepsin K contains two hydrophobic exosites which play a major role in stabilizing the interactions between elastin and cathepsin K. The structure of cathepsin K makes it a potent elastase due to the exosites being located far from the active site and the binding of elastin to these sites positions the cleavage susceptible region of elastin in the cathepsin active site[62].

Table 2.2. Cysteine cathepsins and their extracellular matrix substrates[62].

ECM Protein	Active Cathepsin	Resulting pathophysiology
Type I collagen, Type II collagen	Cathepsin B, K, L, S	Osteoarthritis, cardiovascular diseases, lung disease, cancer
Elastin	Cathepsin K, L, S, V	Cardiovascular diseases, cancer
Fibronectin	Cathepsin B, L, S	cancer
Aggrecan	Cathepsin B, K, L, S	Osteoarthritis
Type IV collagen	Cathepsin B, S	Cancer progression, intestine trauma

Cathepsin K plays a crucial role in the degradation of collagen and elastin and this has an impact on vascular diseases. Vascular diseases, such as atherosclerotic plaque and atheroma, have shown significantly increased cathepsin K expression[14]. This is significant because atheroma is associated with regions of increased elastin degradation. Beyond their

role in atherosclerosis and degradation of the ECM, cathepsins play an important role in immune response. One such disorder, where the breakdown of elastin and immune response lead to disease progression, is an abdominal aortic aneurysm (AAA) in which cathepsin K contributes to AAA formation and growth[12,62]. The role of cathepsin K in AAA progression was confirmed using cathepsin K deficient mice. In these mice, the aorta was infused with elastase to induce an aneurysm. Compared to the control mice, the cathepsin K deficient mice were protected from AAA formation[66].

2.3. Abdominal aortic aneurysms (AAAs)

Abdominal aortic aneurysms are localized expansions of the aorta that develop and grow to rupture due to the chronic overexpression of matrix metalloproteinases causing irreversible breakdown of vessel wall elastic matrix. Clinically, AAAs are defined as aortal expansions with a 50% increase over the healthy aortal diameter (2.5 cm)[67]. Elderly male smokers are at the greatest risk for developing an AAA, however the prognosis for women is worse with a rupture rate 4 times greater[68]. The formation of an aneurysm has been linked to genetic factors but environmental factors play a major role in development.

2.3.1. AAA etiology

The formation of an AAA can be caused by multiple factors such as trauma, chronic hypertension, vasculitis or inflammatory diseases (e.g. atherosclerosis) but this accounts for a small portion of aneurysms. Therefore, most aneurysms have been termed "non-specific" but atherosclerosis has been associated with most cases of AAAs[69]. However, this view on the development of the abdominal aortic aneurysm has been challenged but in all cases, there is an initial stimulus that induces AAA formation. **Figure 2.6** shows the

etiological progression for AAA development and growth to rupture. An AAA occurs after an initial injury or stimulus causing the recruitment of inflammatory cells to the aortic wall (**Figure 2.6.1** and **Figure 2.6.2**). The inflammatory cells release proteases, specifically matrix metalloproteinases (MMPs) (**Figure 2.6.3**). The proteases degrade the fibrillar collagens and elastic matrix generating elastin fragments[69]. The elastin fragments have a two-fold effect. First, the fragments recruit more inflammatory cells thereby creating a positive feedback loop. The elastin fragments recruit leucocytes to the aortic wall as well as inflammatory cytokines, chemokines and prostaglandins[69]. Additionally, the elastin fragments induce smooth muscle cell apoptosis which further results in decreased elastin content (**Figure 2.6.4**). The SMCs express several ECM proteins and therefore are critical in vascular wall remodeling so the depletion of SMCs limits remodeling capabilities. Further, the loss of elastin content exposes the SMCs to an increased stress and to compensate, the cells produce additional collagen matrix (**Figure 2.6.5**). The collagen in the tunica adventitia plays a critical role in the resistance to rupture once the elastin in the tunica media has been broken down[69]. The increased collagen production leads to a transient wall thickening but is susceptible to proteolytic breakdown, eventually leading to wall thinning (**Figure 2.6.6**). The stress in the aortic wall becomes greater than the wall strength and the aneurysm ruptures (**Figure 2.6.7**).

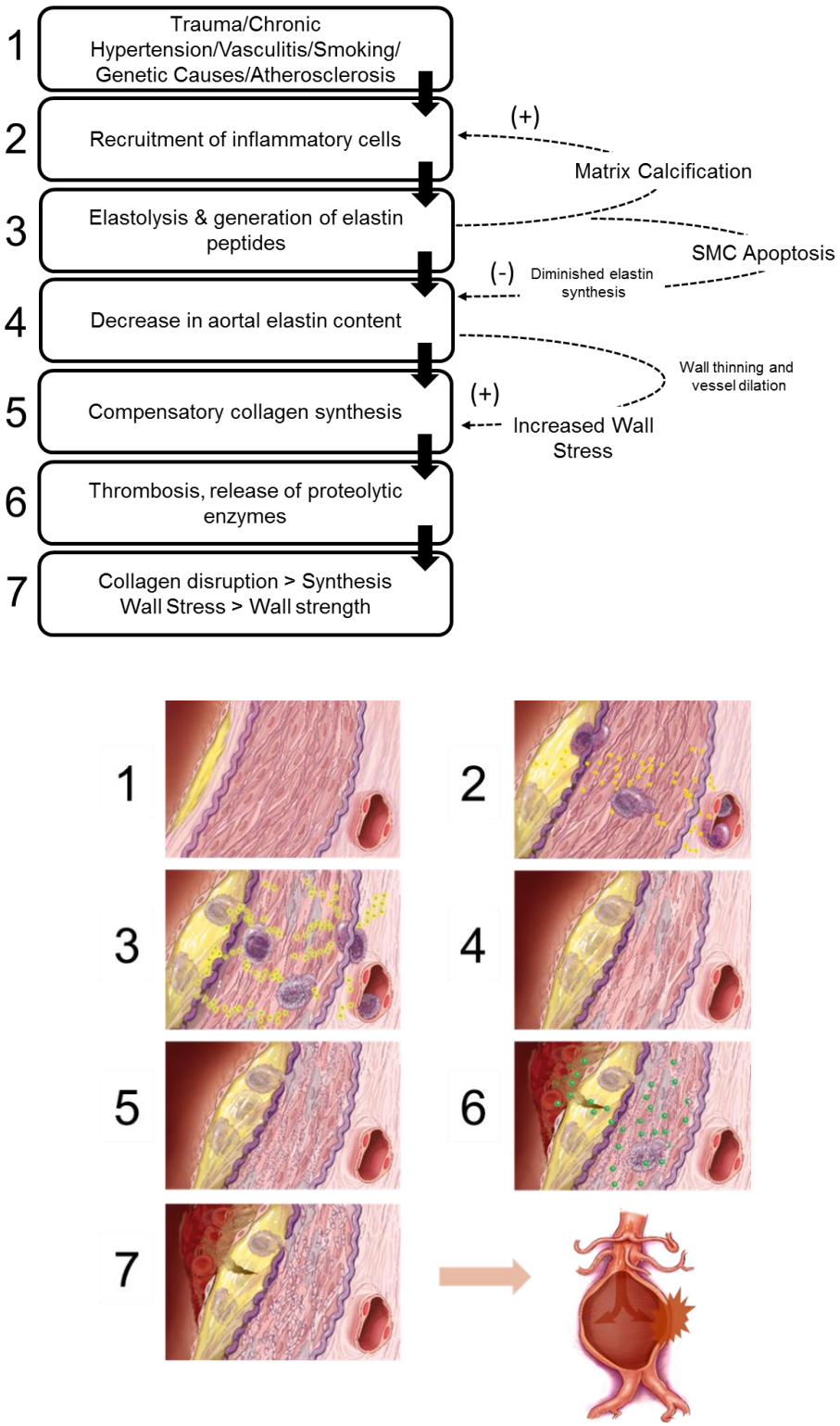

Figure 2.6. Abdominal aortic aneurysm etiology in which an initial injury stimulus (1) begins aneurysm development and ends with wall thinning (7) and eventual aorta rupture.

The inflammatory cells recruited to the aneurysm site release proteases, specifically matrix metalloproteinases (MMPs). As previously mentioned, aneurysms were thought to be caused by atherosclerotic disease but recently there has been a shift citing MMPs to play an important role in formation[68]. The release of MMPs was originally thought to occur from the inflammatory cells recruited to the aneurysm site but experimental data has shown activated endothelial cells, aortic SMCs and adventitial fibroblasts are secreting MMPs into the ECM. When MMPs are secreted into the ECM, they are in an inactive form and converted to an active form. This may be a useful target for treating AAAs. Inhibiting the activation of MMPs in the aneurysm tissue could significantly decrease growth and formation. Specifically, MMP-9, expressed by macrophages in the aneurysm, has an affinity for the breakdown of elastin and collagen and the increase in aneurysm diameter may be correlated to its expression[68]. Therefore, identifying inhibitors of MMPs may be a crucial part of aneurysm treatment.

2.3.2. Treatment options for AAAs

Identification of high risk populations and preventative, imaging-based screening has enabled the detection of aneurysms early in development. At the present time, management of small AAAs is limited to passive ultrasound or magnetic resonance imaging (MRI) every six months and endovascular/surgical repair at a critical size (>5.5 cm) (**Figure 2.7**) when rupture risk greatly exceeds surgical risk[10,20]. Even with screening and treatments, AAA rupture still remains one of the largest causes of death in the elderly[11]. There are currently several treatments available for large AAAs to reduce the risk of rupture but the risks and benefits of repair need to be compared to the risk of rupture before elective surgery should be considered. The two most common surgeries are endovascular stent

graft and open repair. Each treatment has its advantages and limitations so careful consideration should be used when determining the appropriate course of treatment as one treatment may be better suited for some individuals. Since current treatment options are limited to large AAAs, developing a novel treatment for small AAAs has several advantages. Treatment of small aneurysms reduces the risks associated with surgeries especially in elderly patients and can reduce the costs of late intervention. Arresting and regressing the aneurysm growth at an early stage can prevent future hospital visits. Another advantage of treating small AAAs is the increase in quality of life. With the current options of passive monitoring and no active treatment, the quality of life is decreased due to the waiting period for aneurysm growth.

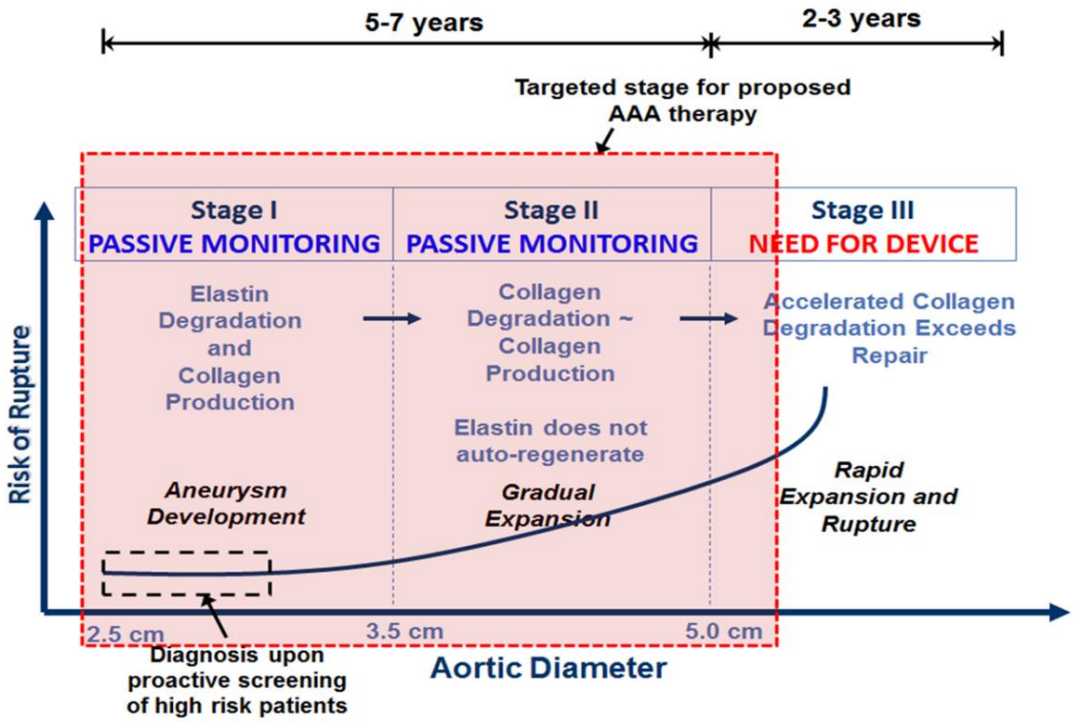

Figure 2.7. Current treatment options vary for small and large aneurysms due to the risk of rupture. Small aneurysms are managed using passive imaged-based monitoring until the size and risk of rupture increases and surgery is performed.

2.3.2.1. Endovascular stent graft repair

Endovascular stent graft repair of AAAs is a common treatment option and a viable alternative to other surgical options as it is less invasive. In endovascular aortic repair (EVAR), the aim is to reduce the risk of rupture by excluding the aneurysm sac from the circulation of blood (**Figure 2.8)**. Excluding the aneurysm sac is accomplished through the placement of a bypass graft in the aorta[18,67]. Most abdominal aortic aneurysms (~70%) can be treated with endovascular repair due to their morphology but there are several limitations to this treatment. If the patient is under 60 years of age, the use of a stent graft is not suggested since there is lack of long-term durability data. Other limitations include a short, conical proximal neck or thrombus within the proximal neck[18]. In EVAR, a catheter with the stent graft is inserted into the femoral artery and guided to the aneurysm. Once the stent graft is located at the aneurysm site, the graft is expanded and attached to the aorta wall. The stent graft is checked with dye to ensure there is no blood leakage around the area. The catheter is removed leaving the stent graft in place and the femoral artery site sutured together leaving only small incision sites[70].

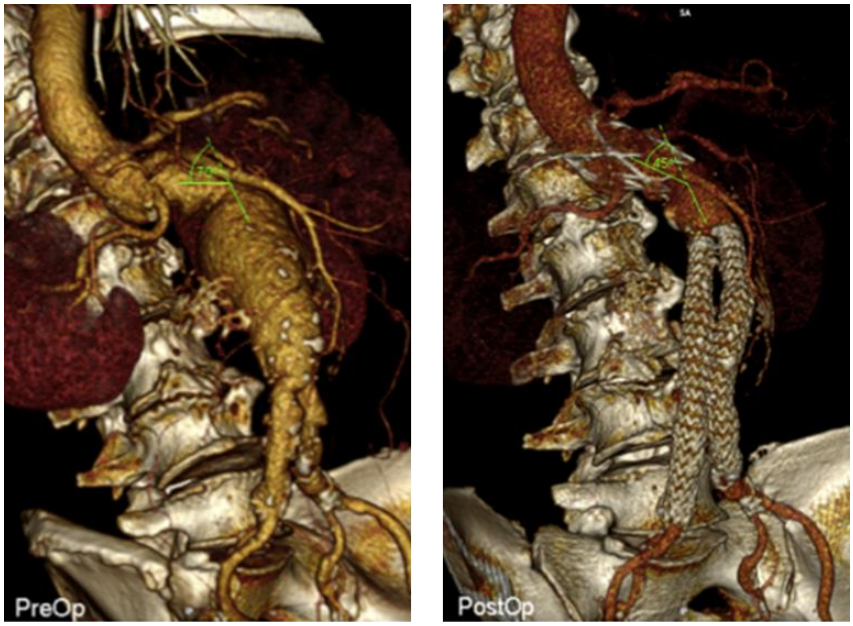

Figure 2.8. A 3-D reconstructed image of an AAA. The left image shows a 7.9 centimeter aneurysm and the image on the right shows the stent graft in place after surgery[71]. Reprinted from European Journal of Vascular and Endovascular Surgery, 52, C.V. Ioannou, D.K. Tsetis, Going Beyond Current AAA Neck Angulation Limitations of the Ovation Ultra-low Profile Polymer-filled Stent Graft, 172, 2016, with permission from Elsevier.

While minor complications can arise from surgery itself, once the endovascular graft has been surgically implanted complications caused by the stent can occur. These complications include renal failure, endoleak, occlusion, migration or infection of the stent graft. While only occurring in 1 to 3% of patients, bowel ischemia is a serious complication with a 50% mortality rate within 1 month[72]. In bowel ischemia, thrombotic deposits can be dislodged while the stent is being positioned and can travel into the renal or lower-limb circulation resulting in patchy ischemia[72]. Similar to bowel ischemia, renal artery occlusion is another complication that occurs in less than 5% of cases. In renal artery occlusion, the stent covers the renal arteries preventing blood flow but if detected early enough the stent can be repositioned without any major side effects[72]. While these complications are associated immediately after surgery, the most common complications

occur within a few months after the surgery. Limb thrombosis can occur in as many as 40% of cases with the underlying cause being stent-graft kinking[72].

2.3.2.2. Open aneurysm repair

Similar to endovascular stent graft repair, open repair utilizes a stent graft to remove the aneurysm sac from circulation, however the main difference is the delivery method of the stent. In open aneurysm repair, an incision is made down the center of the abdomen to expose the aorta. Once the aorta is exposed, it's clamped above and below the aneurysm site to stop blood flow. The aneurysm sac is cut open and a graft inserted. The graft is sutured to the aorta wall effectively connecting the two together. The clamps are removed, the aorta wall wrapped around the graft and sutured together before suturing the abdominal incision[70].

The open repair procedure is more invasive than EVAR. Although EVAR shows a lower 50-day mortality but the long term results of open repair may outweigh the risks[73]. Common complications are similar to EVAR with open repair including bleeding, small bowel obstruction, hernia and ischemia. The complications were corrected through reintervention surgery and most reintervention surgeries were not related to the graft but were directly related to the laparotomy[73]. However, patients undergoing EVAR had a 3-4 times greater risk of graft related complications or reintervention compared to patients undergoing open repair. EVAR carries an advantage in mortality after the first few years but that advantage disappears over time. This may be due to the late rupture of patients treated by EVAR[73]. While EVAR may have reduced initial risks, open repair requires less follow-up monitoring. The open repair surgery is considered 'for life' and requires

minimal to no follow-up monitoring because there are so few late complications. Finally, the reintervention rate for EVAR was 41% while the reintervention rate for open surgery was 9%[73]. The long term complications and costs associated with open repair compared to EVAR require more data to decide which treatment option should be considered the standard[73].

2.4. Restoring elastin homeostasis in the AAA wall

The goal of tissue engineering and regenerative therapies is to utilize patient derived cells or other biological materials/resources to generate functional, structural and biological mimics of native tissues on demand to restore or replace diseased tissues. Tissue engineering of the aorta would be an exciting breakthrough in the treatment of AAAs and could become the standard treatment. The extracellular matrix of the aorta is complex and requires significant remodeling to treat aneurysm formation so it is necessary to explore several tissue engineering options.

Current advances in restoring elastin include improvements in cell therapies and drug-based MMP inhibition. The use of cell therapies provide unique treatment opportunities. Autologous cell therapies reduce the likelihood of an immune response as the cells were taken from the patient but the applications of use for these cells can be limited. Another possible cell therapy utilizes stem cells. Stem cells can be generated from multiple sources and tailored to a specific application but can be severely limited in clinical settings. To use stem cells in a clinical setting, the culture conditions and processes must be highly regulated to ensure there are no variations in the cell types and complications upon implantation. Drug-based MMP inhibition is an attractive option for restoring elastin

because once the drug has been FDA approved it can be mass produced. Unlike cell therapies, using drug-based therapies limits the time spent in hospitals since most drugs are administered at home. However, the use of drug-based MMP inhibition has its drawbacks. MMP expression and activity is required as part of the natural remodeling within the body so the high concentrations of MMP inhibitors, especially from oral dosing, can have systemic side effects.

2.4.1. Elastin regeneration using stem cells

Terminally-differentiated, healthy adult vascular SMCs are poorly elastogenic and thus cannot be used for cell therapy towards regenerative repair of AAAs. However, a viable option to regenerate the elastic matrix is through the use of stem cells. Elastin production is upregulated during fetal and transiently during vascular injury responses, both representing the only scenarios when this occurs. However, the elastin produced by inflammatory cells fails to crosslink into elastic fibers[74]. Stem cells and their SMC-like progenitors/derivatives are purported to play a key role in elastogenesis in such scenarios. For effective cell therapy, it is crucial to identify stem cells and derivative phenotypes that will stimulate the diseased SMCs to produce elastic matrix, inhibit matrix proteolysis, and also serve as an additional source of new elastic matrix to augment elastin regeneration at the AAA site.

There are several sources of adult stem cells available for cell therapy including those from bone marrow, peripheral blood, and adipose tissue. The advantages of using these autologous stem cells is the lack of immune rejection. These adult stem cells (mesenchymal stem cells or MSCs) are multipotent meaning they can differentiate into

several distinct cell lineages. MSCs have been successfully differentiated into adipocytes, chondrocytes, osteocytes, and SMCs[75–78]. They provide several advantages for cell therapies for matrix regeneration including their immunoregulatory property – which prevents activation of the immune response through inactivation of surface markers in T-lymphocytes even upon allogeneic implantation[79]. Multiple studies have suggested MSCs stimulate matrix regeneration and tissue recovery which may play a crucial role in treating AAAs. One such study determined when rat aorta tissue from an AAA model was co-cultured with MSCs, there was an increase in elastin fiber formation compared to controls. Another study found when the MSCs were differentiated before culturing with aneurysmal tissue, the differentiated MSCs increased the gene expression of elastin and elastin deposition[79,80]. Both of the studies suggest MSCs and differentiated MSCs have the ability to stimulate the regeneration of elastin when cultured with aneurysmal tissue. It is crucial now to determine if MSCs can produce the same results *in vivo* and develop a means to deliver the MSCs to the AAA.

2.4.2. Elastin regeneration using pharmaceuticals

There are currently no FDA-approved or proven drugs for AAA treatment and almost none capable of regenerating elastic matrix. Drugs in the development pipeline for small AAA management including statins[5,67,81], tetracyclines[21,60,69], and ACE inhibitors[82] only seek to attenuate chronically overexpressed proteases in the AAA wall. This can at best lead to slowed AAA growth. There is no impetus to regenerative repair of disrupted elastic matrix structures. There is therefore, a compelling need for non-surgical, drug based therapy targeting and reversal of pathophysiologic changes in the AAA wall which include chronic proteolysis and lack of autoregenerative repair of the elastic matrix.

The inhibition of MMP activity is an area of focus for treating AAAs so there have been great strides in producing synthetic MMP inhibitors such as batimastat, doxycycline and other tetracycline derivatives[69]. Synthetic MMP inhibitors reduced aneurysm dilation in several rat models by controlling the inflammatory response[83,84]. The MMP inhibitors produced promising results but also caused adverse musculoskeletal side effects likely related to their systemic biodistribution and high dosing levels[85,86]. Recently, tetracycline based drugs have been shown to inhibit MMP activity[87]. One of the most studied is the drug, doxycycline (DOX), which has been shown in several animal models of AAAs to slow AAA development[87]. When DOX was administered subcutaneously in a rat elastase injury AAA model, there was a significant decrease in AAA growth while oral dosing showed a 50% reduction in AAA growth rate in Ang II mice[88]. DOX has also shown promise in clinical trials in slowing AAA growth upon oral therapy[89,90]. This was primarily attributed to decrease in elastolytic MMPs 2 and 9 in the AAA wall. Despite this promise, the clinical outcomes are inconsistent largely due to difficulties in delivering a defined steady dose of the drug in the AAA wall, sustaining its effect in the long term, and rapid drug inactivation associated with oral dosing. In addition, the high oral DOX doses (30-50 mg/kg/day) necessary to ensure sufficient levels of MMP inhibition in AAA tissue causes body wide side effects (e.g., musculoskeletal pain, inflammation, tendonitis) and also further inhibits the already poor elastin regeneration and crosslinking in the AAA wall[85]. This negates prospects to restore elastin homeostasis in the AAA wall, a key requirement for arresting or reversing AAA growth.

In recent studies in our laboratory, we have shown that at much lower doses (< 5 μg/ml) than that achieved in the AAA wall with oral dosing (50 mg/kg/day equivalent to

~50 µg/ml), DOX maintains its anti-MMP effects but also has significant pro-elastogenic effects as well, which was a novel finding (Unpublished Data). To achieve this benefit, modalities to ensure targeted, predictable, sustained and steady low level DOX dosing locally in the AAA wall are necessary. Nanoparticles (NPs) offer several advantages for this purpose.

2.5. Nanoparticles for drug delivery

Nanoparticles provide unique opportunities as a treatment option that are not available in pharmaceutical and cell-based therapies. Limitations of pharmaceuticals include short half-lives, poor bioavailability, or physical and chemical instability[91]. These limitations have led researchers to study nanoparticles in which many of the poor characteristics from pharmaceuticals can be overcome and a unique environment for drug delivery can be designed[25]. One of the largest obstacles to overcome in using stem cells as a therapy is their delivery to the treatment site as well as the processing and purifying of the cells along with tracking the cells *in vivo*. Upon implantation in the body, stem cells have the ability to form tumors if not properly controlled or delivered to the target area. This gives nanoparticles (NPs) a distinct advantage as a therapy option. However, to be an effective drug delivery system, the NP needs to consist of three components: the core material, the ability to carry therapeutics, and surface modifiers[92].

2.5.1. NP characteristics

An important feature of NPs is their composition or core material[92]. Most NPs are formulated using either synthetic or natural polymers however other nanoparticles have been generated using lipids to create liposomes or silica and alumina to create inorganic

nanoparticles[25]. In liposomes, the hydrophilic head and hydrophobic tail of the lipid aggregate to form an aqueous core in which therapeutics can be encapsulated[92]. The use of liposomes to deliver therapeutics is currently the most developed system with the largest number of clinical trials and treatments in the marketplace. However, this may be due to the relatively new focus on polymeric materials compared to liposomes[92]. Synthetic polymers have advantages over natural polymers in terms of drug delivery and release kinetics, but the formulation conditions of synthetic polymers limits their use. Some common synthetic polymers used are biodegradable polymers such as poly (D, L-lactide-co-glycolide) (PLGA) and polylactide (PLA).

Both PLGA and PLA polymers are approved by the US Food and Drug Administration for safe human use and are commercially available in various molecular weights and co-polymer compositions[25,93]. PLGA is one of the most commonly used polymers due to the degradation products being lactic acid and glycolic acid which are easily metabolized in the body through the Krebs cycle thereby limiting the toxicity of the NPs[93,94]. The biodegradable polymers can be formulated to encapsulate drugs, proteins or DNA and act as a delivery system. The polymer matrix helps prevent degradation of the encapsulated drug and allows for control over drug release. Drug release is altered by changing the ratio of drug to polymer or changing the polymer molecular weight and composition[95].

Nanoparticles are submicron-sized polymer particles and have characteristics different than bulk materials[24,96]. Nanoparticles have advantages over larger sized particles when targeting cells for treatment. Studies comparing uptake of particles with different sizes have shown the smaller particles are more readily taken up by cells. The uptake of

100 nm particles was 15 to 250 fold greater than particles of 1 and 10 μm with respect to a rat intestinal model. It was also found particles in the nanometer range could pass through the submucosal layer while larger particles were trapped in the epithelial lining[28]. The uptake of the NPs into the cell are mediated through a concentration and time-dependent endocytosis process. Once the NPs are taken up by the cell, and depending on their surface charge, undergo a surface charge change from anionic to cationic in the endo-lysosomes disrupting the membrane. The NPs do not remain in the endo-lysosomes for long because of this and they quickly enter the cytoplasm following uptake[95]. The surface characteristics of the NPs play a vital role in their escape from the endo-lysosomes which effects their retention within the cell. The surface characteristics that influence NP retention in the cytosol include zeta potential and hydrophilicity[95].

2.5.2. Tissue targeting of NPs

While the use of nanoparticles as drug delivery systems has been around for decades, extensive research has recently been conducted on utilizing nanoparticles as a targeted delivery system[24]. Nanoparticle surfaces have been modified to effect the characteristics, uptake, and localization of the nanoparticles within the body with much research conducted to identify surface modifications to increase nanoparticle targeting to specific tissues. Nanoparticles have been altered with several types of surface modifications such as polysorbate 80, PEG, and DMAB to change nanoparticle behavior in the body[23,26]. Studies have shown the polysorbate 80 modification can help move drug-loaded nanoparticles through the blood-brain barrier while the addition of heparin or DMAB can increase nanoparticle retention in arteries[26]. Previously published research from our group, indicates modifying the surface with DMAB increases the nanoparticle

binding to elastin[23]. Each surface modification imparts a unique characteristic on the NP so it's critical to understand how to utilize these qualities. Utilizing these qualities of surface modification, targeting of nanoparticles to specific regions of the body is an area of great promise and continued interest.

Targeting of NPs to specific tissues/regions is an area of interest in treating diseases. Extensive research has been conducted on treating cancer using NPs loaded with chemotherapeutic drugs. In order to target cancer cells, chemotherapy drugs are administered at high concentrations which has adverse side effects on the entire body but with NPs the systemic concentration could be significantly decreased and thereby reduce side effects. For example, paclitaxel loaded NPs were modified with transferrin to increase cellular uptake. After a week of treatment *in vitro*, the modified NPs demonstrated an 80% decrease in cell growth compared to a 40% decrease with unmodified NPs. The largest change was in comparison to the paclitaxel solution where there was a 20% decrease in growth[95]. This demonstrates the effectiveness of using NPs as delivery systems.

In order to increase the targeting capabilities of NPs, understanding the biology of the target tissues is crucial. Movement of nanoparticles into the intracellular space is accomplished through endocytosis which can be separated into three subtypes: phagocytosis, pinocytosis and receptor mediated endocytosis. Phagocytosis occurs in select cell types such as macrophages and neutrophils where particles up to 10 μm are ingested. However, in pinocytosis submicron particles can be ingested by nearly all cell types leading to greater access of nanoparticles to cells[25]. This difference in uptake depends on nanoparticle size and can be used to differentiate which cells ingest nanoparticles. Expression of receptors that can be targeted can change depending on tissue

type and disease state so identifying these changes allows for the determination of specific targets[25,28]. Finally, modifying the surface of the NP with a primary antibody has been linked to increased targeting capabilities (**Figure 2.9)**. The functionalization of the NP surface with an antibody can be accomplished through adsorption of a compound to the surface or though covalently linking the compound to the polymer[95]. In this method, the active site of the antibody is left free to bind to target compounds. If the target is a receptor on the cell surface, this can effectively increase the localization of the NP to the tissue.

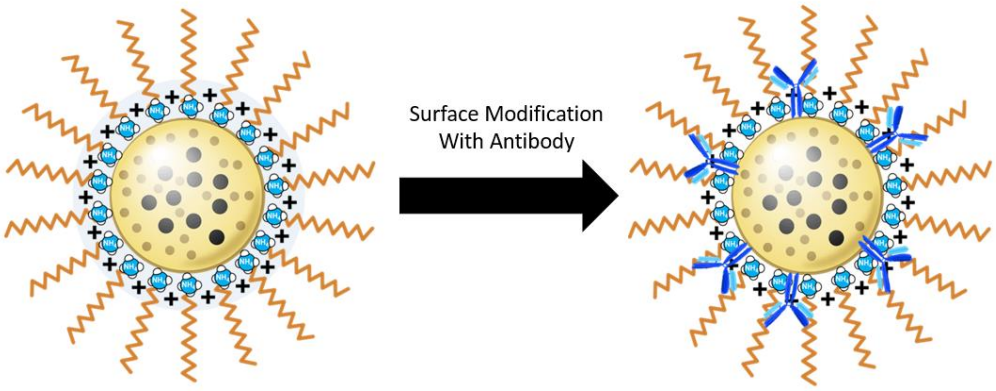

Figure 2.9. Functionalization of nanoparticles using a primary antibody surface modification.

Another option being actively explored to increase localization of NPs to specific tissues utilizes the loading of iron oxide into NPs to generate superparamagnetic iron oxide NPs (SPIONs). Currently, there are imaging contrast agents commercially available utilizing SPIONs to improve imaging of the liver and GI tract. Recently, SPIONs have been combined with therapeutics to investigate improvement in treatments with the use of magnetic fields[97–99]. The combination of imaging agents and therapeutics is described in more detail in the following sections. Iron oxide particles alone are hydrophobic leading

to aggregation resulting in large clusters. The formation of these large clusters is undesirable so modifying the surface or encapsulating the iron oxide particles in polymer scaffolds reduces this effect and increases their effectiveness as a treatment option[100]. The use of SPIONs originally focused on delivery of peptides, DNA molecules and chemotherapeutic drugs but the focus has shifted to using SPIONs to fight infections, as anti-inflammatory reagents, or dissolve blood clots[99]. Several studies have confirmed the capabilities of SPIONs to target tumors with concentration increases from 4 to 200 times greater. Using an implanted permanent magnet, cytotoxic SPIONs were successfully localized to solid tumors in hamsters. The localization to the tumor increased the anti-tumor activity as well as eliminated unwanted side effects such as weight loss[99]. Despite the attractive NP targeting possibilities with SPION incorporation, there are regulatory challenges due to the designation of SPION-loaded/modified polymer NPs as combinatory devices and questions regarding long-term safety and biodistribution of the SPIONs, which need to be elucidated. Therefore, alternative safer and less complex targeting modalities (e.g., antibody or peptide mediated targeting) must be explored.

2.5.3. Environmental activation of NPs

While surface modifications improve targeting, activation of nanoparticles as drug delivery systems has become an area of interest as it helps create specificity in drug release. Activation of these nanoparticles can occur through two main modes – exogenous and endogenous activation[101,102]. In exogenous activation, the NPs are stimulated through an external stimuli to control drug release. This can be accomplished through magnetic fields, light, or radio frequencies[91,101,103]. Using an external stimulus provides greater control of drug release allowing for high concentrations of therapeutics to be delivered in specific

sites while limiting systemic concentrations. Also, the use of magnetic fields to stimulate drug release can serve a dual purpose as it can help localize NPs to the treatment area as well as control drug release. Using magnetic guidance for SPIONs has shown potential in experimental cancer treatments through an increase in drug concentration in solid tumors[102]. Beyond the localization of nanoparticles, the magnetic field has shown to trigger the drug release in certain materials. In a ferrogel composed of micelles encapsulating SPIONs and a hydrophobic drug, the applied magnetic field causes the micelles to be squeezed through SPION interactions thereby releasing the drug[102]. The use of SPIONs and the MRI may play a vital role in treating AAAs as the treatment and imaging could be performed at the same time. Passive monitoring of the AAA is currently performed and the addition of the SPIONs could provide a treatment option without significantly changing current treatments.

The endogenous activation relies on a variety of differences between healthy and diseased tissue to cause drug release from NPs. Factors that influence the activation of NPs include pH, enzyme concentrations, and hypoxia[91,101,103]. Using pH sensitive NPs allows for targeting and triggered release of drugs in specific organs as well as specific intracellular compartments. pH sensitive NPs utilize two main strategies for triggered release including polymers that undergo conformational or solubility changes when the pH changes as well as systems where the bonds in the polymers are broken when the pH changes[102]. Another possible endogenous activation system relies on enzymatic activity. In pathological conditions, the expression of enzymes may be altered and can be a target for NPs. Studies have reported the use of peptide sequences susceptible to MMPs as linkers in nanoparticles. As MMPs cleave the peptides, the encapsulated drugs are released

thereby limiting their release to areas of high MMP concentration[102]. The use of enzyme concentrations to control drug release could provide valuable treatment options within AAAs as several proteins have been identified to be over expressed in the diseased tissue.

2.5.4. NP treatments and diagnostics

Treatments using nanoparticles have been approved for human use by the FDA to treat disorders ranging from cancer to infection but the number of options is relatively small[25,104]. However, there are a large number of clinical trials underway which could lead to a dramatic increase in nanoparticle treatments. One study published in 2013 evaluated the developments of nanoparticles and their use in clinical trials and found nearly 800 potentially relevant clinical trial results. Of these 800 clinical trials, 141 were unique products with approximately 40 already approved for use[104]. This number is expected to grow as interest in nanoparticles and nanomaterials increases.

Imaging is a large portion of diagnosing and the first step to treat many disorders. In medical imaging, there are two approaches: anatomic imaging to identify structural information and molecular/functional imaging to provide physiological and cellular information. Anatomical imaging does not always require contrast agents but for molecular imaging the contrast agents are essential. Imaging contrast agents include small molecules, proteins, and nanoparticles[105]. While most scans use small molecules as contrast agents, interest in nanoparticles has grown and led to new applications. These include intense and long lasting imaging signals, the ability to have different targeting strategies, theranostic capabilities, and detection by several imaging instruments. One of the most intriguing possibilities is the use of nanoparticles as theranostics in which the

imaging agent can also deliver therapeutics. The use of nanoparticles as theranostics has been studied with doxorubicin loaded ferumoxytol nanoparticles to treat cancer. The nanoparticles, or SPIONs, generate a signal when using MRI but may also be able to treat cancer by releasing the encapsulated doxorubicin[105]. More studies are confirming the increased localization of SPIONs to tumors using MRI which may eventually lead to improved drug delivery[106,107].

Apart from imaging agents, the use of nanoparticles has been extensively researched in the treatment of cancer. The most common treatment of cancer involves using one or more cytotoxic small molecules to kill cancer cells. Unfortunately, these small molecules do not recognize cancer cells specifically and will kill other cells types leading to many unwanted side effects[108]. To limit side effects, targeted therapy has been explored to reduce exposure to cytotoxic small molecules. Two modes of targeted therapy using nanoparticles have been explored including direct and indirect treatment methods. Indirect treatment relies on an immune response that causes cancer cell apoptosis or inhibits angiogenesis[108]. Nanoparticles loaded with cancer treating drugs have shown much promise. However, different drugs have different mechanisms of action and require delivery to specific target areas. Paclitaxel affects microtubules so it needs to localize in the cytoplasm where other drugs need to migrate into the nucleus to be effective[108]. In treating AAAs, the direct treatment method will provide the necessary cellular response to stimulate elastin regeneration.

Nanoparticles have been used as detection agents and treatment options for several vascular diseases including atherosclerosis and thrombosis[109]. As previously mentioned, the vascular wall is a complex and difficult tissue to treat and regenerate. The vascular

wall cannot be treated like many other tissues because of the large amount of blood flow. Administering a therapeutic drug directly does not induce therapeutic benefits due to rapid drug removal from the site as well as the short half-life of drugs in plasma. Also, conventional therapies for treating disorders in the vascular wall do not produce the desired results because many therapeutic agents are toxic at the dose required to be therapeutic as well as having systemic side effects[109]. This has led to much research into using nanoparticles as targeted drug delivery systems.

Using targeted drug delivery systems allows for low systemic concentration but high concentration in areas of interest as well as a sustained and controlled release that can be extended over a long period of time. The success of nanoparticles targeted to the vascular wall are affected by the size of the particle, the blood flow type, and the vascular wall shear rate. In this study, we aim to utilize targeted drug-loaded nanoparticles, with a sustained and controlled drug release, to stimulate regeneration of the disrupted elastic matrix associated with abdominal aortic aneurysms and investigate the efficacy of antibody based targeting on these NPs to the AAA wall with no adverse impact on their physical and functional properties, which are vital to effective regenerative repair of the AAA wall ECM.

CHAPTER III

MATERIALS AND METHODS

3.1. Induction of AAA in rat model via elastase infusion

All rat surgeries were performed with IACUC approval at the Cleveland Clinic (2016-1581). Acepromazine (0.5 mg/kg) was administered subcutaneously approximately 30 minutes before anesthesia induction. Elastase solution was prepared (20 Units/ml, Sigma) and stored on ice until use. Immediately prior to anesthesia induction, buprenorphine hydrochloride (0.03 mg/kg) was administered subcutaneously. The rat was moved to the anesthesia induction chamber (oxygen flow rate 1 L/min, 2.5% isoflurane) for 7-8 minutes until anesthetized.

Once anesthetized, ophthalmic eye ointment was applied to both eyes and the rat was placed on the surgery table and its nose inserted into the nose cone. The isoflurane concentration was reduced to 2% for the duration of the procedure. The hair from the abdomen was clipped, the abdominal skin sterilized using betadine and alcohol scrubs with application proceeding from the inside out. Immediately before the surgical procedure, 0.25% Bupivacaine (2-8 mg/kg; analgesic) was administered subcutaneously at the

incision site. The abdominal cavity was exposed by a laparotomy and the abdominal wall was held open using retractors. The exposed intestines and other internal organs (stomach, pancreas, liver, etc.) were removed to outside the body cavity and were covered with moistened sterile gauze to prevent drying during the procedure. Using fine forceps, the aorta was exposed by removing surrounding fat and connective tissue. Once the aorta was exposed, images were taken using a microscope to allow for diameter determination. The blood flow in the aorta was stopped by using a plastic clamp at the proximal and distal ends of the abdominal aorta. Care was taken to ensure the aorta was completely sealed before infusion. A micro cannula system (Braintree Scientific, Inc.) was inserted into the aorta without passing completely through. The elastase solution was infused through the micro cannula system into the aorta and held for 20 minutes. The solution was removed from the aorta and the cannula system removed. The aorta was either sutured or glued shut using a fibrin glue (Tisseel Fibrin Sealant; Baxter; Westlake Village, CA). Images of the aorta were taken post treatment. The intestines were replaced and the abdomen sutured with the muscle layer sutured using 4-0 vicryl non-absorbable nylon stiches in a running pattern and the skin sutured using 4-0 silk stiches in an interrupted pattern. During suturing, the isoflurane was reduced to 1.5% to begin recovery.

The animal was removed from isoflurane and placed on a heating pad (37 °C) to continue recovery before being moved to its cage and placed on a towel to finish recovering. While in the cage, food and a water-gel pack was placed on the cage floor to allow access during recovery. Once the animal has recovered enough to move around the cage, the cage was returned to the BRU. Pain from the surgery is managed through twice daily injections of buprenorphine hydrochloride (0.03 mg/kg) for 72 hours.

3.2. Isolation and culture of SMCs from elastase perfusion-induced rat AAAs

EaRASMCs were harvested from multiple (n = 3) adult male Sprague-Dawley rats at 14 days following elastase infusion, as we have previously published[110]. The AAA segments were isolated following laparotomy and the intimal layer scraped off. The medial layer was then separated from the adventitia, dissected into ~0.5 mm long slices, and rinsed in sterile phosphate-buffered saline (PBS). The tissue was digested in DMEM-F12 medium (Invitrogen, Carlsbad, CA) containing 125 U/mg collagenase (Worthington Biochemicals; Lakewood, NJ) and 3 U/mg elastase (Worthington Biochemicals) for 30 min at 37 ^{o}C, centrifuged (400*g*, 5 min) and cultured in T-75 flasks in DMEM-F12 medium containing 10% v/v of fetal bovine serum (FBS; PAA Laboratories; Etobicoke, Ontario) and 1 % v/v of penicillin-streptomycin (PenStrep; Thermo Fisher; South Logan, UT). At 70% confluence, the primary EaRASMCs from individual rats (n = 3) were pooled and passaged.

Primary rat aortic SMCs (RASMCs; healthy cell controls) were isolated from aortae of multiple (n = 3) healthy Sprague-Dawley rats, in a similar manner as previously described for EaRASMCs, pooled, passaged, and used in culture experiments at passage <6.

3.3. Experimental design for cell culture

In order to study the effect of cathepsin K antibody-conjugated DOX-NPs and unconjugated NPs on cellular elastic matrix synthesis, EaRASMCs were seeded at 30,000 cells per well in wells of a 6-well plate, and cultured for 21 days in DMEM-F12 medium supplemented with 10% v/v fetal bovine serum (FBS) (Invitrogen), 1% v/v PenStrep (CCF

Cell Services), and 50 ng/ml of tumor necrosis factor-α (TNF-α) (Thermo Fisher; Waltham, MA). The media from each well was removed and centrifuged (5 min, 12,000 RPM) to pellet the NPs. The NPs were re-suspended in fresh medium before being added back into each well. Culture groups included untreated EaRASMC cultures (treatment control), EaRASMCs cultured with unconjugated NPs loaded with 2% w/w of doxycycline hyclate (DOX; Sigma Aldrich), and cathepsin K Ab-conjugated NPs loaded with 2% w/w of DOX. In the latter cases, the NPs were added on Day 1 following an overnight incubation at a concentration of 0.2 mg/ml.

To study the migration of Ab-modified NPs through the endothelial cell layer, human umbilical vein endothelial cells (HUVECs) were cultured in vascular cell basal media (ATCC; Manassas, VA) supplemented with Endothelial Cell Growth KIT-VEGF (ATCC; **Table 3.1**). The HUVECs were seeded at 30,000 cells per well or per collagen-coated PET membrane (Millipore; Billerica, MA) and cultured with the medium supplemented with vascular endothelial growth factor (VEGF; 5 ng/ml; ATCC). The cells were stimulated with 10 ng/ml of TNF-α for subsequent experiments (immunofluorescent labeling and treatment with NPs and Ab-modified NPs). The cells were cultured with the NPs at a concentration of 0.2 mg/ml.

Table 3.1. Endothelial Cell Growth Kit-VEGF added to 500 ml of vascular basal media for the culturing of HUVECs.

Component	Volume	Final Concentration
rh VEGF	0.5 ml	5 ng/ml
rh EGF	0.5 ml	5 ng/ml
rh FGF basic	0.5 ml	5 ng/ml
IGF-1	0.5 ml	15 ng/ml
L-glutamine	25.0 ml	10 mM
Heparin sulfate	0.5 ml	0.75 Units/ml
Hydrocortisone hemisuccinate	0.5 ml	1 µg/ml
Fetal Bovine Serum	10.0 ml	2%
Ascorbic Acid	0.5 ml	50 µg/ml

3.4. Formulation of fluorescein-loaded, Alexa Fluor 633-loaded, VivoTag® 800-loaded, DOX-loaded, and blank PLGA NPs

Poly (DL-lactic-co-glycolic acid) (PLGA; 50:50 lactide: glycolide; Durect Corporation; Birmingham, AL) NPs loaded with fluorescein (Chemicon; Temecula, CA), Alexa Fluor 633 (AF633) (Invitrogen; Carlsbad, CA), or VivoTag® 800 (PerkinElmer; Waltham, MA) were prepared using a double emulsion solvent evaporation technique. PLGA (50 mg) was dissolved in 2 ml of chloroform (Fisher Scientific, Fair Lawn, NJ) and 0.1 ml of a 1 mg/ml solution of fluorescein, AF633, or VivoTag® 800 was added. The mixture was emulsified on ice using a probe sonicator (Q500; QSonica LLC; Newtown, CT) for 30 seconds at an amplitude of 20% to form a water-oil emulsion. Similar to loading of the fluorescent dye, the DOX-loaded NPs were prepared using an aqueous DOX solution containing a 2% w/w ratio of DOX: PLGA and emulsified into the PLGA solution using a probe sonicator. For all of the NP formulations, 6 ml of an aqueous phase consisting of nanopure water and surfactant, didodecyldimethylammonium bromide (DMAB; Sigma-Aldrich, St. Louis, MO), was added and sonicated again for 60 seconds (30 seconds on – 10 seconds off - 30 seconds on) on ice at 20% amplitude to form the water-in oil-in water

double emulsion. The double emulsion was stirred for 16 hours at room temperature and desiccated for 1 hour under vacuum. The samples were separated by ultracentrifugation (35,000 rpm, 30 minutes; Beckman L-80, Beckman Instruments, Inc., Palo Alto, CA), the supernatant removed and the NPs washed with nanopure water to remove residual DMAB and unencapsulated loading compounds, sonicated to re-suspend the NPs, and a repeat ultracentrifugation (30,000 rpm, 30 minutes). Following the second ultracentrifugation step, the NPs were re-suspended in 6 ml of nanopure water and sonicated before aliquoting into cryovials. The cryovials were immersed in liquid nitrogen, to flash freeze the NPs, and stored at -80°C overnight. The NPs were lyophilized for 48 hours to obtain a dry powder. Samples were kept covered throughout this procedure to ensure the fluorescent dye did not undergo bleaching. Following the methods as previously described, blank PLGA NPs were formulated using DMAB as the surfactant.

3.5. Determination of NP size and surface zeta potential

Mean hydrodynamic diameters of the NPs were determined using a dynamic light scattering technique, and their mean zeta potentials (surface charge) were determined via a phase analysis light scattering technique using a commercial particle-sizing system (PSS/NICOMP 380/ZLS, Particle Sizing Systems; Santa Barbara, CA).

To determine the particle size, a small aliquot of the NPs (~ 5 µl) was diluted in nanopure water and placed in a small glass vial. The glass vial was wiped clean to ensure no interference. The glass vial was inserted into the particle-sizing system and the particle size was measured over a 2 minute cycle. The results were displayed as a Gaussian distribution. To determine the zeta potential, the NPs (~0.5 ml) was added to ~2.5 ml of nanopure water and transferred to the cuvette. The electrode was rinsed with deionized

water and placed on the cuvette. The cuvette and electrode were placed into the instrument and the electrode connected. Once the electrode is connected the zeta potential was measured over a 5 minute cycle.

3.6. Preparation of cathepsin K Ab-modified NPs

3.6.1. Adsorption of cathepsin K Ab to NP surface

Fluorescent dye loaded-NPs (AF633) were suspended in PBS (pH 7.4, 0.5 mg/ml) and a 490 µl aliquot of this was mixed with 10 µl of cathepsin K Ab (200 µg/ml; rabbit anti-rat; Santa Cruz Biotechnology, Inc.; Dallas, TX). A mixture containing 490 µl of the NP dispersion and 10 µl PBS was used as a control. These mixtures were stirred (2, 5, or 24 hours) and centrifuged (12,000*g*, 10 min) to separate the free antibody from NPs. The pellet containing cathepsin K Ab-adsorbed NPs were washed twice with PBS and re-suspended in 500 µl of PBS (pH 7.4).

3.6.2. Covalent conjugation of cathepsin K Ab to NP surface

1-Ethyl-3-(3-dimethylaminopropyl) carbodiimide HCl (EDC; Thermo Fisher; Rockford, IL), a cross-linking reagent, was used to generate a covalent bond between free carboxylic acids on the PLGA NP surface and the primary amine group on the cathepsin K Ab. The NPs were suspended in 2-(N-Morpholino)ethanesulfonic acid (pH 5.5, MES; Sigma-Aldrich) at a concentration of 0.5 mg/ml and 490 µl of this mixture was mixed with 10 µl of cathepsin K Ab followed by the addition of 100 ng of EDC . Two controls were run including one without EDC and one without EDC and antibody. The mixtures were stirred at 24^{o}C for 5 hours followed by centrifugation (10 min, 12,000 rpm) and the

supernatant discarded and the NP pellet washed two times with PBS (pH 7.4). The NPs were finally re-suspended into PBS to the desired concentrations.

3.7. Assessment of cathepsin K Ab incorporation on NP surface

3.7.1. Fluorescence spectroscopy to assess cathepsin K Ab binding to NPs

A fluorescein-tagged goat anti-rabbit secondary antibody (Chemicon, Temecula, CA), was used to qualitatively determine the relative binding of the cathepsin K Ab on the surface of the NPs. Cathepsin K Ab-modified NPs were treated with the secondary antibody (4 ^{o}C, 1 h, 1:500 dilution). The samples were centrifuged (12,000g, 10 min) and the pellets washed twice with PBS, to remove any unbound secondary antibody, and then re-suspended in 500 µl of PBS. Three 150 µl aliquots per sample were placed in the wells of a 96-well microplate. The fluorescence intensity due to fluorescein was measured (λ_{ex} = 493 nm and λ_{em} = 525 nm) using a SpectraMax M2e microplate reader (Molecular Devices, Sunnyvale, CA) as well as visual confirmation using a fluorescent microscope.

3.7.2. Measurement of cathepsin K Ab conjugation efficiency

The cathepsin K Ab was covalently conjugated to AF633-loaded NPs over 5 hours as described previously, with proper controls. Following conjugation and washing, an Alexa Fluor (AF) 546-conjugated donkey anti-rabbit (1:1000 dilution; Thermo Fisher Scientific) was used to fluorescently tag the NP-bound cathepsin K Ab (25 ^{o}C, 1 hour). Samples were centrifuged (12,000g, 10 min), washed twice with PBS, and re-suspended in PBS at a concentration of 0.5 mg/ml. Three 150 µl aliquots of each sample was added to a 96-well microplate and the fluorescence of fluorescein (λ_{ex} = 493 nm and λ_{em} = 525 nm)

and Alexa Fluor 546 (λ_{ex} = 556 nm and λ_{em} = 573 nm) were measured using a microplate reader. The NPs were aliquoted onto glass cover slips, mounted, and visualized on a microscope (Leica TCS SP5 II, Leica Microsystems, Inc., Buffalo Grove, IL) to detect cathepsin K Ab-conjugated NPs exhibiting both green (fluorescein) and red (AF 546) fluorescence.

3.7.3. Assessing retention of conjugated and absorbed cathepsin K Ab on NP surface

To determine whether chemical conjugation or physical adsorption resulted in stable binding of cathepsin K Ab to the NP surface, Alexa Fluor 633 (Invitrogen) was loaded into the NPs as previously described. Cathepsin K Ab modification of the NPs was performed as described above for both methods (Sections 3.6.1 and 3.6.2). An Alexa Fluor 488-conjugated goat anti-rabbit secondary antibody (1:1000 dilution; Invitrogen) was used to fluorescently tag the cathepsin K Ab. The NPs were centrifuged (12,000g, 10 min), washed twice with PBS, re-suspended in PBS (0.5 mg/ml) and a fluorescent microscope used to visualize the NPs exhibiting both red (AF633) and green (AF488) fluorescence.

To determine fluorescence intensity due to NP surface-bound cathepsin K Abs, a corrected total fluorescence (CTF) protocol was used. Briefly, individual NPs were selected using the drawing tool in ImageJ software® to obtain an integrated density for both red and green fluorescence. The integrated density was used to calculate the corrected total fluorescence at Day 1 and Day 14. The CTF is calculated by: (Integrated Density – (Mean Fluorescence of Background * Area of Selected NP)). To determine the ratio of FITC bound to the NP surface, the CTF of FITC (adsorption n = 132, n = 130 and conjugation n = 154, n = 207) was divided by the average CTF of AF633 for each test case.

3.8. Verifying cathepsin K overexpression by aneurysmal cells and their targeting by NPs

3.8.1. Assessing cathepsin K expression by EaRASMCs in culture

EaRASMCs (passage 3) and RASMCs (healthy cell controls) were seeded at 30,000 cells/well, and cultured for 2 weeks in six-well plates in DMEM-F12 medium containing 10% v/v FBS and 1% v/v PenStrep. Half of the EaRASMC cultures received medium supplemented with 50 ng/ml of TNF-α in order to simulate the inflammatory aneurysmal tissue environment.

For immunofluorescence visualization of cathepsin K expression, after a further 24 hours of culture, all cell layers were fixed in 4% v/v paraformaldehyde, permeabilized with Triton-100 (VWR International; UK) and labeled with the primary cathepsin K Ab (1:100 dilution) and a secondary AF 546-tagged secondary antibody (1:1000 dilution). DAPI (Vector Labs; Burlingame, CA) and AF488-Phalloidin (Molecular Probes; Temecula, CA) were used to stain the nuclei and actin cytoskeleton, respectively. The cell layers were imaged on a fluorescent and confocal microscope.

3.8.2. Assessing cathepsin K expression in matrix-injured arteries

Cathepsin K expression in elastase injured arteries (Lampire Biological Laboratories, Pipersville, PA) was compared to expression of the housekeeping protein, β-actin, using western blot. Porcine carotid arteries (n = 3) were infused with either elastase (20 units/ml, Sigma) or 0.9% v/v sterile saline. The end of each artery was clamped shut and a catheter was used to infuse 1 ml of solution into the lumen. The other end of the artery was clamped shut and the arteries were incubated at 37 °C for 20 minutes. After

incubation, the samples were washed with PBS to remove any residual elastase or saline. The arteries were then cut into segments of similar length (~15 mm) and flash frozen in liquid nitrogen. After storage overnight (-80 °C), the tissue segments were lyophilized to produce a dry sample. The dry weight of each segment was obtained. The dry arteries were placed in RIPA buffer (Thermo Scientific) containing 1% Halt^{TM} protease inhibitor (Thermo Scientific), homogenized and vortexed for one hour. The samples were centrifuged (10,000 rpm, 10 minutes) to pellet the cell debris and the supernatant removed and stored at -80^{o}C. The samples were thawed and prepared for western blot (**Table 3.2**) followed by heating for 10 minutes (70°C).

Table 3.2. Preparation of samples for western blot. The amounts listed are for one sample to be loaded into one well of the western blot gel.

Reagent	Volume (µl)
Sample in RIPA Buffer	15.6
Reducing Agent	2.4
Sample Buffer	6.0

A 22.5 µl aliquot of each sample was loaded under reduced conditions into each lane of a 4-12% sodium dodecyl sulfate polyacrylamide gel electrophoresis gel (SDS-PAGE), along with a SeeBlue pre-stained molecular weight ladder (Invitrogen). The gels were transferred onto nitrocellulose membranes (Invitrogen). Subsequently, the membranes were blocked for 1 hour with Odyssey Blocking Buffer (LI-COR Biosciences; Lincoln, NE; 1:1 dilution Blocking Buffer: PBS). After blocking, the membranes were labeled (16 hour, 4^{o}C) with a rabbit cathepsin K Ab (1:200 dilution) and a mouse monoclonal antibody against β-actin (1:1000; Sigma Aldrich). Following the primary antibody incubation, the membranes were washed with PBST (PBS+0.1% v/v Tween, 10 min, 10 min, 5 min). Secondary antibody labeling occurred at room temperature for 1 hour

on a shaker using IRDye® 680LT goat-anti-rabbit (1:15,000 dilution; LI-COR Biosciences) and IRDye® 800CW (1:20,000; LI-COR Biosciences). The membranes were protected from light to prevent photo-bleaching. The secondary antibody was removed by washing the membrane with PBST (10 min, 10 min, 5 min) and the membrane was then stored in PBST (4 °C). A LI-COR Odyssey scanning system was used to detect the protein bands. The intensities of the cathepsin K bands were quantified using Image Studio® and normalized to their respective β-actin bands to allow reliable comparison between different samples in the same blot.

3.8.3. NP targeting of cathepsin K in in vitro EaRASMC cultures

Using the covalent conjugation method, AF633-loaded PLGA NPs were conjugated with cathepsin K Ab. RASMCs and EaRASMCs (passage 3) were seeded at 75,000 cells per well and cultured for 13 days in six-well plates. The EaRASMCs were cultured in DMEM-F12 supplemented with 10% v/v FBS and 1% v/v PenStrep supplemented with 50 ng/ml of TNF-α. Following 24 hours of incubation, the cell cultures received the cathepsin K Ab-conjugated AF633-encapsulated NPs. The final concentration of NPs was 0.5 mg/ml. After a further 24 hours, the cell layers were fixed, stained with AF488-Phalloidin (green for cytoskeleton; Molecular Probes) and mounted on slides with VectaShield containing DAPI (blue for nuclei; Vector Labs, Burlingame, CA).

3.8.4 Assessing elastase-mediated disruption of the porcine carotid artery wall

Porcine carotid arteries were thawed, washed with PBS, and the length of each artery measured. One end of the artery was clamped shut and a catheter used to infuse 1 ml of solution (elastase; 20 units/ml; Sigma or 0.9% v/v sterile saline) before the other end

was clamped shut. With the arteries clamped, the artery segments were incubated for 20 minutes at 37°C. Following incubation, the arteries were washed with PBS to remove any remaining infusion solution before continuing with additional experiments.

3.8.4.1. Disruption of porcine carotid artery for TEM imaging

To determine the disruption of the artery due to elastase treatment, the arteries were prepared for imaging by TEM. Following either elastase or saline infusion (described in Section 3.8.4), the arteries were cut into small segments (~3 mm in length) and placed in room temperature 4% paraformaldehyde and incubated at 37°C for 5 minutes before fixation overnight at 4°C. The samples were post-fixed in 1% w/v osmium tetroxide (1 hour), dehydrated in a graded ethanol series (50-100% v/v), embedded in Epon 812 resin, sectioned, placed on copper grids, stained with uranyl acetate and lead citrate, and imaged (using FEI Tecnai G2 Spirit) under multiple magnifications.

3.8.4.2 Targeting cathepsin K modified NPs to the matrix-injured artery wall

To determine the effectiveness of cathepsin K targeting in the aorta, thawed porcine arteries (n = 3) were infused with elastase (20 units/ml, 37 °C, 20 minutes, Sigma) and rinsed with PBS. Following elastase infusion, unmodified Alexa Fluor 633-loaded NPs, cathepsin K Ab-conjugated Alexa Fluor 633-loaded NPs, IgG Ab-conjugated Alexa Fluor 633-loaded NPs, or 0.9% saline were infused in the artery (1 ml, 2 mg/ml NP) and incubated (37°C, 20 minutes). Following incubation, the arteries were flushed with PBS to remove any unbound NPs. The arteries were imaged (IVIS Spectrum CT *In Vivo* Imager, PerkinElmer; Waltham, MA) and analyzed using spectral unmixing to measure NP binding using Living Image® software. Briefly, spectral unmixing was used to subtract tissue

autofluorescence from each sample to allow for pure AF633 NP fluorescent signal. Once the tissue autofluorescence was removed, ROIs were drawn over each artery and the total radiant efficiency ([p/s]/ [μW/cm^2]) was measured and the fold-increase of NP fluorescence was calculated.

3.9. Characterizing DOX release from cathepsin K Ab-conjugated and unconjugated NPs

DOX release from both cathepsin K Ab-conjugated and unconjugated NPs was measured in PBS at 37^{o}C. The efficiency of DOX encapsulation within the NPs was determined by pooling the supernatants from the washing and ultracentrifugation steps for individual NP formulations. Unencapsulated DOX in the supernatant fraction was assayed by UV spectrophotometry (SpectraMax M2, Molecular Devices, Inc., Sunnyvale, CA) using the absorbance peak of DOX at 270 nm. This peak was calibrated to a standard curve generated using serial dilutions of a 1 mg/mL DOX solution. The total amount of encapsulated DOX and the encapsulation efficiency were determined by subtracting the total amount of unencapsulated DOX from the known amount of DOX added during NP formulation. Aliquots containing conjugated or unconjugated DOX-NPs (0.5 mg/ml) were collected at various time points over 45 days and centrifuged (13,000 rpm, 30 min, 4^{o}C). The amount of DOX in the supernatant was quantified by UV spectrophotometry. The absorbance at λ = 270 nm was calibrated to a standard curve generated using serial dilutions of DOX in PBS. Following the absorbance measurements, the volume in each sample was replenished with fresh PBS. The total amount of DOX loaded in the NPs was calculated and the released amount was used to determine the percentage of DOX released.

3.10. DNA assay for cell proliferation

The DNA content of the cell layers was measured via a fluorometric assay of Labarca and Paigen to determine the combined effects of the unconjugated or conjugated NPs and released DOX on EaRASMC proliferation[111]. The cell layers were harvested at 1 and 21 days of culture in Pi buffer, sonicated on ice, and assayed for DNA content. Cell density was calculated assuming 6 pg of DNA per cell.

3.11. Fastin assay for elastin

A Fastin assay (Accurate Scientific and Chemical, Westbury, NY) was used to quantify the amounts of elastic matrix (alkali-soluble and insoluble fractions) deposited by EaRASMCs. For each of 3 replicate samples, cell layers from 3 separate wells were harvested in Pi buffer, at 21 days of culture, and pooled. The cell layers were homogenized by sonication on ice. The cell suspension obtained was digested with 0.1 N NaOH (1 h, 98 ºC) and then centrifuged to yield a pellet containing mature, highly cross-linked alkali-insoluble elastin and a supernatant fraction containing less cross-linked alkali-soluble elastin. The alkali-insoluble elastin was converted into a soluble form prior to quantification, as the Fastin assay can only quantify soluble α-elastin. The pellet obtained after the NaOH digestion step was dried and solubilized with 0.25 M oxalic acid (1 h, 95 ºC), then pooled and centrifuge-filtered (3000 rpm, 10 min) in microcentrifuge tubes (Amicon® Ultra, 10 kDa molecular weight cut-off; Millipore, Inc., Billerica, MA). The alkali-soluble and insoluble matrix elastin fractions, as well as the tropoelastin precursors released into the cell culture medium were then measured using the Fastin assay. The

amounts of elastin measured were also normalized to the corresponding DNA amounts, so as to provide an accurate comparison between the different treatments.

3.12. Elastic matrix ultrastructure visualized by transmission electron microscopy (TEM)

To visualize the ultrastructure of deposited elastic matrix, EaRASMCs were seeded into permanox chamber slides (Thermo Fisher; Waltham MA; 50,000 cells per well) and stimulated with 50 ng/ml of TNF-α. After 21 days of culture, the test (cathepsin K Ab-conjugated DOX-loaded NPs, unconjugated DOX-loaded NPs) and control EaRASMC cultures were rinsed with PBS (37 °C) and fixed (5 min, 37 °C, 4% w/v paraformaldehyde/2.5% w/v glutaraldehyde prepared in 0.1 M sodium cacodylate buffer). Following the initial fixation step, the cell layers were incubated in the fixative overnight at 4 °C. The samples were post-fixed in 1% w/v osmium tetroxide (1 hour), dehydrated in a graded ethanol series (50-100% v/v), embedded in Epon 812 resin, sectioned, placed on copper grids, stained with uranyl acetate and lead citrate, and imaged (using FEI Tecnai G2 Spirit) under multiple magnifications.

3.13. Assessing MMP-2 and -9 expression in DOX-loaded NP treated EaRASMCs

MMP-2 and -9 expression by EaRASMCs cultured with cathepsin K Ab-conjugated or unconjugated DOX-NPs were compared using western blots. At 21 days of culture, the cell layers were harvested in RIPA buffer with protease inhibitor and 3 wells were pooled per replicate (n = 3 replicates/treatment). Maximum volumes of sample protein (15.6 µL) were then loaded under reduced conditions into each lane of a 10% Bis-Tris electrophoresis gel (Invitrogen), along with a SeeBlue^{TM} pre-stained molecular weight

ladder (Invitrogen) and MMP-2 and -9 standards. The gels were run in MOPS buffer (Invitrogen) for 50 minutes at 200 V, and subsequently dry transferred onto nitrocellulose membranes (iBlot® Western Blotting System, Invitrogen). As before, the membranes were blocked with Odyssey Blocking Buffer for 1 hour and immunolabeled (4 ^{o}C, overnight) with a rabbit polyclonal antibody against MMP-2 (1:500 dilution; Abcam, Cambridge, MA) or rabbit monoclonal antibody against MMP-9 (1:500 dilution; Millipore, Billerica, MA) with a mouse monoclonal antibody against β-actin (1:1000 dilution; Sigma-Aldrich) as a loading control. Secondary labeling occurred for 1 hour at room temperature using IRDye® 680LT goat-anti-rabbit (1:15,000 dilution; LI-COR Biosciences) and IRDye® 800CW goat-anti-mouse (1:20,0000 dilution; LI-COR Biosciences). A LI-COR Odyssey laser scanner was used to quantify the fluorescence of the secondary antibodies. The intensities of the active MMP-2 and MMP-9 bands on all gels were quantified using ImageJ software, expressed in terms of relative density units (RDU) and normalized to the intensity of their respective β-actin bands to enable comparison between the different test cases within the same blot. The ratios obtained for the NP-supplemented cell layers were further normalized to that for standalone EaRASMC cultures (treatment controls).

3.14. Assessing MMP-2 and -9 activity using gel zymography

The differential effects of cathepsin K Ab-conjugated and unconjugated DOX-loaded NPs on enzyme activity of MMP-2 and -9 in EaRASMC cultures was assessed using gel zymography. Cell layers harvested in RIPA with a protease inhibitor were loaded into each lane of a 10% zymogram gel (Invitrogen) in a volume containing 5 μg of protein, along with a SeeBlue™ pre-stained molecular weight ladder, and MMP-2 and -9 protein standards. Gels were run for 2 h at 125 V. The gels were then washed in a buffer containing

2.5% v/v Triton-X-100 for 30 min to remove sodium dodecyl sulfate (SDS) detergent, and then incubated overnight in a substrate/development buffer to activate the MMPs. The gels were stained with Coomassie Brilliant Blue solution for 45 min, and destained for 90 min, until clear bands appeared visible against the blue background of the gel. Band intensities (RDU) of the bands obtained for NP-supplemented cultures were measured using ImageJ software, and normalized to those obtained for the NP-untreated control cultures to determine fold changes in MMP activity. Data was acquired from 3 independent replicate gels.

3.15. Verification of cadherin and $\alpha v\beta_3$ expression and targeting by Ab-modified NPs

3.15.1. Cadherin and $\alpha v\beta_3$-Integrin expression by HUVECs in culture

In order to actively target the SMCs in the aorta, it is crucial for the NPs to pass through the endothelial cell layer. In AAAs, the endothelial cell layer is disrupted leading to gap formation and a leaky endothelium. Cadherin plays a vital role in cell-to-cell junctions so a decrease in cadherin expression can lead to the gap formation. Human umbilical vein ECs (HUVECs) were seeded at 30,000 cells per well and incubated at 37 °C until a confluent layer was formed. The cells were stimulated with 10 ng/ml TNF-α for 24 hours at 37°C. Following stimulation, cells were fixed with 4% paraformaldehyde (10 minutes, RT) and washed 3 times with PBS. The cell layer was blocked with the appropriate serum (5% serum, 20 minutes, RT). Following blocking, the primary antibody (1:100 dilution of cadherin Ab or $\alpha v\beta_3$ Ab) was added and incubated overnight at 4 °C. The primary antibody solution was aspirated and the cell layer washed with PBS. The secondary antibody (AF 488-conjugated secondary antibody, 1:1000 dilution) was added

and incubated for 1 hour at room temperature. The secondary antibody solution was aspirated and the cell layer washed with PBS twice. The cell layers were mounted onto glass coverslips using VectaShield® with DAPI to stain the nucleus. After mounting, the cell layers were visualized using a fluorescent microscope.

3.15.2. Preparation of AF633-loaded NPs

The AF633-loaded NPs were prepared using the methods previously described in Section 3.4. The PLGA NPs were prepared using a double emulsion solvent evaporation method with the AF633 encapsulated within the NP followed by washing to remove unencapsulated dye, flash freezing, and lyophilization to produce a dry powder. The particle size and surface zeta-potential were determined using a commercial particle-sizing system (PSS/NICOMP 380/ZLS, Particle Sizing Systems; Santa Barbara, CA) as described in Section 3.5.

3.15.3. Preparation of αvβ3-integrin Ab-modified NPs

The αvβ3-integrin plays a vital role in cellular adhesion and migration as well as cellular uptake. The goal of incorporating the αvβ3-integrin onto the NP surface was to increase the movement of the NPs through the endothelial cell (EC) layer into the tunica media. The covalent binding of the αvβ3-integrin Ab to the NP surface was performed using the procedure described previously in section 3.6.2 for cathepsin K Ab incorporation. The NPs were suspended in MES (0.5 mg/ml) and incubated with 10 µl of αvβ3-integrin Ab and 100 ng EDC for 5 hours. After incubation, the NPs were rinsed with PBS twice.

3.15.4. Assessment of αvβ3-integrin Ab incorporation on NP surface

Using the previously described procedure for measuring Ab binding to NPs (Section 3.7.3) we determined binding of the αvβ3-integrin Ab. An Alexa Fluor (AF) 488-conjugated goat anti-rabbit secondary Ab (1:1000 dilution; Thermo Fisher), was used to fluorescently tag the NP-bound αvβ3-integrin Ab (25 ^{o}C, 1 hour). Three 150 µl aliquots per sample were added to a microplate and the fluorescence of both the fluorescein (λ_{ex} = 493 nm and λ_{em} = 525 nm) and Alexa Fluor 633 (λ_{ex} = 632 nm and λ_{em} = 647 nm) were measured using a microplate reader. The NPs were aliquoted onto glass cover slips, mounted, and visualized on a fluorescent microscope.

3.15.5. NP localization in HUVEC cultures

HUVECs were seeded onto glass coverslips at a density of 30,000 cells per well and incubated for 7 days. The cells were unstimulated or stimulated with TNF-α (10 ng/ml) for 24 hours before the addition of AF633-loaded NPs or $\alpha v\beta_3$ Ab-modified AF633-loaded NPs. The test cases are shown in **Table 3.3**.

Table 3.3. Test cases for localization of NPs in HUVECs.

Stimulation	Nanoparticle
TNF-α	$\alpha v\beta_3$ Ab Modified
No TNF-α	$\alpha v\beta_3$ Ab Modified
TNF-α	Unmodified AF633 NPs

The cells were incubated with the NPs for 3 hours at 37 °C followed by washing with PBS to remove any unbound NPs. A membrane stain (Vybrant® DiI Cell-Labeling Solution, Thermo Fisher Scientific, 40 µM) was added to the cell layer and incubated for 15 minutes at 37 °C. The DiI solution was aspirated and the cell layer washed with PBS.

Following membrane staining, the cells were fixed with 4% v/v paraformaldehyde (10 minutes, RT) and mounted onto slides with mounting medium containing DAPI stain (VectaShield® mounting medium with DAPI). The cell layers were imaged using a confocal microscope (Leica TCS SP5 II-AOBS, Buffalo Grove, IL) allowing for the generation of Z-stacks enabling 3D reconstruction and multiple planes of views through the entire cell layer.

3.16. Migration of NPs through endothelial cell layer

3.16.1. FITC-Dextran migration through endothelial cell layer

HUVECs were seeded on a transparent 1.0 µm polyethylene terephthalate (PET) membrane cell insert that had been previously coated with collagen. Rat Tail Collagen Type I (1 mg/ml) was added to the membrane and incubated for 1 hour at 4 °C. The collagen solution was removed and the membranes incubated overnight at 4 °C. After incubation, HUVECs were seeded (30,000 cells per insert) on each membrane and allowed to incubate at 37 °C for 7 days. The test case was HUVECs stimulated with TNF-α (10 ng/ml) for 24 hours and the two control cases were HUVECs without stimulation and the membrane containing no HUVECs. FITC-Dextran (1 mg/ml, 150,000 avg. MW) was added to the upper chamber of each insert and incubated at 37 °C for 3 hours. Following incubation, the supernatant from the lower chamber was removed and three 150 µl aliquots from each sample were added to a 96-well microplate and the fluorescence measured using a fluorescent plate reader (λ_{ex} = 490 nm and λ_{em} = 525 nm).

3.16.2. NP migration through the endothelial cell layer

AF633 loaded-NPs were modified with an $\alpha_v\beta_3$-integrin Ab as previously described (Section 3.15.3). HUVECs were seeded on a 1.0 µm PET membrane cell insert previously coated with collagen using the procedure from Section 3.16.1. The test cases were stimulated with TNF-α (10 ng/ml) for 24 hours. Following stimulation, the αvβ3-integrin Ab-modified NPs or unmodified NPs (0.2 mg/ml) were added to the upper chamber of the insert (**Table 3.4**). The cells were incubated for 3 hours at 37 °C. Following incubation, the media from the lower chamber was removed and the fluorescence of the NPs was measured using a fluorescent plate reader (λ_{ex} = 632 nm and λ_{em} = 647).

Table 3.4 Test cases for NP migration through the endothelial cell layer.

Cells	Stimulation	NP Addition
Yes	TNF-α (10 ng/ml)	$\alpha_v\beta_3$-integrin Ab-modified AF633 NPs
Yes	TNF-α (10 ng/ml)	Unmodified AF633 NPs
Yes	No TNF-α	Unmodified AF633 NPs
No	No TNF-α	Unmodified AF633 NPs

3.17. Oxidative stress assay for DOX-loaded NPs in HUVECs and EaRASMCs

In order to determine the toxicity of DOX-loaded NPs, the oxidative stress and superoxide production was measured when DOX-loaded NPs were cultured with EaRASMCs and HUVECs. The oxidative stress was determined using an ROS/Superoxide Detection Assay Kit (Abcam). Cells were seeded in a 96 well plate at a density of 20,000 cells per well and incubated at 37°C until the cells were at ~70-80% confluency (approximately 48 hours). The media was aspirated and fresh media added the day of the experiment. The cells were simultaneously treated with DOX-loaded NPs (0.2 mg/ml) and 100 µl of ROS/Superoxide Detection Solution (1:2500 dilution of Oxidative Stress

Detection Reagent, 1:2500 dilution of Superoxide Detection Reagent). The cells were incubated for 60 minutes at 37°C. Following incubation, the plate was read from the bottom using a fluorescent plate reader for fluorescein (λ_{ex} = 488 nm and λ_{em} = 520 nm) and rhodamine (λ_{ex} = 550 nm and λ_{em} = 610 nm).

3.18. AAA induction in rat model via periadventitial elastase injury

3.18.1. Surgical procedure for AAA induction

Previously, as described in Section 3.1, aneurysm induction in our lab was performed using an elastase infusion into the aorta which requires complex microsurgical intervention for collateral vessel ligation, aortal catheterization and aortotomy sealing, the latter at risk of reopening and hemorrhage. As a result, we investigated if small aneurysms could be generated in the rat model instead through periadventitial elastase treatment. This method also provides the advantages of limiting lower limb paralysis that results from extended durations of surgery.

All rat surgeries were performed with IACUC approval at the Cleveland Clinic (2016-1581). Acepromazine (0.5 mg/kg) was administered subcutaneously approximately 30 minutes before the induction of anesthesia. Fresh elastase solution was prepared (20 Units or 40 Units elastase, Sigma) and stored on ice until use. Immediately before anesthesia induction, buprenorphine hydrochloride (0.03 mg/kg) was administered subcutaneously. Following injection, the rat was moved to the anesthesia induction chamber (oxygen flow rate 1 L/min, 2.5% v/v isoflurane) for 7-8 minutes until anesthetized.

Once anesthetized, the rat was removed from the chamber and ophthalmic eye ointment was applied to both eyes. The rat was placed on the surgery table and its nose inserted into the nose cone. The isoflurane concentration was reduced to 2% for the duration of the procedure. The hair from the abdomen was clipped, the abdominal skin sterilized using betadine and alcohol scrubs with application proceeding from the inside out. Immediately before the surgical procedure, 0.25% Bupivacaine (2-8 mg/kg; analgesic) was administered subcutaneously at the incision site. The abdominal cavity was exposed by a laparotomy and the abdominal wall was held open using retractors. The exposed intestines and other internal organs (stomach, pancreas, liver, etc.) were removed to outside the body cavity and were covered with moistened sterile gauze to prevent drying during the procedure. Using fine forceps, the aorta was exposed by removing surrounding fat and connective tissue. Once the aorta was exposed, images were taken using a microscope to allow for diameter determination. The elastase or 0.9% v/v saline was soaked up by a small piece of gauze and the soaked gauze was placed around the aorta. This was done to ensure the treatment stayed in contact with the aorta for 20 minutes. The gauze was removed and the residual solution (elastase or saline) removed by rinsing the cavity with sterile saline and soaked up with sterile gauze. Images of the aorta were taken post treatment. The intestines were replaced and the abdomen sutured. The muscle layer was sutured using 4-0 vicryl non-absorbable nylon stiches in a running pattern. The skin was sutured using 4-0 silk stiches in an interrupted pattern. During suturing, the isoflurane was reduced to 1.5% v/v to begin recovery.

The animal was removed from isoflurane and placed on a heating pad (37 °C) to continue recovery. The animal was moved to its cage and placed on a towel to finish

recovering. While in the cage, food and a water-gel pack was placed on the cage floor to allow access during recovery. Once the animal has recovered enough to move around the cage, the cage was returned to the BRU. Pain from the surgery is managed through twice daily injections of buprenorphine hydrochloride (0.03 mg/kg) for 72 hours.

3.18.2. Rat AAA diameter measurements using stereomicroscope

The images taken prior to elastase treatment were used for diameter measurements of the aorta. All images of the aorta during surgery were generated using an Olympus SZ61 microscope. The images include a reference marker with a known diameter (1.5 mm) to accurately measure the aorta diameter. To perform the measurements (ImageJ®), a straight line was drawn across the reference marker to determine the number of pixels per 1.5 mm and this was used to create a global scale. Straight lines were drawn across six different segments of the exposed aorta and the length of each line was calculated. The average length and standard deviation of the lines were calculated for each rat. The same procedure was used to determine the final diameter of the aorta following a 14 day development period. The initial and final measurements were compared to determine the increase in diameter due to the elastase treatment.

3.18.3. Rat AAA model for aorta imaging using MRI

An initial trial for protocol development was set up to optimize the MRI parameters to clearly visualize the aorta. This protocol development was performed on a naïve male rat under anesthesia. The breathing rate of the rat was monitored and the concentration of isoflurane administered was altered to maintain 50 breaths per minute. The breathing rate was maintained at this level due to the MRI software containing a specific gated imaging

program that generates clearer images. This MRI program takes images between breaths to minimize the distortion effects of the movement of the chest cavity.

The anesthetized rat was placed in the MRI in a prone position for imaging. Multiple images of the abdomen were taken to identify which parameters and program settings generated clear visualizations of the aorta. The images were taken under several imaging modes including T1-Flash, T1-FISP-3D, and T2-TurboRARE. The images were taken with either a coronal or axial orientation.

To further develop the imaging protocol, a euthanized rat, which had undergone aneurysm induction as previously described (Section 3.18.1), was imaged to determine aorta diameter. For this protocol development, the rat was placed in the MRI instrument in a supine position. The change in position (prone to supine) was taken into account to determine which position enhances the images. Images were taken using T1-Flash and T2-TurboRARE.

All images from the MRI were converted from a DICOM format to a NiFTi format for use in imaging software. The images were viewed using the software programs mricron and MIPAV to visualize the aorta, determine aorta diameter, and generate a 3D reconstruction. In MIPAV, the aorta was measured using the line tool to draw a line across the aorta and the width measured from the line length. The aorta was measured in two directions – from the coronal plane and the sagittal plane to determine any expansion from periadventitial elastase treatment.

3.18.4. Cathepsin K expression in induced rat AAAs

Following aneurysm induction, the aneurysm was left to develop over 14 days before sacrificing the rat by CO_2 and a physical secondary method. The abdomen of the euthanized rat was opened using sterile procedures through the previously described laparotomy and the aorta exposed. Healthy segments and elastase injured segments of the aorta were removed and rinsed with PBS. Removing healthy and injured segments from the same aorta provides an internal control for cathepsin K expression. The segments were flash frozen in liquid nitrogen and stored at -80°C before lyophilization. The dried segments were placed in RIPA buffer, homogenized and placed on a shaker at 4 °C for 1 hour. The vials were centrifuged (12,000 rpm, 10 min) to pellet any debris and the supernatant collected. The supernatant was stored at -80°C until western blot was performed. The western blot for cathepsin K expression was performed following the procedure previously described (Section 3.8.2).

3.18.5. Preliminary imaging studies to assess uptake of intravenously infused NPs into AAA wall

Following aneurysm induction and development, the rat was anesthetized using isoflurane (2.5%). The abdomen and back of the rat were shaved to decrease auto fluorescence before imaging. The rat was placed in a prone position in the IVIS Spectrum CT connected to isoflurane to maintain anesthesia during imaging. Images of the anesthetized rat were taken under varying wavelengths as a control and to allow for spectral unmixing. The multiple wavelengths were selected to cover the excitation and emission wavelengths of the AF633 loaded into the NPs as well as allow for the subtraction of tissue autofluorescence. Following the collection of control images, the anesthetized rat was

injected with cathepsin K Ab-modified AF633 NPs (5 mg/ml) via tail vein injection. Images were taken at 30 minutes, 3 hours, and 24 hours post-injection to determine the localization of the NPs.

Following aneurysm induction and development, the rat was anesthetized (2.5% isoflurane) and injected with cathepsin K Ab-modified VivoTag® 800-loaded NPs (10 mg/ml) via tail vein injection. The rat was euthanized after injection (1 or 3 hours) and the abdomen opened via laparotomy to expose the aorta. The exposed aorta was imaged using the IVIS Spectrum CT to determine the localization of the NPs. As previously discussed, the images were taken under multiple wavelengths to visualize the fluorescently loaded NPs as well as identify background and tissue autofluorescence. The images were visualized using Living Image® software and spectral unmixing was performed to identify pure Vivotag800® fluorescence.

3.19. Statistical analysis

All experimental data presented (n = 3 per condition, unless stated otherwise) are mean values with standard deviation (SD) or standard error (SE) where indicated. Statistical significance of differences between mean values for different samples and conditions was evaluated using a Student's t-test, with $p \leq 0.05$ considered as statistically significant.

CHAPTER IV

RESULTS AND DISCUSSION

4.1. Introduction

The following sections present the results from experiments conducted to demonstrate the feasibility of using cathepsin K as a molecular target for AAA wall-specific delivery of drug-releasing elastic matrix regenerative NPs. The experiments assess the formulation of Ab-modified NPs, expression of cathepsin K *in vitro* and *ex vivo*, and the ability of cathepsin K Ab-conjugated NPs to target cathepsin K. The ability of Ab-conjugated NPs to migrate through the endothelial cell layer is discussed as well as the stress induced from the presence of iron oxide NPs. Finally, aneurysm induction in a rat model, experiments to identify and image aneurysm formation, and the ability of Ab-conjugated NPs to target the aneurysm is discussed.

4.2. Formulation and characterization of PLGA nanoparticles

The physical characteristics, size and zeta potential, of the 0.25% w/v DMAB stabilized PLGA NPs were determined for the various encapsulations. The formulation of the blank PLGA NPs stabilized with DMAB exhibited a size of 306.9±115.1 nm and a zeta

potential of 30.89 mV. Changing the loading of the NPs with either 2% DOX or various fluorescent dyes did not affect the size or zeta potential (**Table 4.1**). For the NPs in this study, the target size was ~300 nm and the target zeta potential was ~30 mV.

Table 4.1. Mean size and zeta potential of DMAB stabilized PLGA NPs with various encapsulations.

NP Condition	Size (nm)	ζ-potential (mV)
No encapsulation	306.9±115.1	30.89
2% w/w fluorescein	280.9±96.4	30.29
2% w/w DOX	299.3±124.8	32.04
2% w/w Alexa Fluor 633	287.8±90.4	40.52
2% w/w VivoTag® 800	343.1±147.9	29.00

4.3. Cathepsin K Ab-modified NPs

4.3.1. Assessment of cathepsin K Ab conjugation to NPs

The conjugation of the cathepsin K Ab to the surface of the NPs was confirmed using fluorescence microscopy (**Figure 4.1**). Utilizing the adsorption and covalent conjugation methods, the cathepsin K was successfully incorporated on the NP surface (**Figure 4.1.B** and **Figure 4.1.C**). Incubation of the NPs with the cathepsin K Ab for 5 hours was appropriate as longer incubation times (up to 24 hours) did not result in improved Ab conjugation (**Figure 4.1.A**)[112].

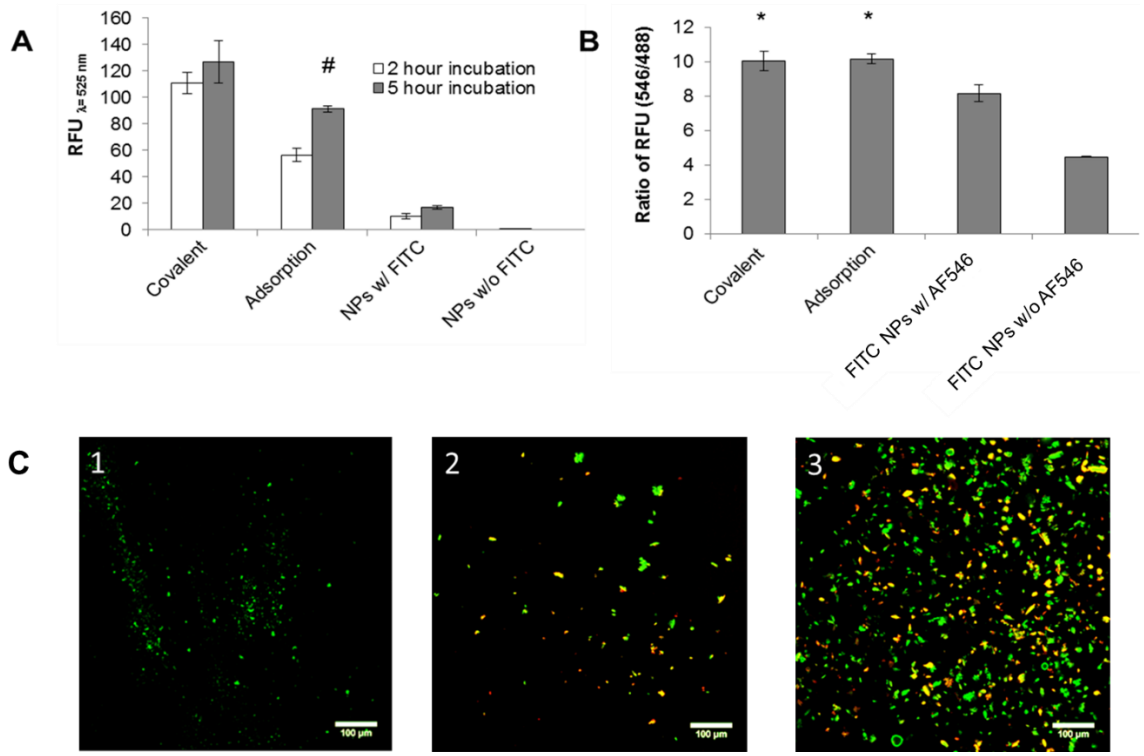

Figure 4.1. The effect of incubation times on conjugation of the antibody to NPs (A). The cathepsin K antibody was detected with a fluorescein-tagged secondary Ab. Relative abundance of conjugated antibodies on the NP surface (B). Cathepsin K antibodies were conjugated onto fluorescein-loaded NPs over 5 hours and were detected with secondary antibodies tagged with AF546. Values shown indicate mean ± SD of RFUs (A) or of ratios of RFUs due to the fluorescein and AF546; n = 3 per case; # denotes significance of differences versus 2 h of incubation, deemed for $p < 0.05$; * denotes significance of differences versus control FITC NPs treated with the AF-546-tagged secondary antibody, deemed for $p< 0.05$. In C, micrographs compare cathepsin K antibody bound to NPs via adsorption and covalent conjugation methods (see quantitative data B). Conjugation was performed over 5 hours. Fluorescein (green) was encapsulated within the NPs and the cathepsin K antibody was detected with an AF546-tagged secondary antibody (red). Panel C1 shows lack of red auto-fluorescence from cathepsin K antibody-conjugated NPs not treated with the AF546-tagged secondary antibody. Panels C2 and C3 show that cathepsin K antibody was successfully conjugated to the NP surface using the adsorption and covalent binding methods respectively[112].

In **Figure 4.1.C**, unconjugated NPs (A) fluoresce green and the cathepsin K Ab-conjugated NPs with the AF546 fluorescent secondary antibody (B) fluoresce yellow. The AF546 secondary antibody fluoresces red alone but when the red and the green signals overlap,

the fluorescent signal turns yellow. The overlapping of these signals and the yellow fluorescence present in the images confirms the conjugation of the cathepsin K Ab to the NP surface.

4.3.2. Assessment of cathepsin K Ab modification for covalent and adsorption methods

To determine whether the covalent conjugation method or the adsorption method provided a stronger cathepsin K Ab attachment to the NP surface, fluorescence microscopy was used (**Figure 4.2**). The adsorption method for Ab attachment to the NP surface utilizes van der Waals forces, generally a weak force, while the covalent conjugation involves a carbodiimide reaction to generate covalent bonds between the Ab and surface. Images were taken under similar conditions at day 1 and day 14. The intensity of the AF633-loaded NPs (red) were measured as well as the intensity of the FITC-labeled cathepsin K antibody (green). The fluorescence of the NPs in **Figure 4.2.A** show a noticeable change in FITC fluorescence at day 14 for the adsorption method. To quantify the changes in fluorescence intensity, the corrected total fluorescence was calculated and a ratio of FITC to AF633 was determined. **Figure 4.2.B** shows the conjugation method provides a significantly ($p < 0.05$) more robust attachment of the cathepsin K Ab to the NP surface. After 14 days, there was a significant decrease in cathepsin K Ab presence on the NP surface for the adsorption method. However, there was no significant loss of cathepsin K Ab from the NP surface at 14 days, when covalently conjugated. This confirms the covalent conjugation method, which generates stronger covalent bonds compared to the weaker van Der Waals interactions, is superior to the adsorption method and therefore will be used in following experiments.

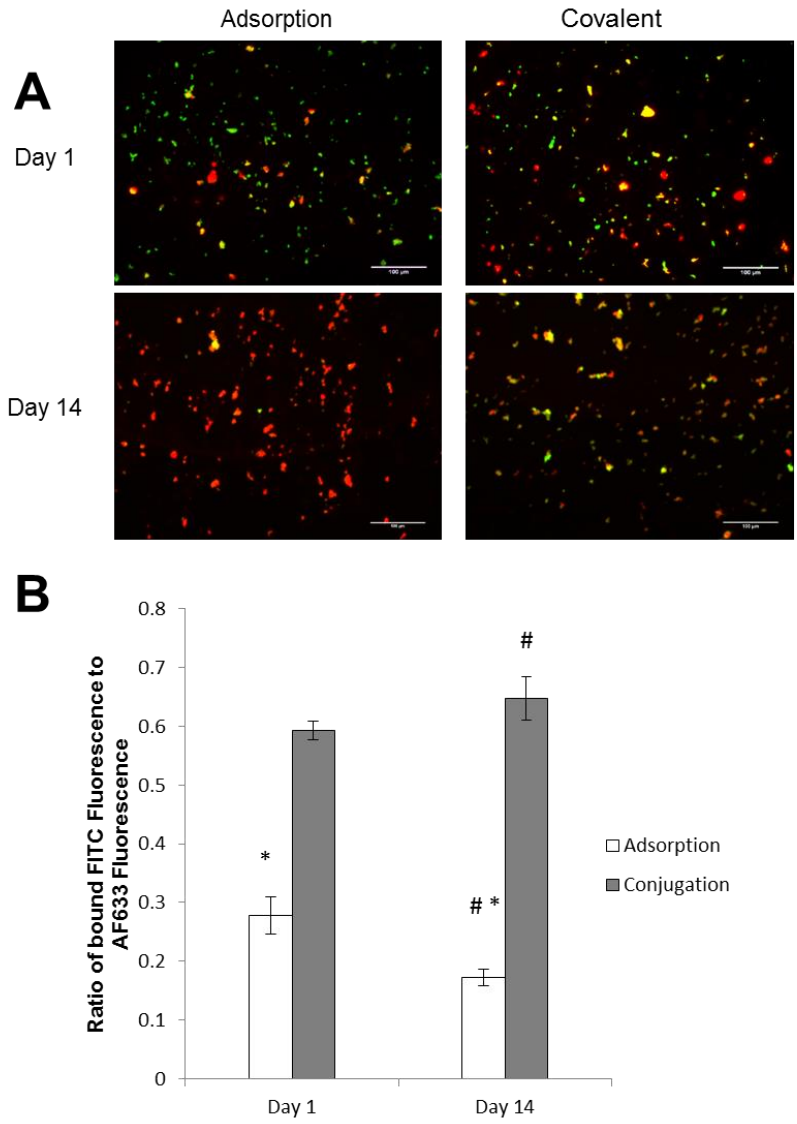

Figure 4.2. Panels A and B show results of fluorescence microscopy analysis of cathepsin K surface modification to AF633-loaded NPs (red). A fluorescein antibody (green) was added to visualize the cathepsin K modification. Panel A shows representative images for the adsorption and covalent conjugation methods at day 1 and day 14. The green fluorescence demonstrates successful cathepsin K conjugation to the NP surface. At day 14, green fluorescence associated with NPs modified using Ab-adsorption was much lower compared to NPs covalently conjugated with the Abs. Panel B shows the ratio of FITC intensity to AF633 intensity (mean ± SE; adsorption n=132, n=130 and conjugation n=154, n=207). The conjugation method bound more cathepsin K to the NP surface for a longer period of time. # denotes significance of differences between adsorption and conjugation on day 14 deemed for $p<0.05$. * denotes significance of differences between day 1 and day 14 for the adsorption method deemed for $p<0.05$[112].

4.4. Verification of cathepsin K overexpression

4.4.1. Verification of cathepsin K expression in EaRASMCs

Increased expression of cathepsin K by EaRASMCs and the effects of TNF-α in augmenting the expression were investigated as this simulates the AAA environment. Comparing cathepsin K expression levels between healthy SMCs (RASMCs) and EaRASMCs, the stimulation of EaRASMCs with TNF-α increased the expression of cathepsin K significantly (**Figure 4.3.A** and **Figure 4.4**). **Figure 4.4** highlights the increased cathepsin K expression using western blot and the images in **Figure 4.3.A** show an increase in cathepsin K expression within the cell layer but it does not provide enough information to determine the location of the cathepsin K. In order for the cathepsin K Ab-conjugated NPs to target cathepsin K, it needs to be released from the cells and localized on the cell surface. To determine the localization of cathepsin K, IF labeling for cathepsin K was visualized using a confocal microscope and reconstructed in 3D (**Figure 4.3.B-C**). **Figure 4.3.B** shows the 3D reconstruction of the cell layer with the nuclei (blue), actin filaments (green) and the cathepsin K (red). The image in **Figure 4.3.B** is a representative image of the cell layer and shows the aggregation of cathepsin K on the cell surface. However, for further confirmation of cathepsin K localization, the cell layer was imaged at various planes heights (**Figure 4.3.C.1** through **4**). **Figure 4.3.C.1** shows the bottom of the cell layer which was attached to the glass coverslip. This region shows very little cathepsin K present. As the imaging planes move towards the top of the cell layer (**Figure 4.3.C.2** through **3**), cathepsin K begins to appear. This confirms the presence of cathepsin K on the cell surface and therefore it can be utilized as a target molecule for the cathepsin

K Ab-conjugated NPs. **Figure 4.3.C.4** is a graphical representation of the plane heights shown in **C.1** through **C.3**.

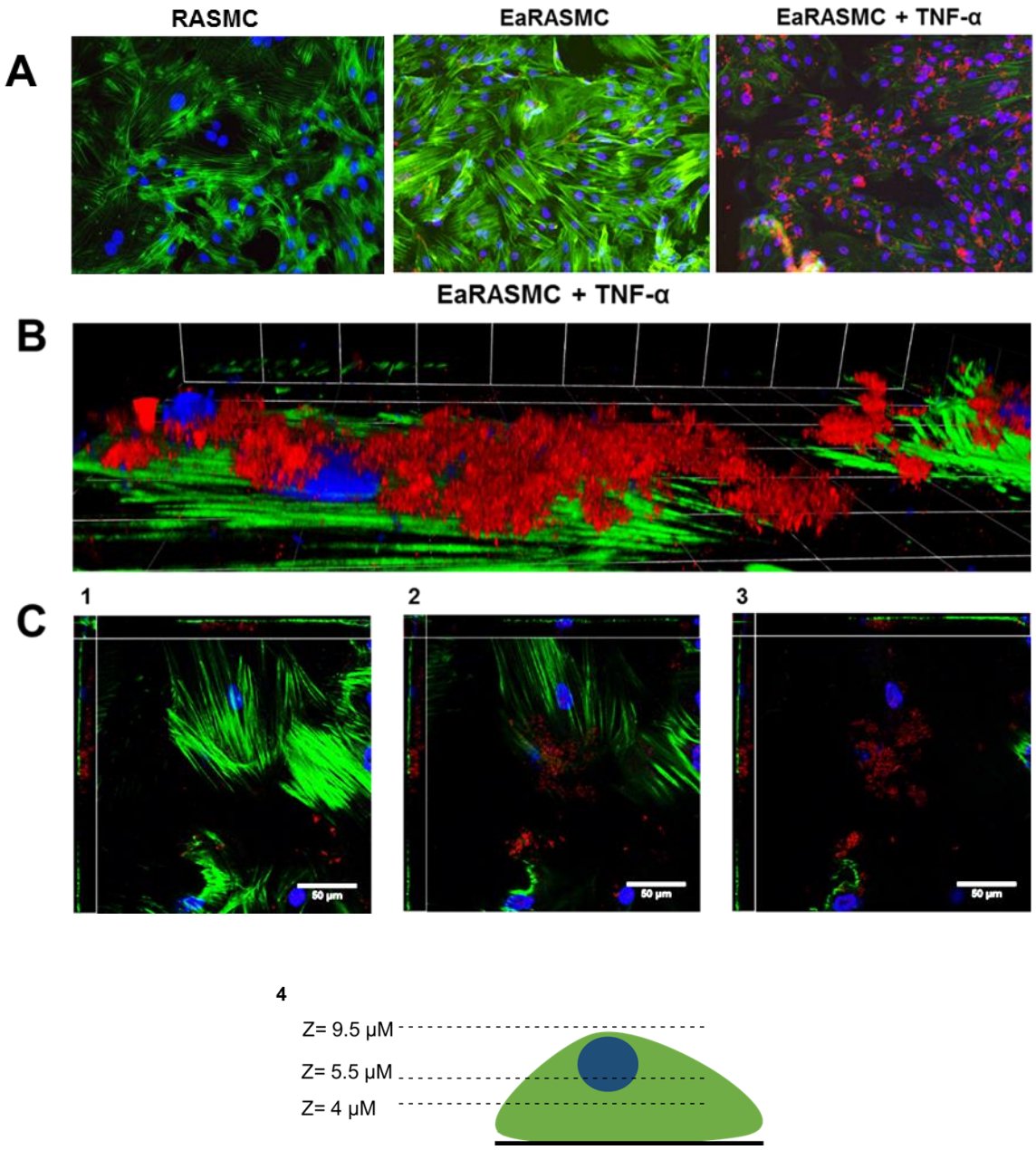

Figure 4.3. (A) IF images (20x) showing relative expression of cathepsin K in RASMCs and EaRASMCs, without and with TNF-α stimulation. Cathepsin K (AF546-tagged secondary antibody) appears red while the cytoskeletal actin filaments (AF488 phalloidin) appear green, and DAPI-stained nuclei appear blue. (B) High magnification view of EaRASMCs stimulated with TNF-α and cathepsin K visualized with AF546-tagged secondary antibody and cytoskeletal actin stained with AF488 phalloidin. Grid: 23 µm x

23 µm. (C). Images of the EaRASMCs at different z-axis heights. (1) The bottom of the cell layer which shows minimal cathepsin K. (2) The middle of the cell layer in which cathepsin K begins to appear. (3) The top of the cells where the most cathepsin K is found. Scale bar for C.1-3: 50 µm. (4) Schematic of the z-axis heights for images C.1-3[112].

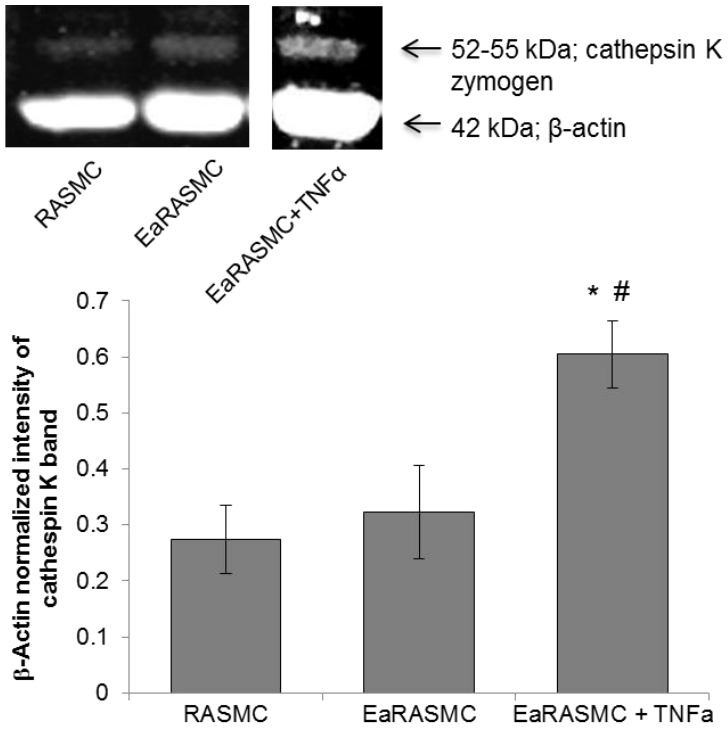

Figure 4.4. Western blot analysis for relative expression of cathepsin K by healthy and aneurysmal SMCs, with and without TNF-α stimulation. The figure shows a representative blot, indicating bands for the cathepsin K zymogen and β-actin (loading control). The plot shows β-actin normalized cathepsin K band intensity (mean ± SD; n = 3 per case); * denotes $p < 0.05$ compared to TNF-α-unstimulated EaRASMCs. # indicates significance of differences versus RASMCs, deemed for $p < 0.05$[112].

4.4.2. Verification of cathepsin K expression in elastase injured arteries

Differences in cathepsin K expression in healthy and matrix-injured porcine carotid arteries was investigated to rationalize using cathepsin K as an NP target in the AAA wall, wherein such elastase induced matrix disruption occurs. Elastase has the ability to digest elastin fibers causing injury similar to an abdominal aortic aneurysm. Western blot

analysis (**Figure 4.5**) showed significant increase in active cathepsin K (38 kDa) expression after exposure to elastase compared to the saline control (7.85 ± 1.93 vs. 0.14 ± 0.02, $p < 0.05$). These findings are similar to our previous results showing an increased cathepsin K expression in TNF-α activated EaRASMCs cultures. The increase in cathepsin K provides a rationale for the study of elastase injured arteries in the context of investigating targeted binding of cathepsin K Ab-conjugated NPs.

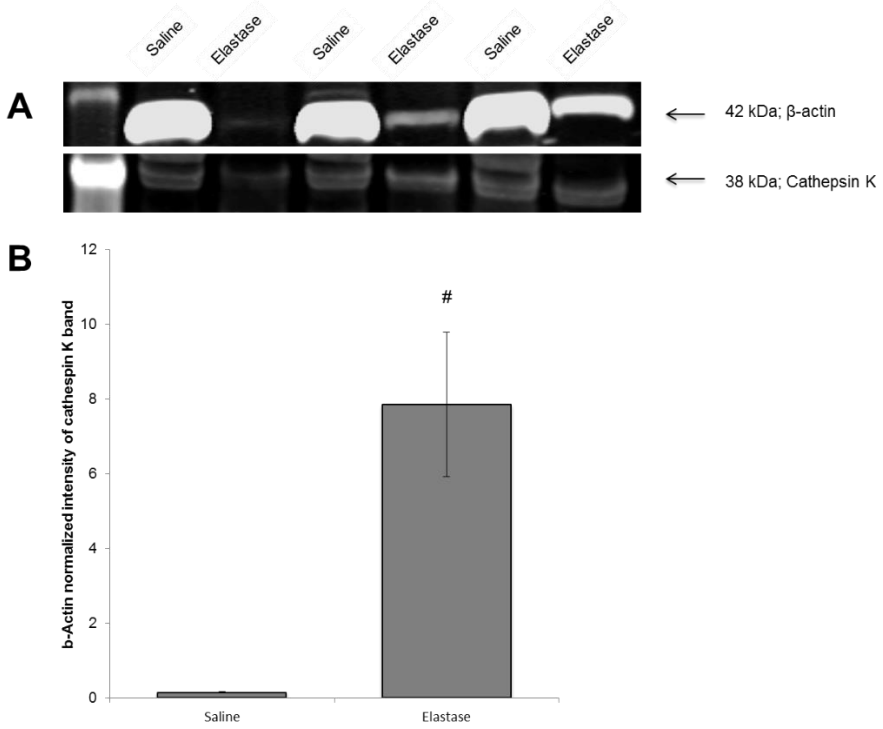

Figure 4.5. Verification of the expression of cathepsin K Ab in elastase injured carotid arteries compared to saline treated arteries, assayed using western blots. Panel A shows a representative blot, showing the active cathepsin K form (38 kDa) and β-actin (loading control). Panel B shows β-actin normalized cathepsin K band intensity (mean ± SEM; n = 9 per case; # denotes significance of difference, deemed for $p < 0.05$[112].

4.5. Targeting of Ab-conjugated NPs to cathepsin K expressing cells

4.5.1. Targeting of cathepsin K Ab-conjugated NPs in EaRASMCs

Figure 4.6 shows microscope and confocal images of RASMCs and EaRASMCs, cultured without TNF-α or with TNF-α, exposed to cathepsin K Ab-conjugated NPs (red fluorescence). EaRASMCs stimulated with TNF-α exhibited a high amount of bound, cathepsin K-Ab conjugated NPs relative to the RASMCs and the EaRASMCs without TNF-α activation. This indicates that the conjugated NPs have a much higher targeting ability correlated to the overexpression of cathepsin K in the stimulated cultures. The unstimulated EaRASMCs showed an increase in bound NP compared to the RASMCs but less than the stimulated EaRASMCs. The EaRASMCs exhibit basal levels of cathepsin K expression and the amount of bound NPs is directly related to the amount of cathepsin K expressed.

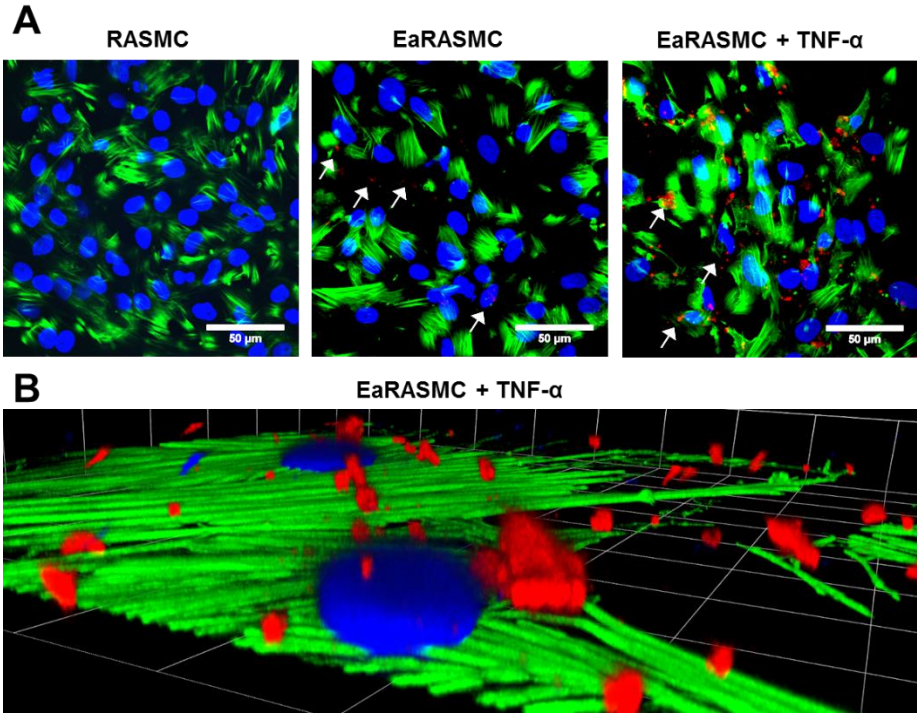

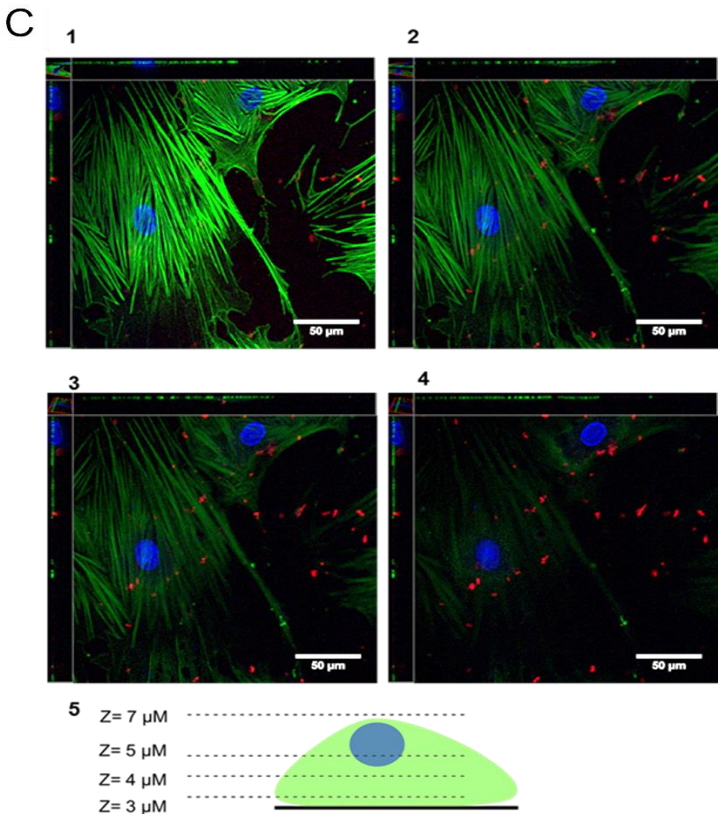

Figure 4.6. Localization of cathepsin K Ab-conjugated NPs on RASMCs and EaRASMCs stimulated with TNF-α. (A) Microscope images showing binding of cathepsin K antibody-conjugated NPs to EaRASMCs, without and with TNF-α stimulation. All NPs were encapsulated with AF633, causing them to fluoresce red. A higher number of NPs bound to EaRASMC cultures stimulated with TNF-α compared to unstimulated EaRASMCs. Cytoskeletal actin filaments, stained with AF488 phalloidin fluoresce green and DAPI-stained nuclei appear blue. (B). High magnification image of NP localization to TNF-α stimulated EaRASMCs. (C) Images of EaRASMCs with NPs at various z-axis heights. (1) Bottom of cell layer with minimal NP bound. (2) and (3) Middle layers of the cell where NPs begin to appear around the cell. (4) Top of the cell layer where NPs are bound to the cell surface. (5) Schematic of the various z-axis heights for images 1-4. Scale bars represent 50 µm (A), 23 µm x 23 µm (B), and 50 µm (C)[112].

4.5.2. Targeting of cathepsin K Ab-conjugated NPs in elastase injured arteries

Figure 4.7 shows fluorescence images of, and a plot highlighting the fold-differences in binding of unconjugated NPs and Ab-conjugated NPs to the cathepsin K expressing wall of porcine arteries. Previous results have shown an increase in cathepsin K expression following elastase injury in porcine carotid arteries. Utilizing this

overexpression, the conjugation of the cathepsin K Ab to the NP surface will increase the retention of the NPs within the vessel. To compare the binding to cathepsin K specifically, the NPs were unconjugated and conjugated with a nonspecific IgG Ab. The nonspecific IgG Ab should not increase the retention of the NPs in the vessel as there is no binding sites for the Ab. In **Figure 4.7.A.4**, there is no fluorescence from the saline treated artery and this was used as a negative control to ensure there was no autofluorescence. The fluorescent images in **Figure 4.7.A** show the greatest intensity in the cathepsin K Ab-conjugated NPs while the unconjugated and IgG Ab-conjugated NPs show similar fluorescent intensities. Using Living Image® software to perform spectral unmixing and the total radiant efficiency, the intensity of the AF633-loaded NPs was determined for each artery using the same sized region of interest. The total radiant efficiency ratio was determined using the unconjugated total radiant efficiency and the results are shown in **Figure 4.7.B**. The plot of the total radiant efficiency confirms the increase in cathepsin K Ab-conjugated NP retention in the artery compared to the unconjugated and IgG Ab-conjugated NP in which these results are similar to the observations in cell cultures. The intensity of fluorescence due to uptake of cathepsin K Ab-conjugated NPs in the artery wall was ~2-fold higher relative to that observed for Ab-unconjugated NPs.

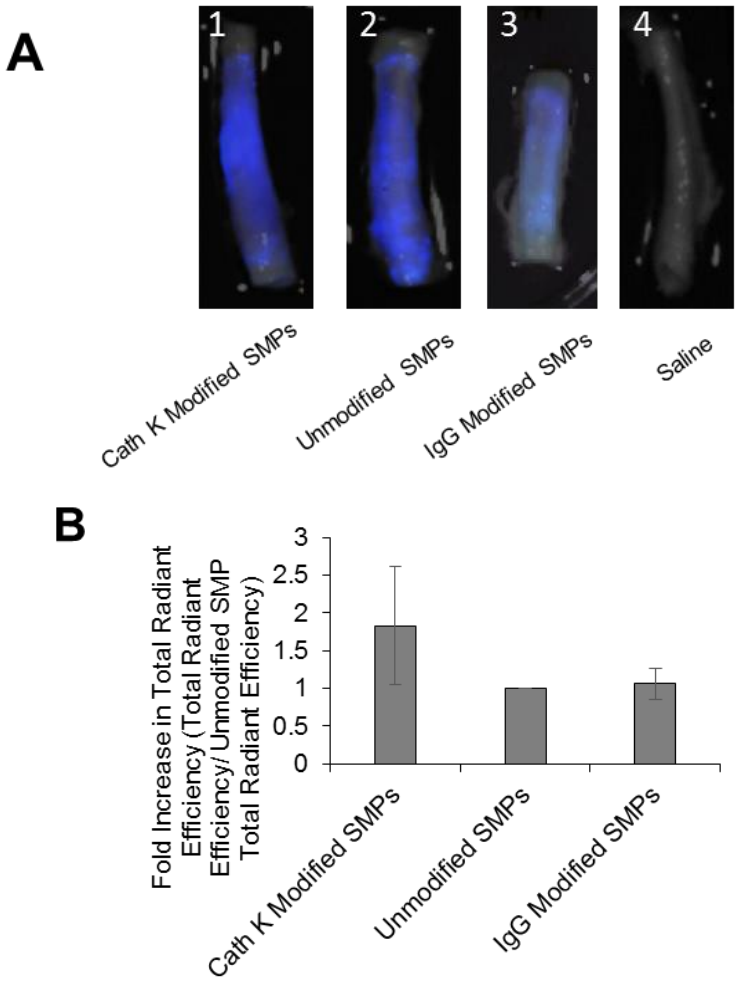

Figure 4.7. Targeting of cathepsin K Ab-conjugated AF633-loaded NPs to wall of elastase injured porcine carotid arteries. (A) Pseudocolor of NP localization in elastase treated arteries with (1) cathepsin K-Ab conjugated AF633 NPs, (2) unconjugated AF633 NPs, (3) IgG-Ab conjugated AF633 NPs, and (4) saline. (B) Fold difference in binding of cathepsin K Ab-conjugated NPs and non-specific IgG conjugated NPs to elastase treated arteries compared to binding of unconjugated NPs (mean ± SEM; n = 6 and n = 3 for IgG-Ab conjugation)[112].

4.6. Effect of conjugated, DOX-loaded NPs on elastic matrix synthesis

Prior data from our lab indicate DOX concentrations below 5 μg/ml stimulate elastic matrix regeneration while maintaining the inhibitory effects on MMPs[23]. Using a 2% w/w DOX encapsulation in PLGA NPs, the released DOX over a 21-day period is less

than 5 μg/ml and the elastic matrix deposition significantly increased in cultures treated DOX-loaded NPs compared to untreated cultures[23,112]. Our own studies showed that cathepsin K Ab conjugation to the NPs does not alter the DOX release profile and generated near steady-state doses in the desired dose range (**Figure 4.8**). The deposition of the elastic matrix was quantified using a Fastin assay (**Figure 4.9.B**) and culturing EaRASMCs with DOX-loaded NPs leads to a significant increase in elastin production per cell compared to untreated cells. The TEM results presented in **Figure 4.9.C** demonstrate that cathepsin K Ab-conjugated and unconjugated DOX-loaded NPs increase generation of elastic matrix compared to NP-untreated EaRASMC cultures. While only sparse elastin fibrils and microfibrils were seen in the control cultures (**Figure 4.9.C.1**), significantly greater presence of forming elastic fibers associated with amorphous elastin deposits were seen in the DOX-loaded NP-treated cultures. No significant differences in elastic matrix deposition were noted between the cultures receiving Ab-conjugated and unconjugated NPs. This is further supported by the data examining the release profile of conjugated and unconjugated NPs in which there was no difference in release kinetics[112]. MMPs play a significant role in the degradation and remodeling of the ECM especially in AAAs, so MMP expression and activity was assessed using western blot and gel zymography, respectively (**Figure 4.10**). The expression of MMP-2 was significantly decreased in EaRASMCs cultured with the cathepsin K Ab-conjugated and unconjugated DOX-loaded NPs compared to NP-untreated cultures (**Figure 4.10.A** and **Figure 4.10.B**). Similarly, the activity of MMP-2 and MMP-9 was significantly decreased in TNF-α stimulated EaRASMCs when cultured with the cathepsin K Ab-conjugated and unconjugated DOX-loaded NPs compared to NP-untreated cells (**Figure 4.10.C-F**).

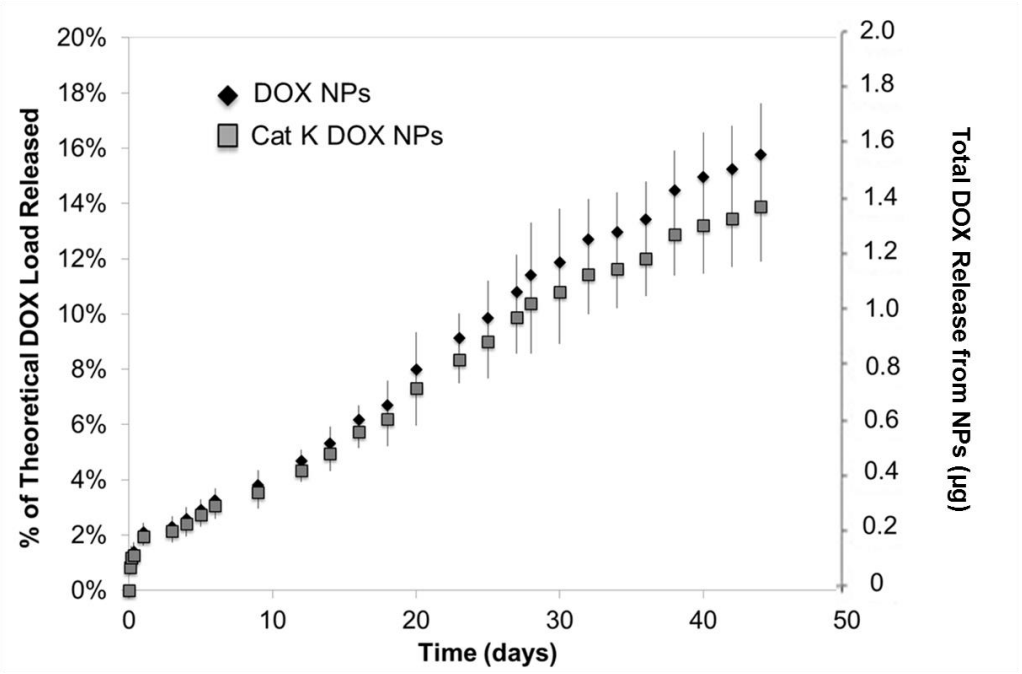

Figure 4.8. DOX release profiles *in vitro* from cathepsin K Ab-conjugated and unconjugated NPs loaded with 2% w/w DOX (mean ± SD; n = 3 per group)[112].

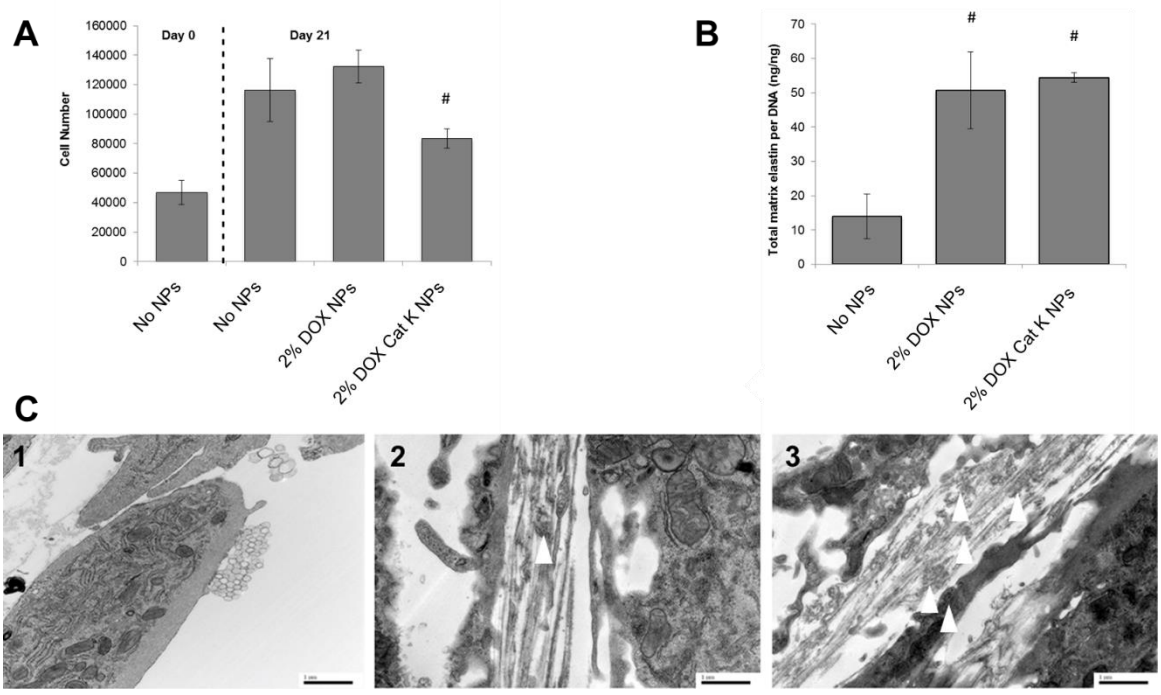

Figure 4.9. The proliferation of EaRASMCs is not impacted by culture with DOX-NPs (cathepsin K Ab-conjugated or unmodified), although cell proliferation in the cultures treated with the Ab-conjugated NPs was significantly lower than that cultured with the unmodified NPs (A) (mean ± SD; n = 3 cultures per group; # denotes significance of

differences versus unconjugated DOX-NPs, deemed for $p < 0.05$). (B) Cathepsin K antibody conjugation of DOX-NPs does not alter their pro-elastogenic effects on cultured EaRASMCs. The amount of deposited elastic matrix was normalized to DNA content of the respective cell layers (mean ± SD; n =3 cultures per group; # denotes significance of differences relative to treatment controls deemed for $p < 0.05$). (C) TEM images showing effects of cathepsin K Ab-conjugated and unconjugated DOX-NPs on elastic matrix deposition in TNF-α stimulated EaRASMC cultures. Elastic matrix deposition was sparse in the (1) NP-untreated cultures and few amorphous elastin deposits and no mature fibers were seen. Numerous forming elastic fibers were seen in the NP-treated cultures (2), with a greater number of amorphous elastin deposits (white arrows) associated with the microfibril components in the cultures that received (3) cathepsin K Ab-conjugated DOX-NPs. Scale bars: 1 μm[112].

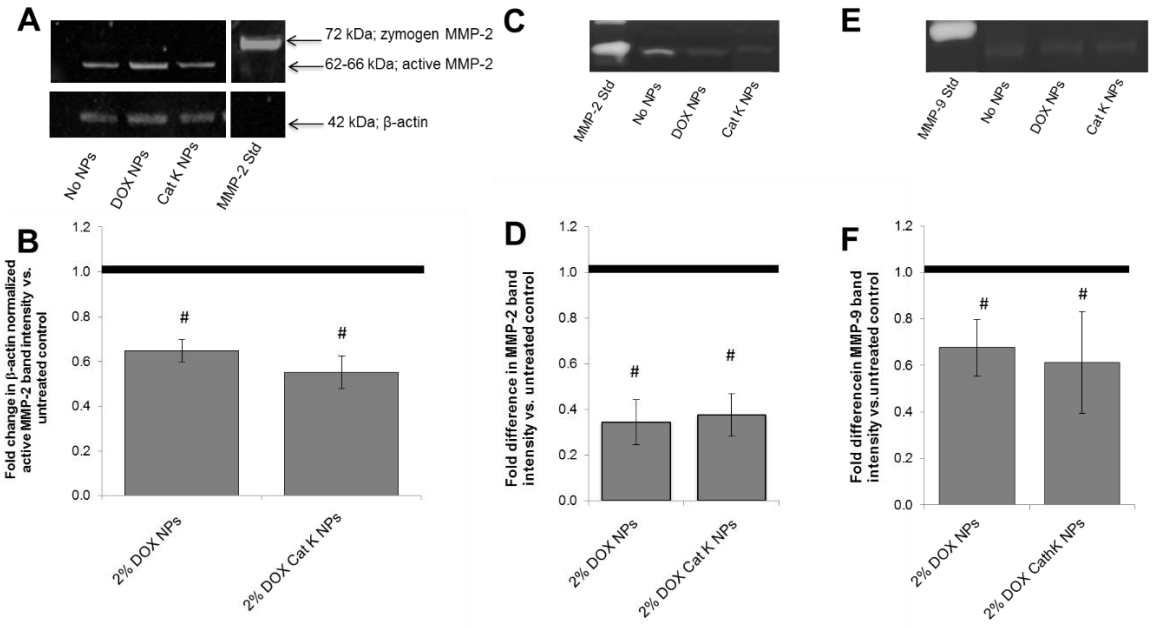

Figure 4.10. Panels A and B show the effects of unconjugated and cathepsin K Ab-conjugated DOX-NPs on MMP-2 protein synthesis in TNF-α stimulated EaRASMCs, as analyzed by western blots. Panel A shows a representative blot. Panel B shows fold difference in β-actin normalized band intensity for active MMP-2 protein in DOX-NP-treated EaRASMC layers, relative to control cultures cultured with no NPs (mean ± SD; n = 3 cultures/condition). # indicates significant differences versus controls (assigned a value of 1.0) deemed for a p *value* < 0.05. Panels C-F show effects of unconjugated and cathepsin K Ab-conjugated DOX-NPs on MMP-2 and MMP-9 activity in TNF-α activated EaRASMCs, as analyzed by gel zymography. Panels C and E show representative images of gel zymogram for MMP-2 and MMP-9, respectively. Panels D and F show fold difference in β-actin normalized MMP-2 and MMP-9 band intensities compared to NP-free control cultures, respectively (assigned value of 1.0; dotted line). Values shown indicate mean ± SD based on analysis of n = 3 cultures per condition. # denotes significance of differences versus control cultures, deemed for $p < 0.05$[112].

4.7. Assessment of αvβ3-Integrin expression in Human Umbilical Vein Endothelial Cells (HUVECs)

In order for the αvβ3-integrin Ab-conjugated NPs to target the integrin in endothelial cells, it was crucial to determine the expression of αvβ3-integrin in TNF-α stimulated cells compared to unstimulated cells. The HUVECs were stimulated with TNF-α for 24 hours prior to IF staining. In the unstimulated cells (**Figure 4.11.A**), the expression of the αvβ3-integrin is constant across the cell layer with minimal gaps forming between cells. However, compared to the TNF-α stimulated cells (**Figure 4.11.B**), the αvβ3-integrin expression is increased along the contact points with other cells and gaps begin to form between cells. The stimulation with TNF-α is expected to have this effect on αvβ3-integrin expression as this is similar to diseased state cells. The αvβ3-integrin is involved in cell migration and movement, so conjugating the αvβ3-integrin Ab to the NP surface will increase the passage of the NPs through the endothelial cell layer to the target SMCs.

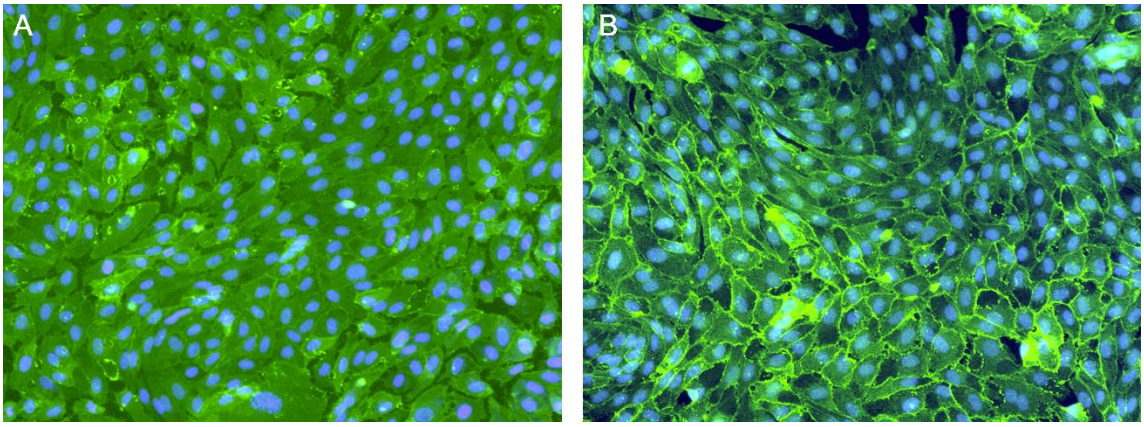

Figure 4.11. Expression of αvβ3-integrin in (A) unstimulated HUVECs and (B) TNF-α stimulated HUVECs. The αvβ3-integrin appears green (AF488-tagged secondary antibody) and the nuclei appears blue (DAPI). Expression of the αvβ3-integrin is increased when the HUVECs are stimulated with TNF-α.

4.8. Assessment of cadherin expression in HUVECs

Cadherins are a trans-membrane protein that play a vital role in cell-to-cell contact and adhesion. The formation of junctions between cells through cadherins provides the necessary binding to keep the endothelium intact. The disruption of cadherins can be caused by cytokine overexpression in diseased states, such as AAA. For this purpose, cadherin expression by ECs was examined *in vitro*. HUVECs were untreated (**Figure 4.12.A**) or stimulated with TNF-α (**Figure 4.12.B**) and labeled with the cadherin Ab for IF. The unstimulated HUVECs in **Figure 4.12.A** show consistent cadherin expression along the cell edges and there is minimal gaps between cells. In the TNF-α stimulated cells in **Figure 4.12.B**, the expression of cadherin around the cell edge decreases and the formation of gaps between cells begins to appear. The formation of gaps between cells is significant because this leads to a leaky endothelium similar to the endothelium found in AAAs. The leaky endothelium can be useful in the targeting of the NPs to the AAA due to the fact the NPs can pass through the gaps formed between cells and reach the SMCs which is crucial in regenerating the elastic matrix.

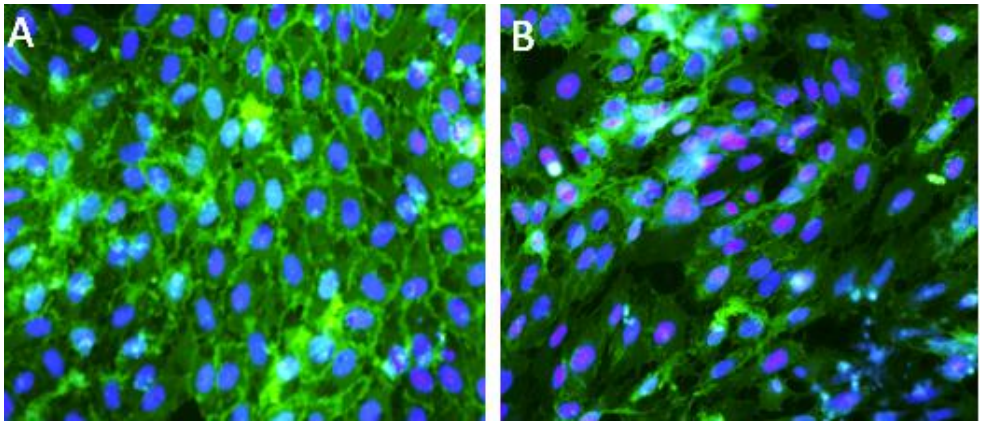

Figure 4.12. Cadherin expression in HUVECs of unstimulated control cells (A) compared to TNF-α stimulated cells (B). Cadherin appears green (AF488-tagged secondary antibody) and the nuclei appears blue (DAPI). The expression of cadherin decreases

following TNF-α stimulation in HUVECs and large micron-sized gaps form between cells[113].

4.9. Assessment of αvβ3-Integrin Ab incorporation on NP surface

The conjugation of the αvβ3-integrin Ab to the surface of the NPs was confirmed via fluorescent microscopy (**Figure 4.13**). In **Figure 4.13**, unconjugated NPs (**A**) fluoresce red and the αvβ3-Integrin Ab-conjugated NPs with the 488 fluorescent secondary (**B**) fluoresce yellow. The AF488 secondary antibody fluoresces green but when the red and green signals overlap, the fluorescent signal appears yellow. The overlapping of these signals and the yellow fluorescence present in the images confirms the conjugation of the αvβ3-Integrin Ab to the NP surface.

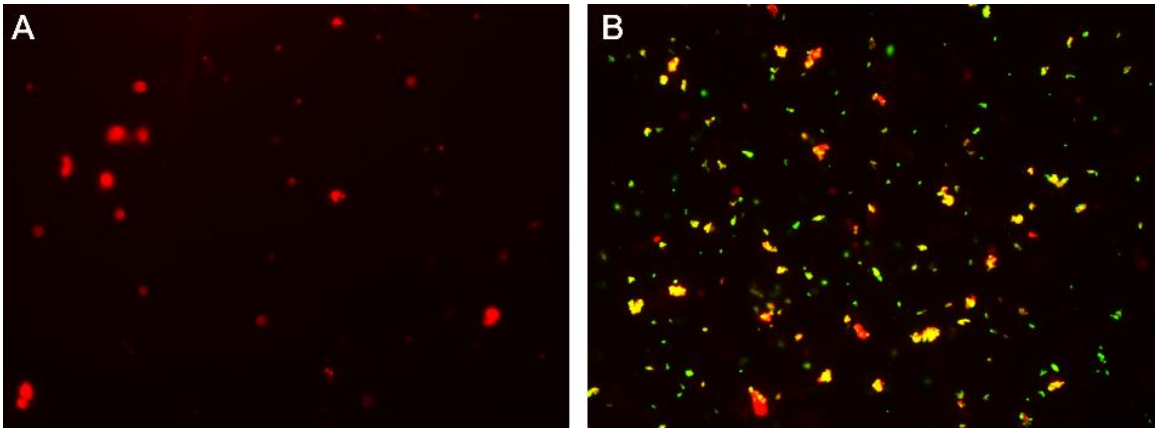

Figure 4.13. Microscope images of conjugation of αvβ3-integrin Ab to NP surface. Panel A shows control AF633 NPs without Ab conjugation and Panel B shows the addition of the αvβ3-integrin Ab to the NP surface and labelled with a 488 secondary antibody.

4.10. FITC-Dextran migration through a HUVEC layer

To test the migration of the NPs through the endothelium, it was first decided to test the passage of FITC-Dextran through a disrupted HUVEC layer comparable of that in

the AAA wall. The FITC-Dextran used for this experiment was 150 kDa as this size should be larger than the NPs used in following experiments. The FITC-Dextran was allowed to migrate through the stimulated and unstimulated HUVECs and the fluorescence was measured using a plate reader (**Figure 4.14**). The stimulation of HUVECs with TNF-α increased the passage of FITC-Dextran through the disrupted cell layer with minimal interference from the PET membrane. This result correlates with the cadherin IF result and the gap formation between cells allows for the passage of molecules through the endothelial cell layer. Based on this result, the next step was to determine if the NPs show similar migration patterns and if the conjugation with the αvβ3-integrin Ab increases NP passage.

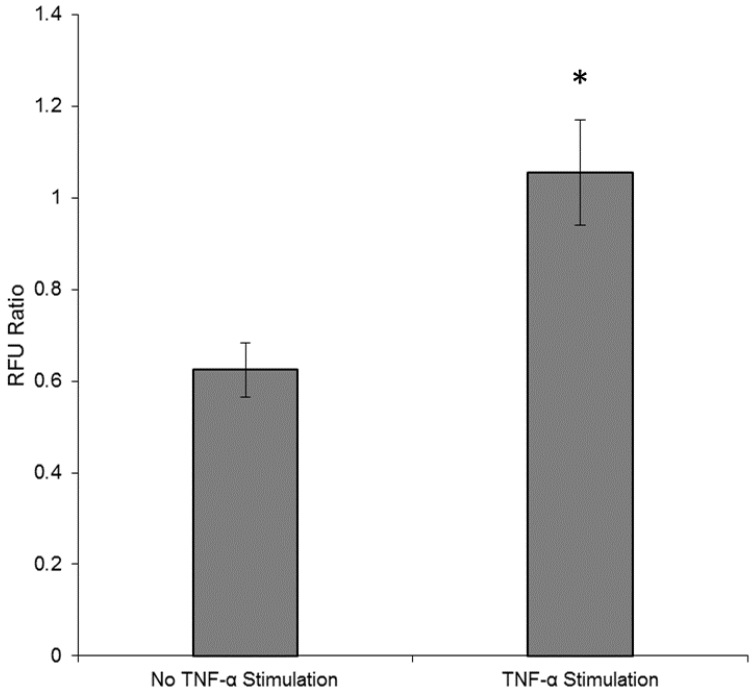

Figure 4.14. The migration of FITC-Dextran was significantly higher through a TNF-α stimulated endothelial cell layer compared to an unstimulated cell layer. The improved passage through the cell layer is due to the formation of gaps between the cells. * denotes significance of difference, deemed for $p < 0.05$[113].

4.11. NP migration through the endothelial cell layer

Building off the above data, it was necessary to determine the migration of the NPs through the HUVEC layer. HUVECs seeded on membranes containing 1.0 μm pores were incubated with αvβ3-integrin Ab-conjugated NPs or with unconjugated NPs and were unstimulated or stimulated with TNF-α (**Figure 4.15**). The data suggests there is no difference between NP migration when the HUVECs were stimulated or unstimulated and cultured with unconjugated NPs. However, the migration of the NPs was slightly lower than the blank membrane without cells so the cell layer is preventing the passage of some NPs. Finally, the HUVECs cultured with the αvβ3-integrin Ab-conjugated NPs and stimulated with TNF-α showed the greatest migration of NPs through the cell layer. The migration of the conjugated NPs is expected but the migration of the unconjugated NPs through the cell layer is greater than expected. One possible explanation for the migration of the unconjugated NPs through the cell layer is the NPs are taken up by the HUVECs through endocytosis and are passed through the cell and expelled on the other side. Another possible explanation is the formation of a confluent cell layer and the formation of gaps between cells that allow for the NP passage. To confirm the localization of the NPs in the HUVECs, confocal images were taken to identify where NPs were passing through the cell layer.

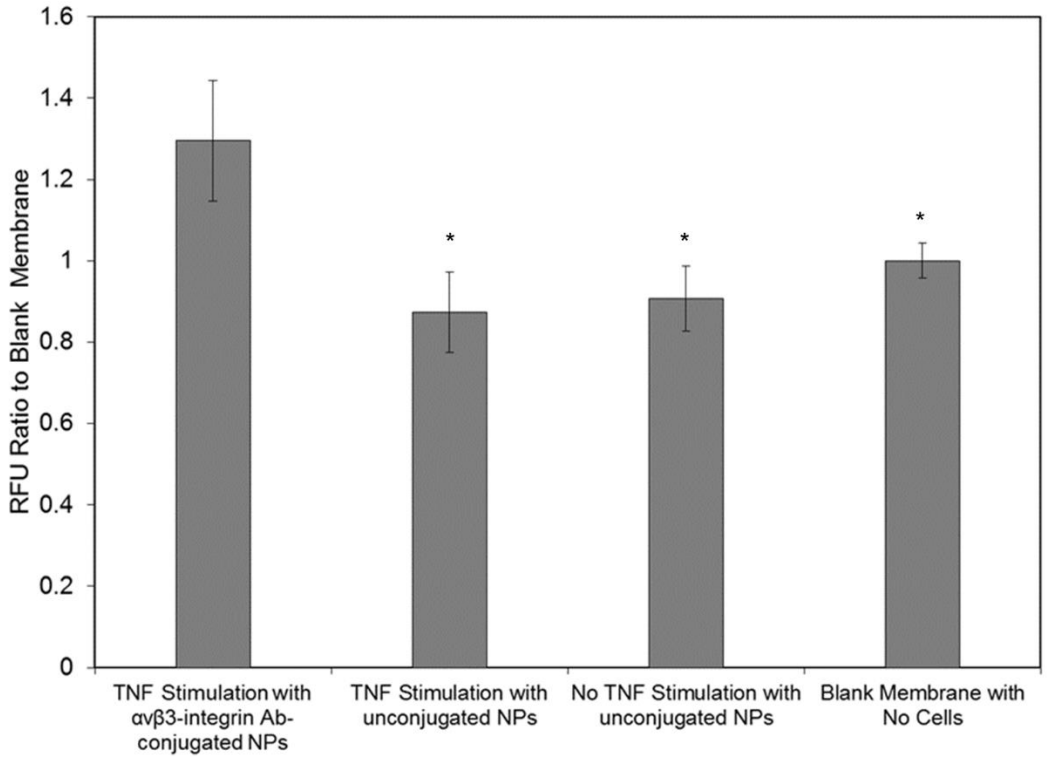

Figure 4.15. Migration of αvβ3-integrin Ab-conjugated NPs and unconjugated NPs through the endothelial cell layer. The modification of the NPs with an αvβ3-integrin Ab slightly increased the passage of the NPs through the endothelial cell layer while the unconjugated NPs were able to migrate through the cell layer but to a lesser extent. * denotes significance of differences versus TNF-α stimulation with αvβ3-integrin Ab-conjugated NPs, deemed for $p < 0.05$

4.12. NP localization in the HUVEC layer

The passage of the NPs through the HUVEC layer was deemed crucial to be able to deliver the NPs to SMCs in the medial layer of the aorta. The previous data has demonstrated the ability of the NPs to migrate past endothelial cell layer but it is necessary to determine if the NPs are passing through the cells or via the gaps between adjoining ECs. Using AF633-loaded NPs (pseudo-colored green), it was possible to determine the localization in the cell layer (**Figure 4.16** and **Figure 4.17**).

In **Figure 4.16**, HUVECs were stimulated with TNF-α and cultured with αvβ3-integrin Ab-conjugated NPs followed by membrane staining (red) and nucleus staining (blue). Using a confocal microscope, the XY, XZ, and YZ planes were visualized. Using only the XY plane, the location of the NPs cannot be accurately determined. The NPs could be localized on the cell surface but using the XZ and YZ planes, the NPs are located within the cell. The XZ and YZ planes shown in **Figure 4.16** are cross sections of the cell and confirm the αvβ3-integrin Ab-conjugated NPs are located within the cell. This is due to (1) the NP presence around the nucleus and (2) the appearance of the membrane surrounding the NPs.

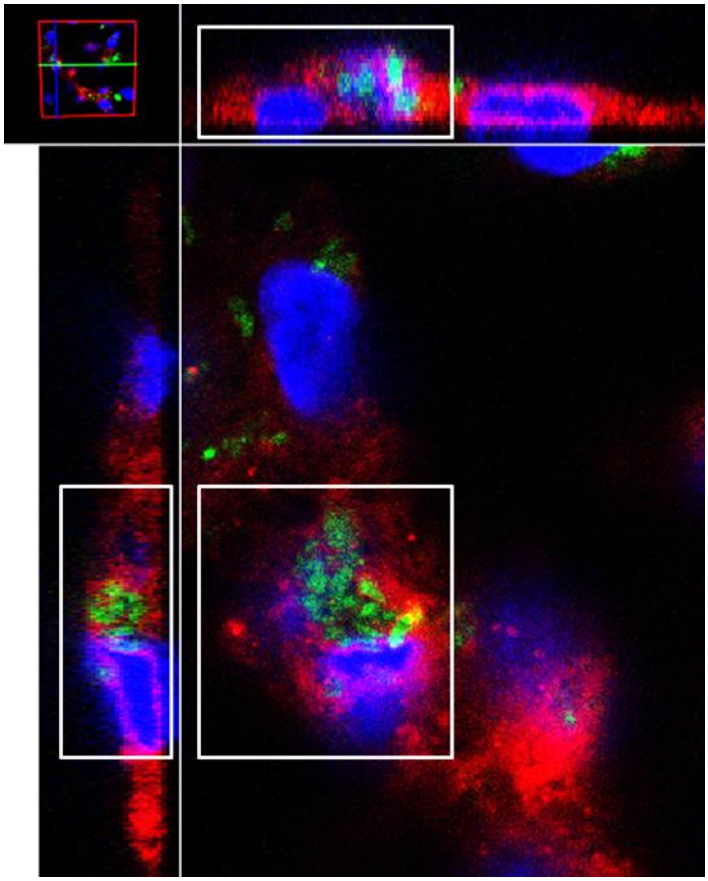

Figure 4.16. Localization of αvβ3-integrin Ab-conjugated AF633-loaded NPs in HUVECs following TNF-α stimulation. The conjugated NPs are localized within the cell as shown in the XZ and YZ axis. The membrane stain (red) allowed for the location of the NPs to be determined.

In **Figure 4.17**, the HUVECs were treated with unconjugated AF633-loaded NPs (pseudo-colored green) and the localization of the unconjugated NPs (A) was determined and compared to the localization of the αvβ3-integrin Ab-conjugated NPs. The unconjugated NPs location was confirmed by imaging the cell layer at various planes. The image of the cell surface (B) shows minimal fluorescence from the NPs but the images at different planes through the cell layer (C) showed an increase in NP fluorescence as the plane moved down through the cell. Another important aspect besides the localization of the NPs within the cell, is the localization of the NPs between the cells (D). The appearance of the NPs in the gaps between cells and within the cell regardless of Ab-conjugation correlate with previous results.

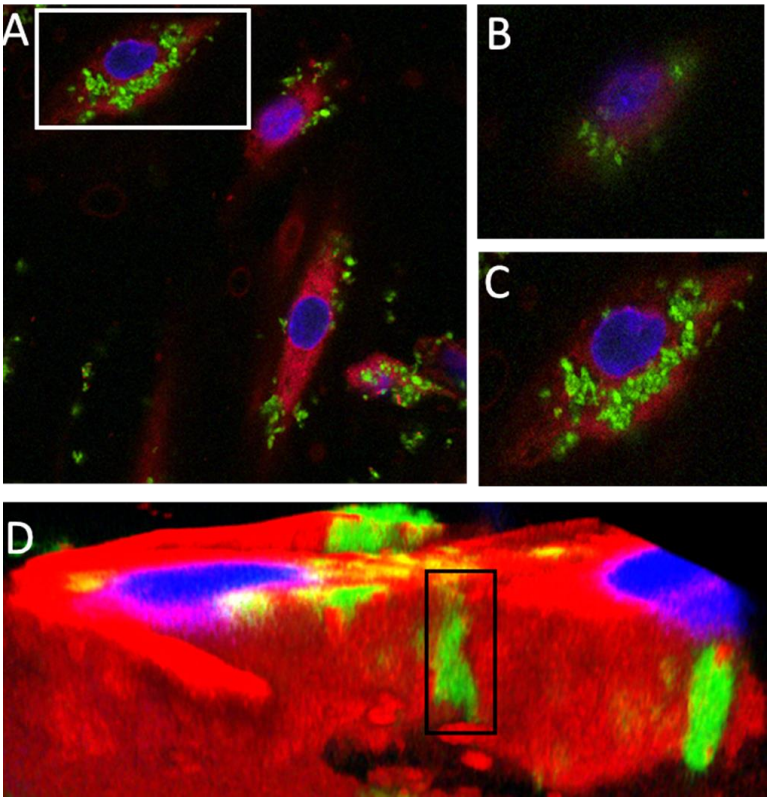

Figure 4.17. HUVECs treated with unconjugated AF633-loaded NPs (pseudo-colored green) (A). The NP's location was confirmed by imaging the cell surface (B). Minimal

fluorescence from the NPs was observed at the apical cell surface. Imaging at different planes through the cell layer (C) showed an increase in NP fluorescence as the plane moved through the cell. In addition to NP migration through the cell, the NPs were shown to move through the gaps between cells (D)[113].

4.13. Effect of DOX-loaded NPs on oxidative stress in HUVECs and EaRASMCs in culture

Induction of oxidative stress and generation of reactive oxygen species (ROS) in cultured HUVECs and EaRASMCs by DOX-loaded NPs were evaluated as an affirmative outcome could impede the use of NPs for AAA treatment (**Figure 4.18**). The DOX-loaded NP-treated cultures were compared to untreated cells and a positive and negative control. For both the HUVECs and EaRASMCs, the DOX-loaded NPs did not increase the oxidative stress compared to the untreated cells and was significantly lower than the positive control (**Figure 4.18.A**). Similarly for the superoxide assay, the DOX-loaded NPs did not increase superoxide production compared to untreated cells (**Figure 4.18.B**). This result confirms the DOX-loaded NPs, which were used throughout this study, do not induce a stress response from either cell type.

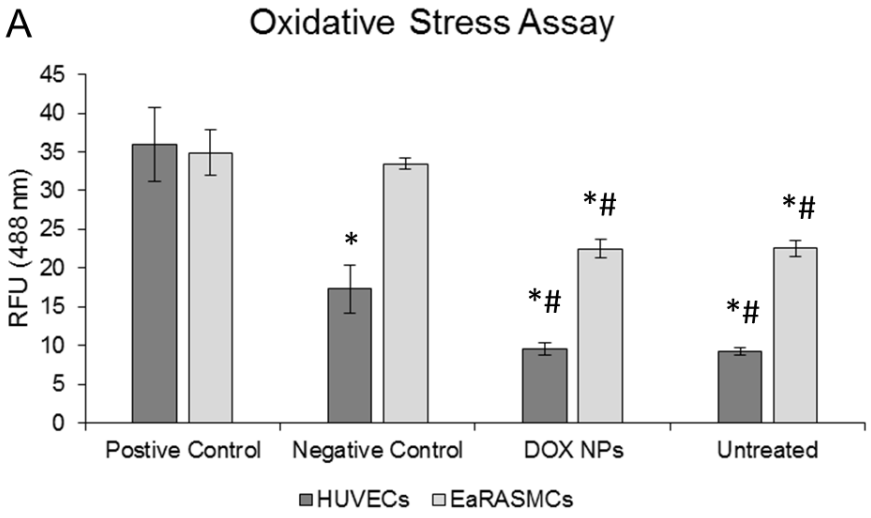

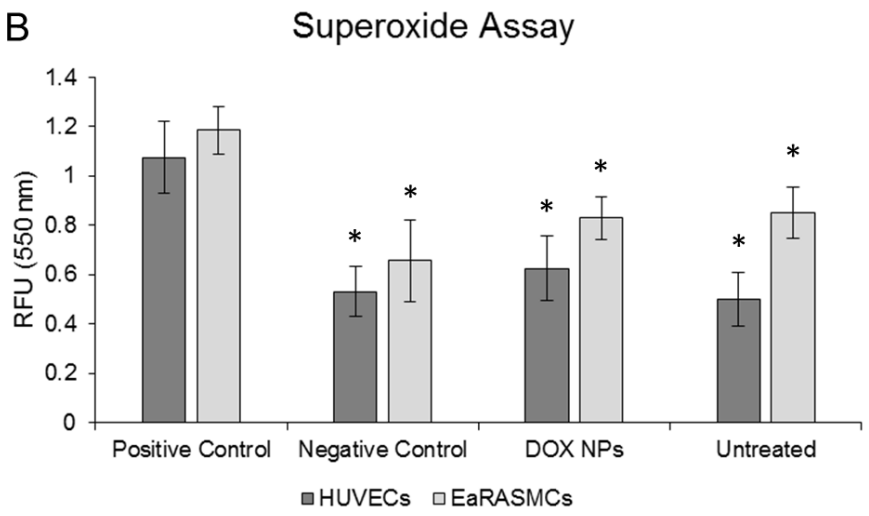

Figure 4.18. HUVECs and EaRASMCs were exposed to DOX-loaded NPs and no NPs to determine the (A) oxidative stress and (B) superoxide production triggered by the NPs. The presence of DOX-loaded NPs did not increase oxidative stress or superoxide production. * denotes significance of difference versus positive control, deemed for $p < 0.05$. # denotes significance of difference versus negative control, deemed for $p < 0.05$[113].

4.14. Assessing elastase-induced endothelial disruption in whole vessels

Elastase infusion induced matrix injury within porcine carotid arteries *ex vivo* was used to evoke the AAA. The elastase breakdowns the extracellular matrix and effectively disrupts the endothelial cell layer. **Figure 4.19** shows TEM images of healthy and disrupted endothelial cell layers when porcine carotid arteries are treated with elastase. **Figure 4.19.A** and **Figure 4.19.C** highlights the intact endothelial cell layer of the artery following treatment with saline. The endothelial cells maintain tight junctions as shown in **Figure 4.19.C**. However, compared to **Figure 4.19.B** and **Figure 4.19.D**, the elastase treated artery exhibits a denuded endothelium with the basement membrane visibly disrupted. The disruption of the endothelium and basement membrane are consistent with abdominal aortic aneurysms suggesting treatment with elastase is a viable option for inducing an aneurysm. Besides the relationship to the aneurysm, the disruption of the

endothelium may play a vital role in NP migration and uptake by the AAA. Previous results in this study confirmed NP migration through the endothelial cells and gaps formed between cells and the disrupted endothelium and basement membrane following elastase treatment provide a large gap for NPs to migrate through.

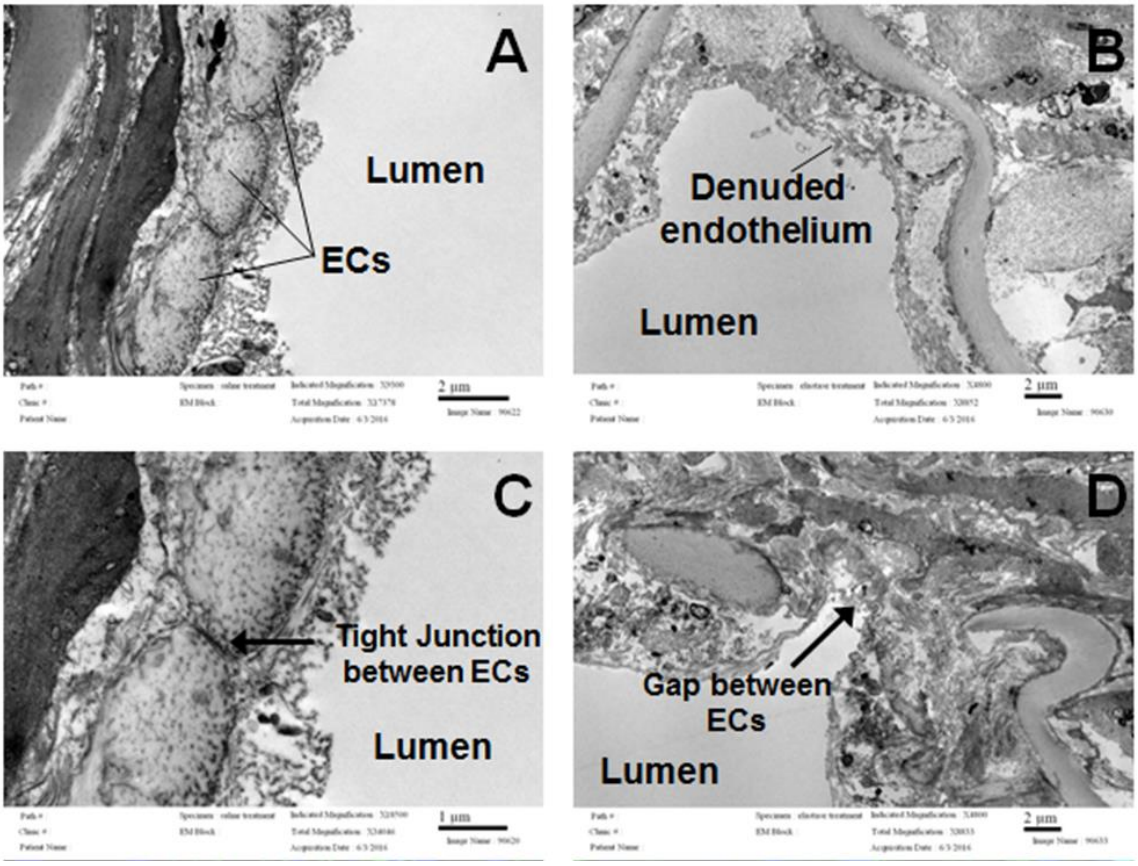

Figure 4.19. TEM images of (A and C) healthy porcine carotid artery infused with saline and (B and D) porcine pancreatic elastase treated porcine carotid artery.

4.15. AAA induction in rat model

The abdominal aortic aneurysm in the rat model was induced through periadventitial elastase treatment. **Figure 4.20.A** is a representative image of an aorta prior to elastase treatment in a male rat while **Figure 4.20.B** shows the aorta immediately

following elastase treatment. Immediately following treatment, the aorta changes from a red color to a white color indicating damage due to elastase. In **Figure 4.20.C**, the same aorta is shown following aneurysm development over several weeks.

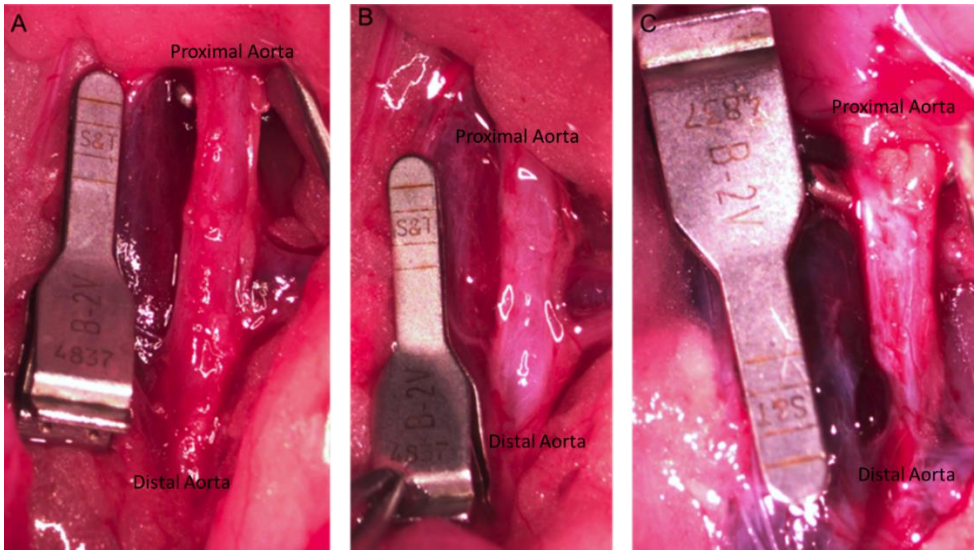

Figure 4.20. Surgical images of aneurysm induction through periadventitial elastase treatment in a rat model. Panel A shows the exposed aorta prior to elastase treatment and Panel B shows the aorta immediately post-treatment. In Panel C, the aorta is exposed following aneurysm development.

The aneurysm induction surgery was performed on multiple rats (n=3) and images were taken prior to treatment and following aneurysm development. **Figure 4.21** shows the average diameter of the aorta for three rats following treatment with elastase (1 ml of 20 units). The figure shows an increase in aorta diameter for two of the rat models while one aorta showed no increase (66.7% success rate). The increase in diameter was relatively small as we intended to achieve, unlike the large AAAs we were able to generate previously following elastase infusion/stretch-induced injury[110]. In the latter case, the ballooning of the aorta upon elastase infusion may allow the elastase to penetrate into the medial layer

of the aorta to more effectively disrupt the elastic matrix and hence generate a larger aneurysmal expansion.

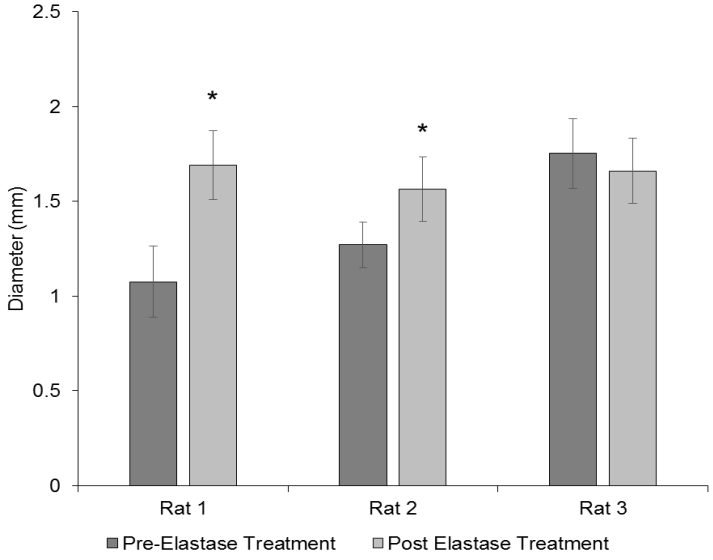

Figure 4.21. Diameter measurements of rat aorta treated with 1 ml of 20 units of elastase. The measurements were obtained from images before elastase treatment and after a 14 day aneurysm development period. * denotes significance of difference compared to pre-elastase treatment, deemed for $p < 0.05$.

4.15.1. AAA imaging and measurement using MRI

The use of MRI allows longitudinal monitoring of aneurysm growth following AAA induction surgery in a single animal without need for laparotomy. **Figure 4.22** shows multiple MRI scans of the abdominal aorta in a healthy (**Figure 4.22.A** and **Figure 4.22.B**) and elastase treated rat (**Figure 4.22.C** and **Figure 4.22.D**). **Figure 4.22.A** shows the aorta from below the kidneys to the bifurcation in the lower abdomen and **Figure 4.22.B** shows a 3D rendering of the same aorta. The 3D rendering provides a clear visual representation of the aorta and would allow for localized expansion to be clearly viewed. **Figure 4.22.C** shows the aorta from the kidneys to the bifurcation in an elastase-injured rat. **Figure 4.22.D** is a 3D rendering of the aorta and the image has been rotated 30°. The rendering

enables visualization of the aorta from multiple angles so if the localized expansion is not in the coronal plane, it can be seen in another plane. An example of a small expansion can be seen in **Figure 4.22.D** highlighted by the red box. Though the purpose of these initial MRI imaging protocols was to merely optimize imaging parameters for reliable assessment of aneurysm/aorta size and spatiotemporal differences in the same rat, which is still ongoing, our initial imaging outcomes at the very least however, demonstrate our success in generating early aneurysmal expansions which exhibit significant spatial anisotropy.

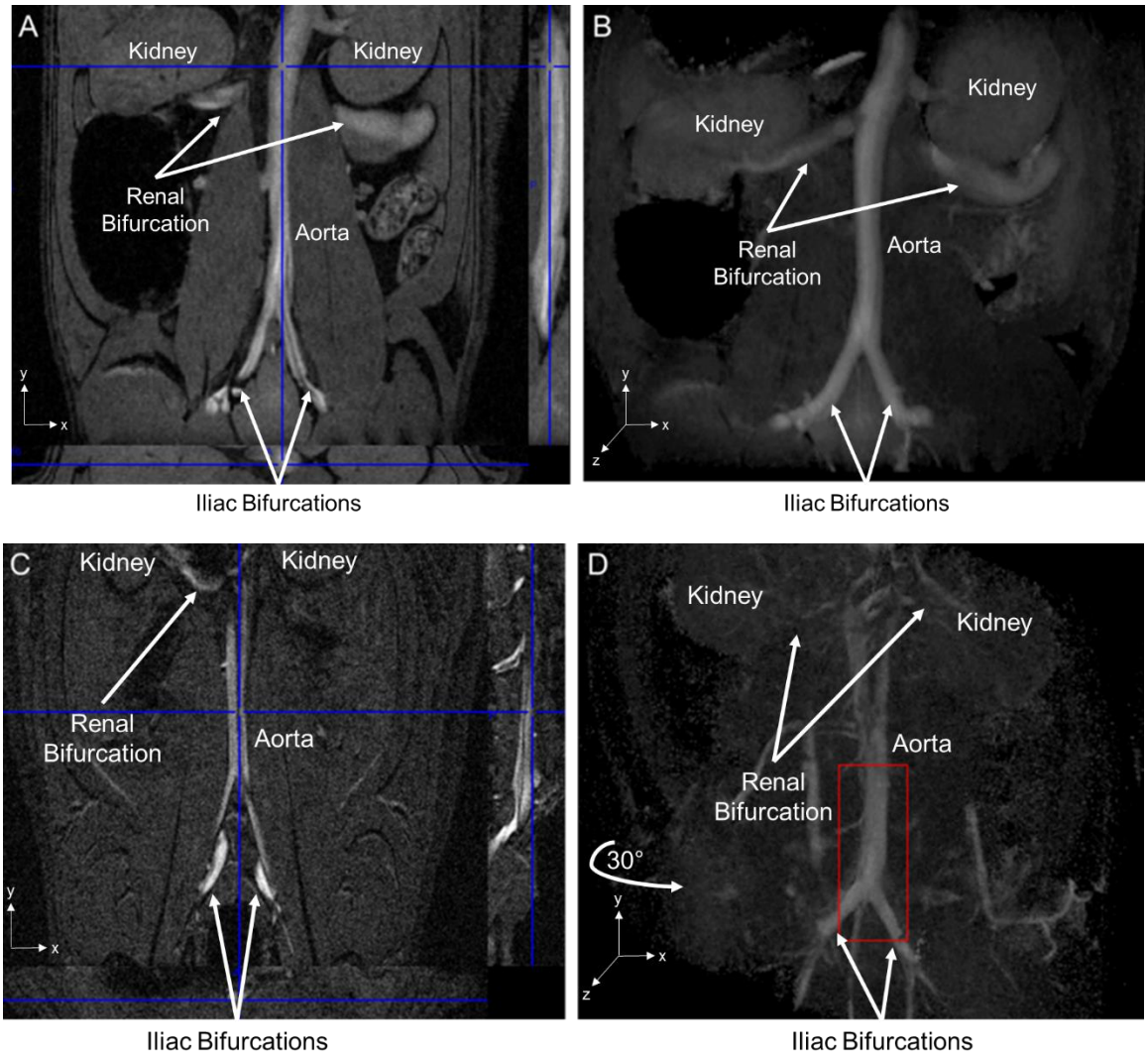

Figure 4.22. MRI scans of a healthy (A, B) and elastase treated (C, D) aorta in a rat model. The healthy rat aorta (A) was clearly shown in the MRI scan and this enabled diameter

measurements. Using the same aorta, a 3D rendering (B) was generated which allows for further visualization of the aorta. The elastase treated aorta (C) was visualized using the same protocol as the healthy aorta. The elastase injured aorta was 3D rendered (D) to visualize any expansions from treatment.

4.15.2. NP localization in rat AAA model

Preliminary *in vivo* infusion studies were performed on VivoTag 800® loaded cathepsin K Ab-conjugated NPs. The expression of cathepsin K in the elastase-injured rat AAA model was increased compared to the healthy aorta (**Figure 4.23**). The expression of cathepsin K in the aorta will be the target for the cathepsin K-Ab conjugated NPs. The cathepsin K Ab-conjugated NPs were injected via tail vein injection and allowed to circulate for 1 or 3 hours. The rat was euthanized and the aorta imaged using an IVIS Spectrum CT whole tissue imager. Preliminary results (**Figure 4.24** and **Figure 4.25**) show localization of the NPs within the aortal segment in the abdomen. **Figure 4.24.A** shows the exposed aorta with the cathepsin K Ab-conjugated NPs (pseudo-colored blue) localized. **Figure 4.24.B** and **Figure 4.24.C** are control images in which the injection site of the cathepsin K Ab-conjugated NPs is visible due to the NPs present (**B**) and the residual NPs visualized in the vial (**C**). These results are promising as preliminary data and further investigation is warranted. The biodistribution (**Figure 4.25**) was determined using similar imaging methods with images of the chest cavity (**Figure 4.25.A** and **Figure 4.25.B**) and the abdominal cavity (**Figure 4.25.C** and **Figure 4.25.D**) to determine the location of NPs. The preliminary data shows the localization of the NPs in the abdominal aorta and the chest cavity. However, longer term NP biodistribution, retention, and safety studies need to be performed as a function of NP dose and time in AAA-induced rats, which have been initiated.

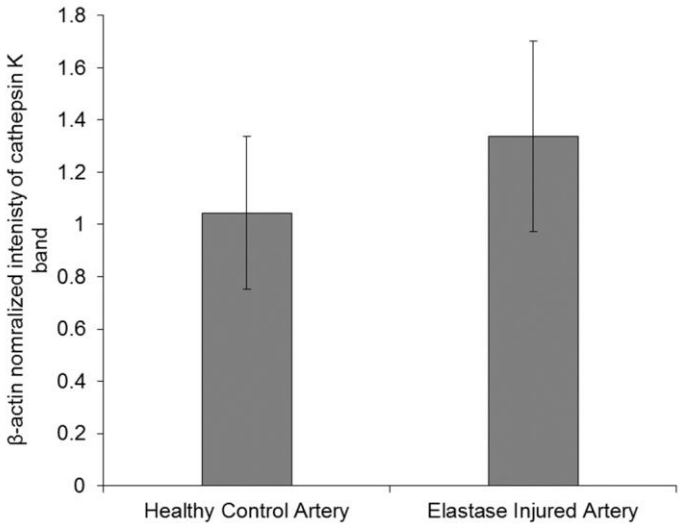

Figure 4.23. Relative expression of cathepsin K in healthy and elastase injured rat AAA models. The plot shows β-actin normalized cathepsin K band intensity (n = 3 per case).

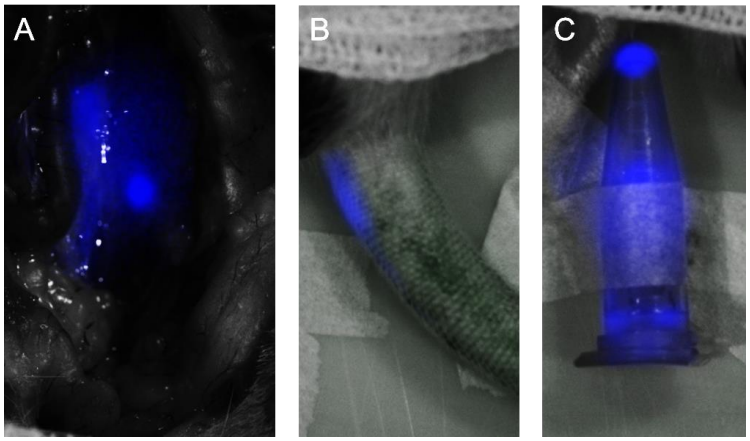

Figure 4.24. Preliminary results of cathepsin K Ab-conjugated VivoTag 800®-loaded NP localization in an AAA rat model. (A) The exposed aorta of the rat following tail vein injection of the NPs. (B) The injection site of the NPs visible 1 hour post injection. (C) The residual NPs in the vial as a control for NP fluorescence. NPs are pseudo-colored blue.

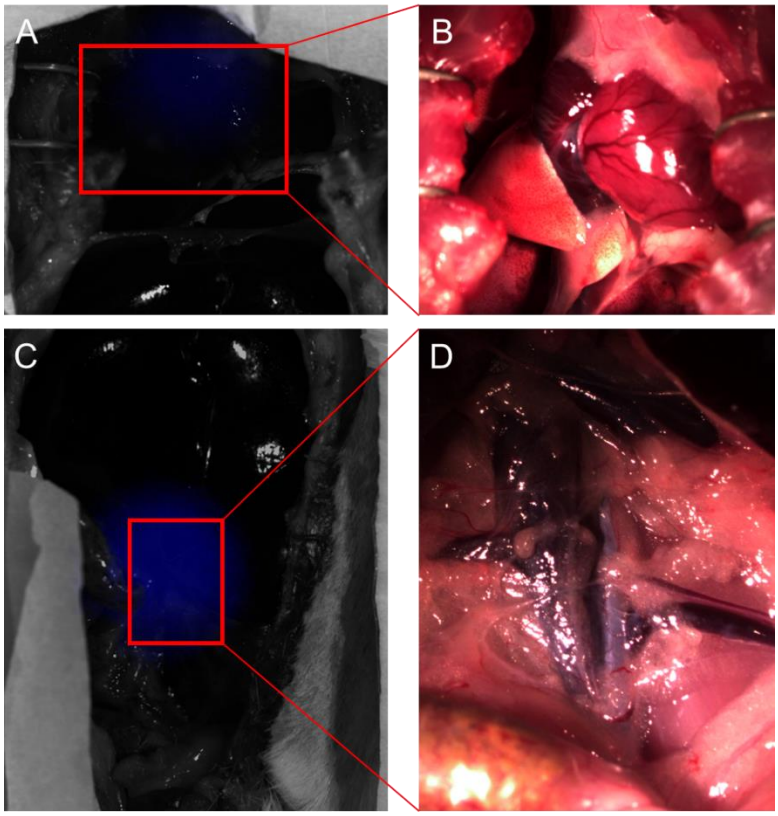

Figure 4.25. Biodistribution of VivoTag 800®-loaded NPs in elastase-injured rat AAA model 3 hours post-injection. The fluorescent image of the chest (A) show fluorescence from the NPs while (B) shows the organs imaged. The fluorescence of the abdominal cavity (C) shows fluorescence from the NPs and (D) shows the aorta and other organs imaged.

CHAPTER V

CONCLUSIONS AND RECOMMENDATIONS

5.1. Conclusions

The goal of this study was to investigate cathepsin K Ab surface functionalization of our matrix regenerative DOX NPs as an effective means of targeting them to the AAA wall following a simple intravenous infusion protocol. Towards rationalizing and guiding rigorous studies to investigate the biodistribution, safety and therapeutic efficacy of these nanoformulations in a pre-clinical rat model of elastase-induced AAAs, this study has successfully fulfilled the sub-aims of a) demonstrating cathepsin K as a viable target for homing in NPs to the AAA wall, b) showing that cathepsin K Abs can be stably functionalized on the polymer NP surface with no adverse implications to their physical properties and beneficial pro-elastic matrix regenerative (i.e., increased elastic matrix synthesis, crosslinking, fiber formation) and anti-proteolytic effects, and to cellular health, and c) generating evidence supporting trans-endothelial transport of the NPs from the AAA vessel lumen to the underlying disrupted aortal medial layer. More specifically, our study generated the following findings:

- Cathepsin K expression is significantly increased in EaRASMCs when stimulated by TNF-α, a cytokine known to be over-expressed in the AAA wall. Cathepsin K expression is primarily localized on the cell membrane which can be readily accessed by NPs.
- Elastase-induced vessel injury, our model to generate AAAs, triggers significant increases in cathepsin K expression in the vessel wall, both *ex vivo* (in porcine carotids) and *in vivo* (rat model), likely associated with increased expression of the enzyme by aneurysmal SMCs as described above.
- Covalent conjugation results in efficient and stable functionalization of the NP surface with the cathepsin K Ab, with no significant changes to NP size, charge, DOX release, and the pro-elastic fiber neoassembly-augmenting and anti-MMP effects attributed to the cationic amphiphile-surface modified PLGA nanocarrier and released active agent, DOX. In addition, the NPs at the doses deemed appropriate to deliver the useful DOX dosing level do not incite oxidative stress or generation of reactive oxygen species in cultured EaRASMCs and HUVECs.
- Elastase-induced vessel injury, and associated TNF-α overexpression have been separately shown to cause activation and disruption/denudation of an intact endothelial layer as demonstrated within the vessel wall and in HUVEC cultures respectively. Where retained, the ECs lose expression of their cadherin junctions that maintain contact between adjacent cells to develop microns-sized gaps between, and also exhibit upregulated expression of αvβ3-integrins along their periphery.
- Cathepsin K Ab-conjugated NPs are able to migrate across a disrupted endothelial layer by both passive diffusion through inter-endothelial gaps, and by trans-cytosis.

In addition, αvβ3 Ab-modification of the NP surface provides additional opportunities in the future to augment endothelial binding and trans-endothelial transport of the NPs, although passive transport, in the absence of such targeting is itself significant.

- Initial *in vivo* infusion of VivoTag 800® cathepsin K Ab-conjugated NPs via the IV route indicated localization of the NPs in the abdominal aneurysm segment, with some additional fluorescence detected in the chest cavity, likely the lung. This promising data suggests effective but likely inefficient targeting of the NPs to the AAA wall using this modality.

5.2. Limitations and recommendations

Below we list key limitations of the experiments as conducted and recommendations for future follow-up investigations.

- The use of elastase for aneurysm induction provides a reproducible and effective mode for aorta disruption. However, in our experience as with that previously reported only ~66% of animals develop an aneurysm following periadventitial or infusion based aortal tissue injury. However, the infusion/vessel ballooning method allows elastase to penetrate between the stretched elastic lamellae causing more effective mechanical disruption of the wall structure compared to periadventitial elastase treatment, which in turn may enhance aneurysm formation and size. The technical skills required for elastase infusion are much greater than the elastase treatment but may produce a larger number of aneurysms in the rat models. While we have pursued the former method in this study for the purpose of simplicity, future *in vivo* studies will involve intraluminal elastase infusion which we had shown effective in a prior study[110].

- The use of the VivoTag 800®-loaded NPs enabled the visualization of the NPs in the rat AAA model. However, the rat had to be euthanized to allow for the aorta to be visualized. This was a significant limitation as several rat models would be needed for each time point for multiple time points. This would require a large number of animals as well as significant surgery time. To visualize the NPs without euthanizing, the NPs could be loaded with paramagnetic iron oxide NPs (SPIONs). We have recently published findings that show SPIONs to impart magnetic mobility to the DOX-NPs in an applied magnetic field and to not alter their physical or biological effects. The SPION-DOX NPs could then be conjugated with the cathepsin K Ab and injected via the tail vein or even better within the flow occluded AAA segment using a balloon drug delivery catheter and guided to the AAA wall by application of a preclinical MRI-generated external magnetic driving force. The NPs driven to the AAA wall in this manner would then 'stick' to the EaRASMC surface. The dual modality of active targeting of NPs could circumvent the otherwise unavoidable passage and removal of IV-infused NPs in the lungs en route to the aorta. SPIONs within the DOX-NPs can also help track their *in vivo* retention and biodistribution using MRI.
- Further investigation in the biodistribution of the cathepsin K Ab-conjugated NPs following tail vein injection is warranted. Preliminary data was collected in this study and was promising but additional data is necessary to confirm the targeting, retention and biodistribution of the NPs. The concentration of cathepsin K Ab-conjugated NPs injected was 10 mg/ml which was enough to produce fluorescence

in the rat model. However, this concentration may not be optimal to visualize localization as too much or too little could significantly affect the results.

- Finally, once the biodistribution of the NPs has been determined and the NPs can be localized to the AAA, the pro-elastogenic effects and anti-proteolytic effects of the DOX-loaded NPs will be examined *in vivo*.

REFERENCES

1. Basak T, Varshney S, Akhtar S, Sengupta S. Understanding different facets of cardiovascular diseases based on model systems to human studies: A proteomic and metabolomic perspective. *J Proteomics*. 2015;127:50-60. doi:10.1016/j.jprot.2015.04.027.

2. Heidenreich PA, Trogdon JG, Khavjou OA, et al. Forecasting the Future of Cardiovascular Disease in the United States. *Circulation*. 2011;123:933-944.

3. HEART DISEASE AND STROKE - AN OVERVIEW OF OUR NATION'S LEADING KILLERS. National Conference of State Legistlaturs. http://www.ncsl.org/research/health/heart-disease-and-stroke-an-overview.aspx. Published 2015.

4. Mozaffarian D, Benjamin E, Go A, et al. Heart disease and stroke statistics— 2016 update: a report from the American Heart Association [published online ahead of print December 16, 2015]. *Circulation*. doi:10.1161/CIR.0000000000000350.

5. Nordon IM, Hinchliffe RJ, Loftus IM, Thompson MM. Pathophysiology and epidemiology of abdominal aortic aneurysms. *Nat Publ Gr*. 2010;8:92-102. doi:10.1038/nrcardio.2010.180.

6. Norman PE, Powell JT. Abdominal aortic aneurysm: The prognosis in women is worse than in men. *Circulation*. 2007. doi:10.1161/CIRCULATIONAHA.106.671859.

7. DeRubertis BG, Trocciola SM, Ryer EJ, et al. Abdominal aortic aneurysm in

women: Prevalence, risk factors, and implications for screening. *J Vasc Surg*. 2007. doi:10.1016/j.jvs.2007.06.024.

8. Kravetz JD, Carbone VG, Federman DG. Improving abdominal aortic aneurysm screening with an electronic clinical reminder. *Am J Med*. 2010. doi:10.1016/j.amjmed.2010.04.028.

9. Kostun ZW, Malik RK. Screening for abdominal aortic aneurysms. *Clin Imaging*. 2015. doi:10.1016/j.clinimag.2015.12.009.

10. Laine MT, Vänttinen T, Kantonen I, et al. Rupture of Abdominal Aortic Aneurysms in Patients Under Screening Age and Elective Repair Threshold. *Eur J Endovasc Surg*. 2015:1-6. doi:10.1016/j.ejvs.2015.12.011.

11. Kuivaniemi H, Ryer EJ, Elmore JR, Tromp G. Understanding the pathogenesis of abdominal aortic aneurysms. *Expert Rev Cardiovasc Ther*. 2015;13(9):975-987. doi:10.1586/14779072.2015.1074861.

12. Abdul-Hussien H, Soekhoe RG V, Weber E, et al. Collagen degradation in the abdominal aneurysm: a conspiracy of matrix metalloproteinase and cysteine collagenases. *Am J Pathol*. 2007;170(3):809-817. doi:10.2353/ajpath.2007.060522.

13. Rieman DJ, McClung HA, Dodds RA, et al. Biosynthesis and processing of cathepsin K in cultured human osteoclasts. *Bone*. 2001;28(3):282-289. doi:10.1016/S8756-3282(00)00445-2.

14. Abisi S, Burnand KG, Waltham M, Humphries J, Taylor PR, Smith A. Cysteine protease activity in the wall of abdominal aortic aneurysms. *J Vasc Surg*.

2007;46(6):1260-1266. doi:10.1016/j.jvs.2007.08.015.

15. Crowther, PhD M, Goodall, BSc S, Jones JL, Bell, MD, FRCS PRF, Thompson, MD, FRCS MMT. Increased matrix metalloproteinase 2. *J Vasc Surg*. 2000;32(3):575-583.

16. Lv BJ, Lindholt JS, Wang J, Cheng X, Shi GP. Plasma levels of cathepsins L, K, and V and risks of abdominal aortic aneurysms: A randomized population-based study. *Atherosclerosis*. 2013;230:100-105. doi:10.1016/j.atherosclerosis.2013.05.018.

17. Curci JA, Petrinec D, Liao S, et al. Pharmacologic suppression of experimental abdominal aortic aneurysms: A comparison of doxycycline and four chemically modified tetracyclines. *J Vasc Surg*. 1998;28(6):1082-1093.

18. Fay D, Wyatt MG, Rose J. Endovascular stent grafting of descending thoracic aortic aneurysms. *Surgery*. 2004;25(8):346-349.

19. Tambyraja AL, Chalmers RTA. Aortic aneurysms. *Surg*. 2007;25(8):342-345. doi:10.1016/j.mpsur.2007.06.002.

20. Ballotta E, Da Giau G, Bottio T, Toniato A. Elective surgery for small abdominal aortic aneurys ms. *Cardiovasc Surg*. 1999;7(5):495-502.

21. Boyle JR, McDermott E, Crowther M, Wills A, Bell P, Thompson M. Doxycycline inhibits elastin degradation and reduces metalloproteinase activity in a model of aneurysmal disease. *Eur J Vasc Endovasc Surg*. 1998;27(2):354-361. doi:10.1016/S1078-5884(98)80008-7.

22. Bendeck MP, Conte M, Zhang M, Nili N, Strauss BH, Farwell SM. Doxycycline Modulates Smooth Muscle Cell Growth, Migration, and Matrix Remodeling after Arterial Injury. *Am J Pathol*. 2002;160(3):1089-1095. doi:10.1016/S0002-9440(10)64929-2.

23. Sivaraman B, Ramamurthi A. Multifunctional nanoparticles for doxycycline delivery towards localized elastic matrix stabilization and regenerative repair. *Acta Biomater*. 2013;9(5):6511-6525. doi:10.1016/j.actbio.2013.01.023.

24. Lee BK, Yun YH, Park K. Smart nanoparticles for drug delivery: Boundaries and opportunities. *Chem Eng Sci*. 2015. doi:10.1016/j.ces.2014.06.042.

25. Faraji AH, Wipf P. Nanoparticles in cellular drug delivery. *Bioorganic Med Chem*. 2009;17:2950-2962. doi:10.1016/j.bmc.2009.02.043.

26. Hans ML, Lowman AM. Biodegradable nanoparticles for drug delivery and targeting. *Curr Opin Solid State Mater Sci*. 2002;6:319-327.

27. Jong WH De, Borm PJ. Drug delivery and nanoparticles: Applications and hazards. *Int J Nanomedicine*. 2008;3(2):133-149.

28. Panyam J, Labhasetwar V. Biodegradable nanoparticles for drug and gene delivery to cells and tissue. *Adv Drug Deliv Rev*. 2003. doi:10.1016/S0169-409X(02)00228-4.

29. Pagels RF, Prud'Homme RK. Polymeric nanoparticles and microparticles for the delivery of peptides, biologics, and soluble therapeutics. *J Control Release*. 2015;219:519-535. doi:10.1016/j.jconrel.2015.09.001.

30. Kumari A, Yadav SK, Yadav SC. Biodegradable polymeric nanoparticles based drug delivery systems. *Colloids Surfaces B Biointerfaces*. 2010. doi:10.1016/j.colsurfb.2009.09.001.

31. Hahn C, Schwartz MA. Mechanotransduction in vascular physiology and atherogenesis. *Nat Rev Mol Cell Biol*. 2009;10(1):53-62. doi:10.1038/nrm2596.

32. Encyclopædia Britannica Online. Transverse Section of An Artery. Encyclopedia Britannica. https://www.britannica.com/science/artery/images-videos/Transverse-section-of-an-artery/121565. Published 2014.

33. Kozel BA, Hubmacher D. Pathology of the Elastic Matrix. In: Anand Ramamurthi and Chandrasekhar Kothapalli, ed. *Elastic Fiber Matrices Biomimetic Approaches to Regeneration and Repair*. Boca Raton: CRC Press; 2016:32-80.

34. Wagenseil JE, Mecham RP. Vascular extracellular matrix and arterial mechanics. *Physiol Rev*. 2009;89(3):957-989. doi:10.1152/physrev.00041.2008.

35. Newby AC, Zaltsman AB. Molecular mechanisms in intimal hyperplasia. *J Pathol*. 2000;190:300-309. doi:10.1002/(SICI)1096-9896(200002)190:3<300::AID-PATH596>3.0.CO;2-I.

36. Yau JW, Teoh H, Verma S. Endothelial cell control of thrombosis. *BMC Cardiovasc Disord*. 2015;15:130. doi:10.1186/s12872-015-0124-z.

37. Sukriti S, Tauseef M, Yazbeck P, Mehta D. Mechanisms regulating endothelial permeability. *Pulm Circ*. 2014;4(4):535-551. doi:10.1086/677356.

38. Bazzoni G. Endothelial tight junctions: permeable barriers of the vessel wall.

Thromb Haemost. 2006;95:36-42.

39. Alberts B, Johnson A, Lewis J, Raff M, Roberts K, Walter P. *Molecular Biology of the Cell*. 4th ed. New York: Garland Science; 2002.

40. Sandoo A, van Zanten JJCSV, Metsios GS, Carroll D, Kitas GD. The endothelium and its role in regulating vascular tone. *Open Cardiovasc Med J*. 2010;4:302-312. doi:10.2174/1874192401004010302.

41. Wolinsky H, Glagov S. A Lamellar Unit of Aortic Medial Structure and Function in Mammals. *Circ Res*. 1967;20:99-111.

42. Brooke BS, Bayes-Genis A, Li DY. New Insights into Elastin and Vascular Disease. *Trends Cardiovasc Med*. 2003;13(5):176-181. doi:10.1016/S1050-1738(03)00065-3.

43. Brooke BS, Karnik SK, Li DY. Extracellular matrix in vascular morphogenesis and disease: Structure versus signal. *Trends Cell Biol*. 2003;13(1):51-56. doi:10.1016/S0962-8924(02)00007-7.

44. Gonzalez MC, Arribas SM, Molero F, Fernandez-Alfonso MS. Effect of removal of adventitia on vascular smooth muscle contraction and relaxation. *Am J Physiol Hear Circ Physiol*. 2001;280(6):H2876-81. http://www.ncbi.nlm.nih.gov/entrez/query.fcgi?cmd=Retrieve&db=PubMed&dopt=Citation&list_uids=11356648.

45. Gutterman DD. Adventitia-dependent influences on vascular function. *Am J Physiol*. 1999;277(4 Pt 2):H1265-72.

http://www.ncbi.nlm.nih.gov/pubmed/10516160.

46. Danpinid A, Luo J, Vappou J, Terdtoon P, Konofagou EE. In vivo characterization of the aortic wall stress-strain relationship. *Ultrasonics*. 2010. doi:10.1016/j.ultras.2010.01.003.

47. Danpinid A, Luo J, Vappou J, Terdtoon P, Konofagou EE. Characterization of the stress-strain relationship of the abdominal aortic wall in vivo. In: *Proceedings of the 31st Annual International Conference of the IEEE Engineering in Medicine and Biology Society: Engineering the Future of Biomedicine, EMBC 2009*. ; 2009. doi:10.1109/IEMBS.2009.5333466.

48. Lodish H, Berk A, Zipursky SL, Matsudaira P, Baltimore D, Darnell J. Collagen: The Fibrous Proteins of the Matrix. In: *Molecular Cell Biology*. 4th ed. New York: W. H. Freeman; 2000. https://www.ncbi.nlm.nih.gov/books/NBK21582/.

49. van der Rest M, Garrone R. Collagen family of proteins. *FASEB J*. 1991;5(13):2814-2823. http://www.ncbi.nlm.nih.gov/pubmed/1916105.

50. Shoulders MD, Raines RT. Collagen Structure and Stability. 2009. doi:10.1146/annurev.biochem.77.032207.120833.

51. Schmelzer CEH. Assembly and Properties of Elastic Fibers. In: Anand Ramamurthi and Chandrasekhar Kothapalli, ed. *Elastic Fiber Matrices Biomimetic Approaches to Regeneration and Repair*. Boca Raton: CRC Press; 2016:1-30.

52. Wagenseil JE, Mecham RP. Elastin in large artery stiffness and hypertension. *J Cardiovasc Transl Res*. 2012;5(3):264-273. doi:10.1007/s12265-012-9349-8.

53. Ewart AK, Jin W, Atkinson D, Morris CA, Keating MT. Supravalvular aortic stenosis associated with a deletion disrupting the elastin gene. *J Clin Invest*. 1994. doi:10.1172/JCI117057.

54. Zhang MC, He L, Giro M, Yong SL, Tiller GE, Davidson JM. Cutis laxa arising from frameshift mutations in exon 30 of the elastin gene (ELN). *J Biol Chem*. 1999. doi:10.1074/jbc.274.2.981.

55. Steven Wise TG, Weiss AS. Molecules in focus: Tropoelastin. *Int J Biochem Cell Biol*. 2009;41:494-497. doi:10.1016/j.biocel.2008.03.017.

56. Rodgers UR, Weiss AS. Cellular interactions with elastin. *Pathol Biol*. 2005;53:390-398. doi:10.1016/j.patbio.2004.12.022.

57. Kagan HM, Tseng L, Simpson DE. Control of elastin metabolism by elastin ligands. Reciprocal effects on lysyl oxidase activity. *J Biol Chem*. 1981.

58. Scott M, Vesely I. Morphology of porcine aortic valve cusp elastin. *J Heart Valve Dis*. 1996;5(5):464-471.

59. Sharma V, Panwar P, O ’donoghue AJ, et al. Structural requirements for the collagenase and elastase activity of cathepsin K and its selective inhibition by an exosite inhibitor. *Biochem J*. 2015;465:163-173. doi:10.1042/BJ20140809.

60. Liu J, Xiong W, Baca-Regen L, Nagase H, Baxter BT. Mechanism of inhibition of matrix metalloproteinase-2 expression by doxycycline in human aortic smooth muscle cells. *J Vasc Surg*. 2003. doi:10.1016/S0741-5214(03)01022-X.

61. Chapman HA, Riese RJ, Shi GP. Emerging roles for cysteine proteases in human

biology. *Annu Rev Physiol*. 1997;59:63-88. doi:10.1146/annurev.physiol.59.1.63.

62. Fonović M, Turk B. Cysteine cathepsins and extracellular matrix degradation. *Biochim Biophys Acta - Gen Subj*. 2014;1840:2560-2570. doi:10.1016/j.bbagen.2014.03.017.

63. Platt MO, Shockey WA. Endothelial cells and cathepsins: Biochemical and biomechanical regulation. *Biochimie*. 2016;122:314-323. doi:10.1016/j.biochi.2015.10.010.

64. Lecaille F, Brömme D, Lalmanach G. Biochemical properties and regulation of cathepsin K activity. *Biochimie*. 2008. doi:10.1016/j.biochi.2007.08.011.

65. Garnero P, Borel O, Byrjalsen I, et al. The collagenolytic activity of cathepsin K is unique among mammalian proteinases. *J Biol Chem*. 1999. doi:10.1074/jbc.273.48.32347.

66. Sun J, Sukhova GK, Zhang J, et al. Cathepsin K deficiency reduces elastase perfusion-induced abdominal aortic aneurysms in mice. *Arterioscler Thromb Vasc Biol*. 2012;32(1):15-23. doi:10.1161/ATVBAHA.111.235002.

67. Aggarwal S, Qamar A, Sharma V, Sharma A. Abdominal aortic aneurysm: A comprehensive review. *Exp Clin Cardiol*. 2011;16(1):11-15.

68. Grootenboer N, Bosch JL, Hendriks JM, van Sambeek MRHM. Epidemiology, Aetiology, Risk of Rupture and Treatment of Abdominal Aortic Aneurysms: Does Sex Matter? *Eur J Vasc Endovasc Surg*. 2009. doi:10.1016/j.ejvs.2009.05.004.

69. Sakalihasan N, Limet R, Defawe O. Abdominal aortic aneurysm. *Lancet*.

2005;365:1577-1589.

70. Johns Hopkins Medicine. Abdominal Aortic Aneurysm Repair. *Heal Libr*. http://www.hopkinsmedicine.org/healthlibrary/test_procedures/cardiovascular/abdominal_aortic_aneurysm_repair_92,p08291/. Accessed January 16, 2017.

71. Ioannou C V, Tsetis DK. Going Beyond Current AAA Neck Angulation Limitations of the Ovation Ultra-low Profile Polymer-filled Stent Graft. *Eur J Vasc Endovasc Surg*. 2016;52(52):172. doi:10.1016/j.ejvs.2016.06.003.

72. Maleux G, Koolen M, Heye S. Complications after endovascular aneurysm repair. *Semin Intervent Radiol*. 2009;26(1):3-9. doi:10.1055/s-0029-1208377.

73. Kieffer WKM, Sonnenberg S, Windhaber RA, Pal N, Pemberton RM. Complications and reintervention following elective open abdominal aortic aneurysm repair: A 10-year retrospective analysis. *Ann R Coll Surg Engl*. 2012. doi:10.1308/003588412X13171221501465.

74. Xu J, Shi G-P. Vascular wall extracellular matrix proteins and vascular diseases. *Biochim Biophys Acta*. 2014;1842(11):2106-2119. doi:10.1016/j.bbadis.2014.07.008.

75. Gong Z, Niklason LE. Small-diameter human vessel wall engineered from bone marrow-derived mesenchymal stem cells (hMSCs). *FASEB J*. 2008;22(6):1635-1648. doi:10.1096/fj.07-087924.

76. Watson N, Divers R, Kedar R, et al. Discarded Wharton jelly of the human umbilical cord: A viable source for mesenchymal stromal cells. *Cytotherapy*. 2015.

doi:10.1016/j.jcyt.2014.08.009.

77. Tamama K, Sen CK, Wells A. Differentiation of Bone Marrow Mesenchymal Stem Cells into the Smooth Muscle Lineage by Blocking ERK/MAPK Signaling Pathway. doi:10.1089/scd.2007.0155.

78. Heino T, Hentunen T. Differentiation of osteoblasts and osteocytes from mesenchymal stem cells. *Curr Stem Cell Res Ther*. 2008;3(2):131-145.

79. Balog BM, Ramamurthi A, Damaser MS. Sourcing and Manipulating Stem Cells for Elastin Regeneration Applications. In: Anand Ramamurthi and Chandrasekhar Kothapalli, ed. *Elastic Fiber Matrices Biomimetic Approaches to Regenerative Repair of Elastic Matrix* . Boca Raton: CRC Press; 2016:227-253.

80. Swaminathan G, Gadepalli V, Stoilov I, Mecham R, Rao R, Ramamurthi A. Pro-elastogenic effects of bone marrow mesenchymal stem-cell derived smooth muscle cells on cultured aneurysmal smooth muscle cells. *J Tissue Eng Regen Med*. 2014;11(3):679-693.

81. Thompson RW, Geraghty PJ, Lee JK. Abdominal aortic aneurysms: Basic mechanisms and clinical implications. *Curr Probl Surg*. 2002. doi:10.1067/msg.2002.121421.

82. Wassef M, Upchurch GR, Kuivaniemi H, Thompson RW, Tilson MD. Challenges and opportunities in abdominal aortic aneurysm research. *J Vasc Surg*. 2007;45(1):192-198. doi:10.1016/j.jvs.2006.09.004.

83. Nosoudi N, Nahar-Gohad P, Sinha A, et al. Prevention of Abdominal Aortic

Aneurysm Progression by Targeted Inhibition of Matrix Metalloproteinase Activity with Batimastat-Loaded Nanoparticles. *Circ Res*. 2015. doi:10.1161/CIRCRESAHA.115.307207.

84. Nosoudi N, Parasaram V, Karamched SR, Chowdhury A, Vyavahare N. Pharmacologic Strategies for Preserving Elastic Matrix. In: Anand Ramamurthi and Chandrasekhar Kothapalli, ed. *Elastic Fiber Matrices Biomimetic Approaches to Regenerative Repair of Elastic Matrix*. Boca Raton: CRC Press; 2016:189-226.

85. Benjamin MM, Khalil RA. Matrix metalloproteinase inhibitors as investigative tools in the pathogenesis and management of vascular disease. *EXS*. 2012. doi:10.1007/978-3-0348-0364-9_7.

86. Vandenbroucke RE, Libert C. Is there new hope for therapeutic matrix metalloproteinase inhibition? *Nat Publ Gr*. 2014;13. doi:10.1038/nrd4390.

87. Rentschler M, Baxter BT. Pharmacological approaches to prevent abdominal aortic aneurysm enlargement and rupture. In: *Annals of the New York Academy of Sciences*. ; 2006. doi:10.1196/annals.1383.003.

88. Sho E, Chu J, Sho M, et al. Continuous periaortic infusion improves doxycycline efficacy in experimental aortic aneurysms. *J Vasc Surg*. 2004. doi:10.1016/j.jvs.2004.01.036.

89. Mosorin, MD M, Juvonen, MD, PhD J, Biancari, MD, PhD F, et al. Use of doxycycline to decrease the growth rate of abdominal aortic aneurysms: A randomized, double-blind, placebo-controlled pilot study. *J Vasc Surg*. 2001;34(4):606-610.

90. Baxter BT, Pearce WH, Waltke EA, et al. Prolonged administration of doxycycline in patients with small asymptomatic abdominal aortic aneurysms: Report of a prospective (Phase II) multicenter study. *J Vasc Surg*. 2002;36(1):1-12. doi:10.1067/mva.2002.125018.

91. Priya James H, John R, Alex A. Smart polymers for the controlled delivery of drugs – a concise overview. *Acta Pharm Sin B*. 2014;4(2):120-127. doi:10.1016/j.apsb.2014.02.005.

92. Webster DM, Sundaram P, Byrne ME. Injectable nanomaterials for drug delivery: Carriers, targeting moieties, and therapeutics. *Eur J Pharm Biopharm*. 2013;84(1):1-20. doi:10.1016/j.ejpb.2012.12.009.

93. Danhier F, Ansorena E, Silva JM, Coco R, Le Breton A, Pr??at V. PLGA-based nanoparticles: An overview of biomedical applications. *J Control Release*. 2012. doi:10.1016/j.jconrel.2012.01.043.

94. Gentile P, Chiono V, Carmagnola I, Hatton P V. An overview of poly(lactic-co-glycolic) Acid (PLGA)-based biomaterials for bone tissue engineering. *Int J Mol Sci*. 2014. doi:10.3390/ijms15033640.

95. Vasir JK, Labhasetwar V. Biodegradable nanoparticles for cytosolic delivery of therapeutics. *Adv Drug Deliv Rev*. 2007. doi:10.1016/j.addr.2007.06.003.

96. Couvreur P. Nanoparticles in drug delivery: Past, present and future. *Adv Drug Deliv Rev*. 2013;65(1):21-23. doi:10.1016/j.addr.2012.04.010.

97. Huang G, Chen H, Dong Y, et al. Superparamagnetic iron oxide nanoparticles:

Amplifying ros stress to improve anticancer drug efficacy. *Theranostics*. 2013;3(2):116-126. doi:10.7150/thno.5411.

98. Gun S, Edirisinghe M, Stride E. Encapsulation of superparamagnetic iron oxide nanoparticles in poly-(lactide-co-glycolic acid) microspheres for biomedical applications. *Mater Sci Eng C Mater Biol Appl*. 2013;33(6):3129-3137. doi:10.1016/j.msec.2013.03.001.

99. Mahmoudi M, Sant S, Wang B, Laurent S, Sen T. Superparamagnetic iron oxide nanoparticles (SPIONs): Development, surface modification and applications in chemotherapy. *Adv Drug Deliv Rev*. 2011. doi:10.1016/j.addr.2010.05.006.

100. Parveen S, Misra R, Sahoo SK. Nanoparticles: A boon to drug delivery, therapeutics, diagnostics and imaging. *Nanomedicine Nanotechnology, Biol Med*. 2012;8(2):147-166. doi:10.1016/j.nano.2011.05.016.

101. Kim CS, Duncan B, Creran B, Rotello VM. Triggered nanoparticles as therapeutics. *Nano Today*. 2013;8(4):439-447. doi:10.1016/j.nantod.2013.07.004.

102. Mura S, Nicolas J, Couvreur P. Stimuli-responsive nanocarriers for drug delivery. *Nat Mater*. 2013;12(11):991-1003. doi:10.1038/NMAT3776.

103. Arranja AG, Pathak V, Lammers T, Shi Y. Tumor-targeted nanomedicines for cancer theranostics. *Pharmacol Res*. 2017. doi:10.1016/j.phrs.2016.11.014.

104. Etheridge ML, Campbell SA, Erdman AG, Haynes CL, Wolf SM, McCullough J. The big picture on nanomedicine: The state of investigational and approved nanomedicine products. *Nanomedicine Nanotechnology, Biol Med*. 2013.

doi:10.1016/j.nano.2012.05.013.

105. Thakor AS, Jokerst J V, Ghanouni P, Campbell JL, Mittra E, Gambhir SS. Clinically Approved Nanoparticle Imaging Agents. *J Nucl Med*. 2016;57:1833-1837. doi:10.2967/jnumed.116.181362.

106. Chertok B, Moffat BA, David AE, et al. Iron oxide nanoparticles as a drug delivery vehicle for MRI monitored magnetic targeting of brain tumors. *Biomaterials*. 2008;29(4):487-496. doi:10.1016/j.biomaterials.2007.08.050.

107. Kandasamy G, Maity D. Recent advances in superparamagnetic iron oxide nanoparticles (SPIONs) for in vitro and in vivo cancer nanotheranostics. *Int J Pharm*. 2015. doi:10.1016/j.ijpharm.2015.10.058.

108. Dawidczyk CM, Kim C, Park JH, et al. State-of-the-art in design rules for drug delivery platforms: Lessons learned from FDA-approved nanomedicines. *J Control Release*. 2014. doi:10.1016/j.jconrel.2014.05.036.

109. Agyare E, Kandimalla K. Delivery of Polymeric Nanoparticles to Target Vascular Diseases. *Biomol Res Ther*. 2014;S1:001:1-11. doi:10.4172/2167-7956.S1-001.

110. Gacchina CE, Deb P, Barth JL, Ramamurthi A. Elastogenic inductability of smooth muscle cells from a rat model of late stage abdominal aortic aneurysms. *Tissue Eng Part A*. 2011;17(13-14):1699-1711. doi:10.1089/ten.TEA.2010.0526.

111. Labarca C, Paigen K. A simple, rapid, and sensitive DNA assay procedure. *Anal Biochem*. 1980;102:344-352.

112. Jennewine B, Fox J, Ramamurthi A. Cathepsin K-targeted sub-micron particles for

regenerative repair of vascular elastic matrix. *Acta Biomater*. 2017. doi:10.1016/j.actbio.2017.01.032.

113. Sivaraman B, Swaminathan G, Moore L, et al. Magnetically-responsive, multifunctional drug delivery nanoparticles for elastic matrix regenerative repair. *Acta Biomater*. 2016. doi:10.1016/j.actbio.2016.11.048.